Publication Series of the John von Neumann Institute for Computing (NIC)
NIC Series Volume 43

John von Neumann Institute for Computing (NIC)

Stefan F. Krieg

Towards the Confirmation of QCD on the Lattice

Improved Actions and Algorithms

PhD Thesis, Bergische Universität Wuppertal,
Forschungszentrum Jülich

Advisor:	Thomas Lippert
2nd referee:	Zoltán Fodor
3rd referee:	Andreas Schäfer

NIC Series Volume 43 ISBN 978-3-9810843-9-9

Die Deutsche Bibliothek – CIP-Cataloguing-in-Publication-Data
A catalogue record for this publication is available from Die Deutsche Bibliothek

Publisher: NIC-Directors
Distributor: NIC-Secretariat
Research Centre Jülich
52425 Jülich
Germany
Internet: www.fz-juelich.de/nic
Printer: Graphische Betriebe, Forschungszentrum Jülich

NIC Series Volume 43 ISBN 978-3-9810843-9-9

Dedicated to the memory of
Elfriede and Friedrich Westermann
Ruth and Kurt Krieg

Abstract

Lattice Quantum Chromodynamics has made tremendous progress over the last decade. New and improved simulation algorithms and lattice actions enable simulations of the theory with unprecedented accuracy.

In the first part of this thesis, novel simulation algorithms for dynamical overlap fermions are presented. The generic Hybrid Monte Carlo algorithm is adapted to treat the singularity in the Molecular Dynamics force, to increase the tunneling rate between different topological sectors and to improve the overall volume scaling of the combined algorithm. With this new method, simulations with dynamical overlap fermions can reach smaller lattice spacings, larger volumes, smaller quark masses, and therefore higher precision than had previously been possible.

The second part of this thesis is focused on a large scale simulation aiming to compute the light hadron mass spectrum. This simulation is based on a tree-level Symanzik improved gauge and tree-level improved stout-smeared Wilson clover action. The efficiency of the combination of this action and the improved simulation algorithms used allows to completely control *all* systematic errors. Therefore, this simulation provides a highly accurate ab initio calculation of the masses of the light hadrons, such as the proton, responsible for 95% of the mass of the visible universe, and confirms Lattice QCD in the light hadron sector.

Contents

Lattice Quantum Chromodynamics
"has now become the principal tool for
quantitative calculations in hadron
physics."

M. Peskin & D. Schroeder

Chapter 1

Introduction

The above quote continues: "This method currently gives the masses of the low-lying mesons and baryons to accuracies of 10-20%; it also allows the calculation of weak interaction matrix elements at the 25% level. As computers become more powerful, this numerical method can be pushed to higher accuracy" [1]. This was in 1995.

As a matter of fact, the huge compute power of today's supercomputers with its exponential increase never "outsmarted" the physicists. Only in 2001, the suggestion that, within a few years, Lattice Quantum Chromodynamics (LQCD) simulations with Wilson type fermions [2, 3] would reach pion masses below the 200 MeV threshold would have seemed unrealistic at best. At that time, judging from the algorithms available, it appeared that even the computing power of the upcoming multi-PFlop/s machines would not suffice to tune down the pion mass this far. But, as a matter of fact, through algorithmic advances, a good choice of lattice action and the availability of supercomputers of the PFlop/s class, it is possible today.

The precision of LQCD calculations could therefore be increased substantially. In chapter 3 of this thesis, I will present a calculation of the masses of the low-lying mesons and baryons with fully controlled systematic errors that improves on the above cited "10-20%" accuracy with combined errors reaching below 2% [4]. This not only represents a complete ab initio calculation of these masses and thus further evidence that QCD is the correct theory of the strong interaction, but it also means that for other quantities as well, high precision LQCD calculations are now possible.

In the case of weak interaction matrix elements, however, such calculations will be less straightforward. The reason for this is the lack of chiral symmetry – which is true even for improved actions such as the one used in chapter 3. While this problem can be solved

by also improving the corresponding operators and including mixing effects between them, there are aspects of QCD, especially those that are connected to chiral symmetry and topology, that are more naturally studied with a different approach.

For simulations aiming at such quantities, Ginsparg-Wilson (GW) fermions are the method of choice. A particular GW fermion is given by the so called overlap fermion Dirac operator [5, 6]. Such a discretization scheme obeys a lattice variant of chiral symmetry [7], as expressed by the Ginsparg-Wilson relation for the quark propagator [8][1]. Consequently, no additive renormalization of the quark mass is required and extrapolations to physical quark masses can be done with continuum chiral perturbation theory.

However, the good conceptual properties come at a high price. The overlap operator is defined via a matrix sign function of a kernel matrix. This kernel is a generic (not necessarily chiral) lattice Dirac operator with a negative mass. Although optimized implementations exist [9], the computation of the matrix sign function still requires $O(100)$ calls to the kernel Dirac operator. Therefore, any simulation with overlap fermions will be correspondingly more expensive than a simulation directly based on the kernel.

Furthermore, the sign function is discontinuous when a kernel eigenvalue changes sign. The generic dynamical[2] fermion algorithm, the Hybrid Monte Carlo (HMC) [10], has to be adapted to be able to cope with this discontinuity. In chapter 2 of this thesis, such an adapted HMC is described. This algorithm correctly treats the discontinuity of the sign function and also solves a range of other problems inherent to simulations with dynamical overlap fermions. With this new algorithm, it will be possible to reach smaller lattice spacings on larger volumes and at pion masses, which are significantly closer to the experimental value than previously possible with this formulation of the theory. The precision of the physics results will increase correspondingly.

1.1 Improved actions and algorithms

LQCD renders the Euclidean path integral computable by restricting the fermionic degrees of freedoms to the sites and the gauge degrees of freedoms to the links of a 4-dimensional

[1] This lattice variant of chiral symmetry differs only by a continuum irrelevant $O(a)$ correction term from the generic continuum definition.

[2] Simulations with dynamical fermions include the effects of virtual quarks in the QCD vacuum, as opposed to the so-called quenched approximation, where the fermion determinant is set to a constant and which therefore neglects these effects.

space-time lattice[3]. Although the discretization procedure of the action is by no means unique, some constraints need to be satisfied. Most important of all, the continuum action must be recovered in the continuum limit, *i.e.* the limit of infinite volume and vanishing lattice spacing a (in that order). It is also desirable to retain as many of the symmetry properties of the continuum action as possible. This is important for practical purposes but also to ensure that the lattice action is in the correct universality class [12, 13, 16–18], so that the details of the discretization scheme become irrelevant in the continuum limit. The remaining freedom can be used to optimize the action with respect to the smoothness of the continuum limit and simulation efficiency. However, there is no consensus on how this should be done in particular. Thus, different lattice actions are used in LQCD calculations, with each of them having unique advantages and problems.

This is especially true for the two discretizations used in this thesis. Overlap fermions provide the fermionic action which is closest to the continuum definition in terms of symmetries surviving the discretization procedure. The overlap action is improved in the sense that its scaling toward the continuum limit is free of any $O(a)$ discretization effects. However, as mentioned above, overlap fermions are difficult to implement and simulate. Thus, until now, simulations with dynamical overlap fermions were restricted to rather large pion masses on coarse lattices with small volumes. Wilson fermions, on the other hand, break chiral symmetry, but are far less complicated in structure, and simulations are considerably less costly than those with overlap fermions. Therefore, finer lattice spacings and larger volumes could be used. However, lack of chiral symmetry leaves the low fermionic eigenmodes unrestricted and the induced eigenmode fluctuations make simulations extremely costly when the pion mass is tuned towards its experimentally observed value. This phenomenon is called “critical slowing down”. By improving the action (see chapter 3), the effects of the broken chiral symmetry can be reduced significantly. If improved simulation algorithms are used as well, small pion masses can be reached. Improved algorithms are even more required for overlap fermions (see chapter 2), firstly, to make simulations possible at all, and secondly, to make them feasible – given the computational costs of this discretization.

[3] Introductory material can be found in [11–15]. The current status of the field is covered in the proceedings of the annual lattice conference.

1.2 Layout of the thesis

This thesis is based on different projects in which I have participated. These projects can be organized in two topical groups, presented in chapter 2 and chapter 3.

Topic 1: algorithms for overlap fermions

In chapter 2, the HMC algorithm for dynamical overlap fermions is described. The algorithm was adapted to enable topology changes and optimized to enhance the "transmission rate", the rate of actual changes of topology. The emphasis of this chapter is on the new algorithms. It is mainly based on the articles

- [19] N. Cundy, S.K., G. Arnold, A. Frommer, Th. Lippert, K. Schilling, Comput. Phys. Commun. **180** (2009), 26-54;
- [20] N. Cundy, S.K., Th. Lippert, A. Schafer, Comput. Phys. Commun. **180** (2009), 201-208.

I will begin with a description of the basic algorithm [19] and afterwards work out how this algorithm has to be changed to increase the transmission rate [20]. Finally, I will summarize and conclude.

Topic 2: improved Wilson fermions

In chapter 3, a setup for simulations with Wilson type fermions is described and applied to a simulation calculating the masses of the low-lying hadrons with fully controlled systematic errors. This is the main result of this chapter and is regarded as a conformation of LQCD in the light hadron sector [21]. The chapter is based on the articles

- [22] S. Dürr, Z. Fodor, C. Hoelbling, R. Hoffman, S.D. Katz, S.K., T. Kurth, L. Lellouch, T. Lippert, K.K. Szabo, G. Vulvert, Phys. Rev. **D79** (2009), 014501;
- [4] S. Dürr, Z. Fodor, J. Frison, C. Hoelbling, R. Hoffmann, S.D. Katz, S.K., T. Kurth, L. Lellouch, T. Lippert, K.K. Szabo, G. Vulvert, Science **322** (2008), 1224-1227.

Here, I will begin, based on ref. [22], with a description of the action and the algorithms used, show how this setup was tested and verified and present a scaling analysis of the action. Finally, I will describe the calculation of the hadron spectrum of ref. [4] and conclude. This work was done within the Budapest-Marseille-Wuppertal collaboration (see acknowledgments).

Finally, in section chapter 4, I will summarize the results and conclude with an outlook.

It does not matter how slowly you go
so long as you do not stop.

孔子

Chapter 2

Hybrid Monte Carlo algorithm for overlap fermions

In this section, we will discuss an adapted HMC for dynamical overlap fermions. Let us begin by first reviewing some fundamental properties of the operator. The overlap Dirac operator [5, 6] contains the sign function of a kernel operator in its definition. This kernel (D_K) is a generic (not necessarily chiral) lattice Dirac operator at a negative mass (*e.g.* the Wilson operator, see below). The massless operator is given by

$$D_{ov} = 1 + \gamma_5 \,\mathrm{sign}(\gamma_5 D_K). \tag{2.1}$$

As already mentioned in the introduction, overlap fermions have a number of important theoretical advantages over generic formulations of LQCD. Most of these are directly related to the lattice variant of chiral symmetry preserved by overlap fermions. More generally[1], a lattice fermion action with a lattice Dirac operator that fulfills a Ginsparg-Wilson (GW) relation of the type

$$D_{GW}\gamma_5 + \gamma_5 D_{GW} = a D_{GW}\gamma_5 D_{GW} \tag{2.2}$$

will be invariant under the infinitesimal transformation ($\theta \ll 1$)

$$\Psi \to \Psi + i\theta\gamma_5 \left(1 - \frac{a}{2} D_{GW}\right)\Psi \qquad \bar{\Psi} \to \bar{\Psi} + \bar{\Psi} i\theta \left(1 - \frac{a}{2} D_{GW}\right)\gamma_5. \tag{2.3}$$

These are the chiral $U_A(1)$ transformations [7] on the lattice. The overlap Dirac operator defined in eqn. (2.1) above satisfies the GW relation of eqn. (2.2).

[1] For a detailed review of Ginsparg-Wilson fermions and their properties please see [23] and references therein.

Under the transformations of eqn. (2.3) the fermion measure is not invariant but picks up the factor

$$\delta\left(\mathscr{D}\Psi\mathscr{D}\bar{\Psi}\right) = \mathrm{Tr}\left[\gamma_5 a D_{GW}\right],$$

the index of the GW Dirac operator. The index in turn is, in the same way as in the continuum (Atiyah Singer index theorem), directly related to the topological charge Q_{top} of the gauge field background

$$\begin{aligned} \mathrm{index}\left(D_{GW}\right) &= \sum_x q(x) = Q_{top} + O(a^2), \\ q(x) &\equiv \mathrm{Tr}\left[\gamma_5 D_{GW,xx}\right], \qquad (2.4) \\ q(x) &= \frac{1}{32\pi^2}\varepsilon_{\mu\nu\rho\sigma}\mathrm{Tr}\left[F_{\mu\nu}F_{\rho\sigma}\right] + O(a^2). \qquad (2.5) \end{aligned}$$

Equation 2.4 gives a natural definition of the topological density $q(x)$ for a GW Dirac operator with the correct continuum limit (eqn. (2.5), see arguments below). In total, with the modified chiral transformations of eqn. (2.3), on the lattice there is the same connection between chiral $U_A(1)$ transformations and the anomaly (and thus the topological charge) as in the continuum.

It can be shown that the gauge field strength tensor can be recovered from the overlap operator via [24]

$$F_{\mu\nu} \propto a^2\mathrm{Tr}\left[\sigma_{\mu\nu}D_{ov}\right] + O(a^3).$$

A similar relation should hold for any Dirac operator that is sufficiently complex to contain a closed loop of gauge links. In principle, given that any operator that satisfies eqn. (2.2) will be a Dirac operator of this kind[2], it is possible to construct the whole LQCD action based on the GW operator alone. The gauge action is for example given by [28]

$$\mathrm{Tr}\left[D_{GW} - D_{GW}(U_\mu = 1)\right] \propto a^4\mathrm{Tr}\left[F_{\mu\nu}F_{\mu\nu}\right] + O(a^6).$$

By using a relation of this kind, an action can be constructed that has the same notion of topology, both in the quark and gluon sector. Such a setup is ideal for the analysis of the QCD vacuum and, since the transformations eqn. (2.3) are related to the $U_A(1)$ anomaly as in the continuum, an analysis of the connection between spontaneous chiral symmetry breaking and QCD vacuum effects.

The two best known exact realizations of a GW operator are the overlap and the fixed-point Dirac operators (see, eg. [29]), the latter being significantly more complicated in structure

[2] A lattice Dirac operator that satisfies eqn. (2.2), cannot be ultra-local [25–27].

and consequently more difficult to implement. Domain Wall fermions [30] provide a 5-dimensional approximation to a GW operator that becomes exact when L_s, the size of the 5th dimension, is tuned towards infinity. This thesis focuses on simulation algorithms with the overlap Dirac operator.

As indicated in the introduction, simulations with overlap fermions face a number of challenges. The sign function within the operator is discontinuous at the boundaries between sectors with different topological index. While this is no problem for the physics side of such a simulation, the generic dynamical fermion algorithm, the HMC, cannot be applied to overlap fermions without significant changes.

More precisely, it is the Molecular Dynamics (MD) part of the HMC that encounters severe problems with the discontinuity. The force associated with the fermion determinant has a singularity at the boundaries between different topological sectors. The conservation of the MD Energy will therefore be violated and the HMC will be unable to change topology. Since, however, such attempted changes happen regularly even on small lattice sizes, the algorithm will become arbitrarily slow and, most likely, fail to produce any ergodic ensemble at all.

An adapted HMC algorithm for overlap fermions thus has to meet the following conditions: The algorithm has to

- correctly treat the discontinuity of the overlap operator to allow for a sampling of all topological sectors,
- have an acceptable autocorrelation time, *e.g.* by changing topological sectors ("tunneling") at an acceptable rate,
- have acceptable energy violations during the MD, so that the acceptance rate of the final Metropolis step is not too low,
- and show that scaling up to large enough volumes is possible.

The dynamical overlap HMC described in this chapter satisfies all of these requirements. In section 2.3 the basics of the dynamical overlap HMC are given, such as the treatment of the discontinuity and energy conservation. Afterwards, in section 2.4, a variant of the HMC algorithm of section 2.3 is discussed that features a greatly improved tunneling rate and an exact treatment of the discontinuous part of the fermionic action as well as improved volume scaling.

2.1 Basics

In this section the prerequisites required for the dynamical overlap HMC are described and the problems that have to be addressed and solved are worked out. As a starting point and in order to introduce the notations and terminology, let us review the generic HMC [10] for Wilson fermions first.

2.1.1 HMC for $N_f = 2$ degenerate flavors of Wilson fermions

The standard Wilson Dirac operator on the lattice, with a mass $-m_0$, is

$$D_{W,xy} = 1_{xy} - \kappa \sum_{\mu} \Big[\big(1-\gamma_\mu\big) U_\mu(x) \delta_{x+e_\mu,y} + \big(1+\gamma_\mu\big) U^\dagger_\mu(x-e_\mu) \delta_{x-e_\mu,y} \Big],$$
$$\kappa = \frac{1}{8-2m_0}.$$

The Wilson operator is γ_5-Hermitian, implying that one can construct a Hermitian Wilson operator $Q = \gamma_5 M$. The HMC method updates the gauge field in two steps:

1. a Molecular Dynamics evolution of the gauge field and
2. a Metropolis step which renders the algorithm exact.

For the MD evolution of the gauge fields U, a momentum Π is introduced. Using a fictitious computer time, τ, the momentum field is defined such that

$$dU/d\tau = \dot{U} = i\Pi U.$$

Since $U \in \mathrm{SU}(N_C)$, with N_C being the number of colors (for QCD $N_C = 3$), Π must be a Hermitian traceless matrix. The gauge field is then integrated following the classical equations of motion, keeping the total energy of the system constant. With the Wilson "plaquette" gauge action, the total MD energy of this system is

$$E(\tau) = \beta \sum_x \left[1 - \frac{1}{2N_C} \mathrm{Tr}\big(U_{\mu\nu}(x) + U^\dagger_{\mu\nu}(x)\big) \right] + X^\dagger_W \Phi + \frac{1}{2} \sum \mathrm{Tr}\Pi^2, \tag{2.6}$$
$$X_W = Q^{-2}\Phi, \quad U_{\mu\nu}(x) = U_\mu(x) U_\nu(x+e_\mu) U^\dagger_\mu(x+e_\nu) U^\dagger_\nu(x)$$

Φ is a Gaussian random spinor field and $U_{\mu\nu}(x)$ is the plaquette. The second equation of motion can be inferred from the condition

$$\frac{dE}{d\tau} = 0$$
$$= \sum_{x,\mu} \mathrm{Tr} \left[\frac{1}{2} \frac{d}{d\tau} (\Pi_\mu(x)^2) - i \left(\frac{\beta}{6} \Pi_\mu(x) U_\mu(x) V_\mu(x) + \Pi_\mu(x) F_\mu(x) - h.c. \right) \right],$$

leading to

$$\dot{\Pi}_\mu(x) = i\left[\left(\frac{\beta}{6}U_\mu(x)V_\mu(x) + F_\mu(x) - h.c.\right)\right]_{\text{Traceless}}.$$

Here $V_\mu(x)$ is the "staple", the sum over all the remaining parts of those plaquettes which contain the specific gauge link $U_\mu(x)$. $F_\mu(x)$ is the "fermionic force". It can be found by differentiating $X_W^\dagger \Phi$ with respect to $U_\mu(x)$. For Wilson fermions, the fermionic force is given by

$$F_\mu(x) = \kappa\left[\Big(MX_W\Big)_{x+e_\mu} X_W^\dagger(x)(1+\gamma_\mu) + X_W(x+e_\mu)\Big(MX_W\Big)^\dagger(x)(1-\gamma_\mu)\right].$$

These classical equations of motion have to be solved numerically.

For the Markov process to converge to the desired canonical distribution, it is a sufficient but not necessary condition, that the gauge field update maintains *detailed balance* [10–12, 14, 15]. This can easily shown to be true, if each MD update from computer time τ to computer time $\tau + \Delta\tau$ is both *area-conserving*, *i.e.* the Jacobian for the update is 1, and *reversible*, meaning that if at any point in the MD trajectory the sign of the momenta is flipped, the MD integration will trace back in opposite direction the previously generated trajectory.

These requirements translate to conditions on the MD integrator. The generic leapfrog algorithm[3] satisfies both requirements, and conserves energy up to order $\Delta\tau^2$. Here $\Delta\tau$ is the step size of the MD integration. For later convenience, we will write it in terms of a four-step procedure updating the momentum fields and gauge fields in turn (see alg. 2.1).

As mentioned above, starting from the "old" configuration, the HMC update consists of

1. $\Pi(\tau+\Delta\tau/2) = \Pi(\tau) + \Delta\tau\dot{\Pi}(\tau)/2.$
2. $U(\tau+\Delta\tau/2) = \exp\{i(\Delta\tau/2)\Pi(\tau+\Delta\tau/2)\}\, U(\tau).$
3. $U(\tau+\Delta\tau) \quad = \exp\{i(\Delta\tau/2)\Pi(\tau+\Delta\tau/2)\}\, U(\tau+\Delta\tau/2).$
4. $\Pi(\tau+\Delta\tau) \quad = \Pi(\tau+\Delta\tau/2) + \Delta\tau\dot{\Pi}(\tau+\Delta\tau)/2.$

Algorithm 2.1: The standard leapfrog update.

an MD integration in n_{md} steps (the trajectory), generating a new configuration, followed by a Metropolis accept/reject test. The latter corrects for the small violations in energy conservation due to the numerical integration. The updated configuration is either accepted

[3] There are superior integrators to the simple leapfrog [31–38]. The algorithms of this section can easily be adapted to make use of such integrators.

or rejected, with the probability of acceptance $P_{\text{acc}} = \min(1, \exp(E - E'))$, where E is the initial energy at the start of the trajectory (before the MD integration), and E' the final energy (after the MD integration).

The efficiency of the HMC depends on the acceptance rate, which, in turn, only depends on the typical total energy violation over a trajectory[4]. For any integrator used, this is a function of the step size $\Delta\tau$, which is given by the total time or trajectory length τ and the number of MD steps n_{md}. A higher precision within the MD, therefore, requires increasing n_{md}. The available computer power being the limiting factor, improving the acceptance rate by increasing n_{md} will result in a smaller number of trajectories generated with the same computational resources. Thus, there is a trade-off between the acceptance rate and the rate of trajectories computed. The optimum setting depends on the MD energy conservation and the integrators used [32, 39–43] and may also depend on the action.

2.1.2 "Naïve" HMC for $N_f = 2$ degenerate flavors of overlap fermions

We now proceed by naïvely replacing the Wilson by the overlap operator and recalculating the fermionic force. As expected, the force contains a singular term which prevents this algorithm from working in practice. Let us start by repeating some of the basics of overlap fermions. The massive overlap operator is given by [44]:

$$D = (1 + \mu) + \gamma_5 (1 - \mu) \operatorname{sign}(Q),$$

where μ is a mass term. The bare fermion mass is

$$m_b = 2\mu m_0 / (1 - \mu),$$

where m_0 is the quark mass parameter of the Wilson operator $D_W = \gamma_5 Q$.
The Hermitian overlap operator reads

$$H = \gamma_5 D.$$

Thus, the pseudo-fermion action is given by $S_{pf} = \phi^\dagger H^{-2} \phi$.

[4] It is therefore desirable to use an integrator which has small energy violation at acceptable computational costs.

The matrix sign function

The matrix sign function of a (Hermitian) kernel matrix (here the Hermitian Wilson operator) Q is defined as

$$\text{sign}(Q) = \sum_i |\lambda_i\rangle\langle\lambda_i|\text{sign}(\lambda_i),$$

where $|\lambda_i\rangle$ and λ_i are the eigenvectors and eigenvalues of Q respectively, and the sum is over the complete set of eigenvectors. In practice, given that the calculation of the entire eigenvalue spectrum is not feasible, one combines an approximation to the sign function for the bulk of the eigenvalue spectrum with the spectral decomposition for the eigenvalues closest to zero, where no approximation can (realistically) be accurate enough without immense computational cost. All present dynamical overlap algorithms are based on an implementation (or some variant) of the the matrix sign function via the Zolotarev approximation [9].

Eigenvalues outside the Zolotarev range

It is necessary to keep the approximation range fixed during the simulation if the sign function is not calculated to perfect accuracy. Therefore, the smallest eigenvalues of Q are treated explicitly in a spectral representation. If we project out the lowest n_e eigenvectors of Q, then the rational fraction expansion[5], which is only used to approximate the sign function for the eigenvalues of Q^2 within the fixed range $[\alpha^2, \beta^2]$, is modified to

$$\begin{aligned}\text{sign}(Q) =& aQ\sum_k A^k \omega_k(\alpha,\beta)\left(1 - \sum_{l=1}^{n_e} |\lambda_l\rangle\langle\lambda_l|\right) + \sum_{l=1}^{n_e} |\lambda_l\rangle\langle\lambda_l|\text{sign}(\lambda_l), \qquad (2.7)\\ A^k =& \frac{1}{a^2Q^2 + \zeta_k(\alpha,\beta)}.\end{aligned}$$

Here $a = 1/\alpha$, $|\lambda_l\rangle$ are the eigenvectors of Q with eigenvalue λ_l, and $\text{sign}(\lambda)$ denotes the sign function. The coefficients of the rational fraction, ω and ζ, are given in [9,47,48]. All eigenvectors of Q with eigenvalues $|\lambda| < \alpha$ will be treated exactly during the simulation.

[5] The rational fraction expansion can be efficiently implemented by a "multi shift solver", see *e.g.* [45,46].

Eigenvalues inside the Zolotarev range

Since the convergence rate of the solvers used within the rational approximation scheme depends on the condition number[6] of the Wilson kernel, Q, it is advantageous to project out a range of eigenvalues. To that end, one is free to project out eigenvectors within the Zolotarev range as well. This can be done either exactly, as in eqn. (2.7), or from the rational approximation itself:

$$\sum_k \frac{\omega_k}{a^2Q^2+\zeta_k} = \sum_k \frac{\omega_k}{a^2Q^2+\zeta_k}\left(1-\sum_{l=n_e+1}^{n_p}|\lambda_l\rangle\langle\lambda_l|\right)+ \sum_{l=n_e+1}^{n_p}|\lambda_l\rangle\langle\lambda_l|\sum_k\frac{\omega_k}{a^2\lambda_l^2+\zeta_k}. \tag{2.8}$$

In order to fulfill the requirements for detailed balance, a fixed number, n_p, of eigenvectors is projected out, treating the n_e eigenvectors below α explicitly according to (2.7), and using (2.8) for the remaining $n_p - n_e$ eigenvectors, which lie within the range of the rational fraction approximation.

Differentiating Eigenvectors

When calculating the fermionic force for the overlap HMC, we need to differentiate the sign function with respect to the fictitious time τ. This means that we have to differentiate both the rational fraction and the small eigenvalues and eigenvectors. Let us start by looking at how to differentiate the eigenvalues; the differentiation of the sign function itself will be discussed in the following paragraph.

We start with the eigenvalue equation

$$Q|\lambda_l\rangle = \lambda_l|\lambda_l\rangle,$$

and perform an infinitesimal change in the matrix Q, $Q \to Q+\delta Q$. The new eigenvalue equation reads

$$(Q+\delta Q)\left(|\lambda_l\rangle+|\delta\rangle\right) = (\lambda_l+\delta\lambda)\left(|\lambda_l\rangle+|\delta\rangle\right).$$

[6]The condition number is given by the ratio $\frac{\lambda_{max}}{\lambda_{min}}$, where λ_{min} and λ_{max} are the smallest respectively the largest eigenvalue of the matrix in question.

Since we are free to define $|\delta\rangle$ so that $\langle\lambda_l|\delta\rangle = 0$, we immediately have:

$$\begin{aligned}\dot{\lambda}_l =& \langle\lambda_l|\dot{Q}|\lambda_l\rangle,\\ \frac{d}{d\tau}|\lambda_l\rangle =& -P_l\dot{Q}|\lambda_l\rangle, \qquad (2.9)\\ P_l =& (1-|\lambda_l\rangle\langle\lambda_l|)(Q-\lambda_l)^{-1}(1-|\lambda_l\rangle\langle\lambda_l|). \qquad (2.10)\end{aligned}$$

Here we have added a second eigenvector projector to eqn. (2.10) so that both $\langle\lambda|P_l$ and $P_l|\lambda\rangle$ can be calculated numerically[7].

We want to use a CG multi-mass solver to perform the inversion of $Q-\lambda$, required in eqn. (2.9). To be able to do so, we have to cast eqn. (2.10) into positive definite form. This can be done by exploiting the normal-equation trick:

$$\frac{1}{Q-\lambda_i}(1-|\lambda_i\rangle\langle\lambda_i|) = (Q+\lambda_i)\frac{1}{Q^2-\lambda_i^2}\left(1-\sum_{j=1}^{n_p}|\lambda_j\rangle\langle\lambda_j|\right) + \sum_{j=1;j\neq i}^{n_p}|\lambda_j\rangle\langle\lambda_j|\frac{\lambda_j+\lambda_i}{\lambda_j^2-\lambda_i^2},$$

We are now in a position to calculate the fermionic force including the differentiation of the eigenvectors and values.

The fermionic force

By proceeding in the same way as for Wilson fermions, the force can be derived from the energy conservation condition (sums over k, l and repeated spatial indices μ and x will be assumed from this point onwards):

$$\begin{aligned}\dot{U}_\mu(x)F_\mu(x) + F_\mu^\dagger(x)\dot{U}_\mu^\dagger(x) =& -(1-\mu^2)\langle X|\left(\gamma_5\frac{d}{d\tau}\mathrm{sign}\,Q + \frac{d}{d\tau}\mathrm{sign}\,Q\gamma_5\right)|X\rangle,\\ X =& H^{-2}\phi.\end{aligned}$$

The differential of the sign function is:

$$\left(\frac{d}{d\tau}\mathrm{sign}\,Q\right)_{nm} = \dot{U}_\mu(x)\left[\tilde{F}^C_{\mu,nm}(x) + \tilde{F}^D_{\mu,nm}(x)\right] + h.c.,$$

[7] For reasons of computational costs, these equations are only used to calculate the fermionic force. This expansion also is only valid if the separation between the eigenvalues is sufficiently large (see appendix B of [19]). A treatment of the case when two eigenvalues are near degenerate can be found in [49, 50].

where $\tilde{F}^C$ contains the terms generated by differentiating the rational approximation, by differentiating the eigenvector projector $1-|\lambda\rangle\langle\lambda|$, and the continuous part of the differential of the last term in eqn. (2.7) containing $\mathrm{sign}(\lambda)$, while the singularity is contained in $\tilde{F}^D$:

$$\begin{aligned}\tilde{F}^C_\mu(x) =& \frac{\partial}{\partial U_\mu} aQ \sum_k A^k \omega_k(\alpha,\beta) \left(1 - \sum_{l=1}^{n_e} |\lambda_l\rangle\langle\lambda_l|\right) \\ &+ \sum_{l=1}^{n_e} \left(\frac{\partial}{\partial U_\mu}|\lambda_l\rangle\langle\lambda_l|\right) \mathrm{sign}(\lambda_l), \\ \tilde{F}^D_\mu(x) =& -\sum_l |\lambda_l\rangle\langle\lambda_l| \left(\frac{d\,\mathrm{sign}(\lambda_l)}{d\lambda_l}\langle\lambda_l|\frac{\partial Q}{\partial U_\mu}|\lambda_l\rangle\right). \end{aligned} \tag{2.11}$$

For later convenience, we define F^G as the gauge field force. Therefore, we have

$$F^G_\mu(x) = \langle X| i\frac{\beta}{6} U_\mu(x) V_\mu(x) |X\rangle + h.c.\,, \tag{2.12}$$

$$F^C_\mu(x) = -(1-\mu^2) i U_\mu(x) \langle X| \left\{\gamma_5, \tilde{F}^C_\mu(x)\right\} |X\rangle + h.c.\,. \tag{2.13}$$

This force can be inserted into a standard HMC routine, like the Wilson HMC at the beginning of this section. However, eqn. (2.11) contains a Dirac delta function (the derivative of the sign function). With a finite step size integrator, this force will not be felt and energy conservation will thus be violated.

Possible solutions to this problem will be discussed in the following section. Most commonly, whenever an eigenvalue of the Wilson operator crosses zero during an HMC trajectory, special attention is paid to this last term. One idea is to replace the standard integrator (leapfrog) by a special update step capable to deal with the discontinuity. As we will see, this can be done in an area-conserving and reversible way.

2.2 Discontinuity of the action

2.2.1 Possible strategies to treat the discontinuity

There are several ways to deal with the discontinuity of the action caused by the eigenvalue crossing:

1. Restrict the simulation to one topological sector. This can be achieved in different ways: One possibility is to always reflect (see section 2.3.5) when one encounters

a potential eigenvalue crossing [51]. By tracking how the sector boundary is approached, the relative weight of different topological sectors can be calculated. Observables in one sector can then be reweighed in the final expectation value.

Alternatively one could use an action which suppresses small eigenvalues of the kernel operator (both by choosing a topology preserving gauge action and by adding a fermionic term) [52]. As a side effect, the inverters will converge faster, because of the reduced condition number implied. Since, as opposed to the method above, in this case it is impossible per se to change to another topological sector, this algorithm will only be ergodic if the targeted sector is connected.

Within both methods one either has to ignore the contribution from sectors with non-zero topological charge probably inducing uncontrollable systematic errors, or has to set up a range of independent simulations to calculate reliable estimates of the sector weights.

2. Use an adapted update step. As soon as one encounters a crossing during the MD evolution of the gauge fields, one repeats the MD update, with the integration over the delta function treated exactly [53, 54]. This is the approach taken in section 2.3.

3. Split off the discontinuity and treat it exactly. Within this approach, the discontinuity is separated from the continuous part of the action, *e.g.* by factorizing the determinant into a discontinuous and a continuous part and treating the former separately. This approach can greatly enhance the tunneling rate. It is described in detail in section 2.4.

The computational costs per trajectory of the latter two methods are considerably larger especially compared to the small mode suppression ansatz. They are however exact and do not require any reweighting. Also, (frequent) changes between the topological sectors reduce the autocorrelation time, which improves the volume scaling of the algorithm. In total it seems that, for these reasons, it is well worth the effort to proceed along the lines of methods 2 and 3.

2.2.2 Computing the discontinuity of the action

To formulate the adapted algorithms, we need to calculate the discontinuity of the fermion action induced by an eigenvalue crossing. The discontinuity causes a violation of the energy conservation in the MD gauge field evolution during a simulation. Thus, following

eqn. (2.6) we start with the second equation of motion, derived by imposing energy conservation:

$$\frac{dE}{d\tau} = 0 = \ldots + \Phi^\dagger \frac{d}{d\tau}\left(H^{-2}\right)\Phi.$$

Care needs to be taken when differentiating the fermionic contribution to the action close to a discontinuity in H. By using the relation [19]

$$\frac{dA^{-1}}{d\tau} = -A^{-1}(\tau+\delta\tau)\frac{dA}{d\tau}A^{-1}(\tau),$$

with A being a matrix function of the variable τ, we get

$$\frac{d}{d\tau}H^{-2} = -\lim_{\delta\tau\to 0} H^{-2}(\tau+\delta\tau)\left.\frac{dH^2}{d\tau}\right|_\tau H^{-2}(\tau).$$

As for the Wilson HMC, we define $X = H^{-2}\phi$ containing the pseudo-fermion vector ϕ. Now, when there is a discontinuity in H, such as through the eigenvalue λ crossing zero, we need to compute X just before the crossing, giving $X_- = \lim_{\delta\to 0} H^{-2}(\lambda(\tau_c - |\delta|))$, and just after the crossing, giving $X_+ = \lim_{\delta\to 0} H^{-2}(\lambda(\tau_c + |\delta|))$, with τ_c being the MD time of the crossing. The energy conservation equation thus reads:

$$\begin{aligned}\frac{dE}{d\tau} = 0 = \sum_{x,\mu}\mathrm{Tr}\Bigg[&\frac{1}{2}\frac{d}{d\tau}\Pi_\mu^2(x) - i\frac{\beta}{6}\Big(\Pi_\mu(x)U_\mu(x)V_\mu(x) - h.c\Big) + \\ &(1-\mu^2)\langle X_+|\left(\gamma_5\frac{d}{d\tau}\mathrm{sign}\,Q + \frac{d}{d\tau}\mathrm{sign}\,Q\gamma_5\right)|X_-\rangle\Bigg].\end{aligned} \tag{2.14}$$

Using the same notation as above, we denote the momenta and the crossing mode just before and after the eigenvalue crossing as Π^- respectively λ_- and Π^+ respectively λ_+. We can recast eqn. (2.14) into the form (in the limit $\delta\tau \to 0$)

$$\begin{aligned}&\frac{1}{2}\frac{1}{\delta\tau}\sum_{x,\mu}\left[(\Pi_\mu^+)^2(x) - (\Pi_\mu^-)^2(x)\right] = \\ &\qquad -(1-\mu^2)\langle X_+|\left(\gamma_5|\lambda\rangle\langle\lambda| + |\lambda\rangle\langle\lambda|\gamma_5\right)|X_-\rangle\frac{\mathrm{sign}(\lambda_-) - \mathrm{sign}(\lambda_+)}{\delta\tau}.\end{aligned}$$

This shows that integrating over the Dirac delta function in the fermionic force will produce a discontinuity in the kinetic energy. We define

$$\begin{aligned}d(\tau) \equiv &-(1-\mu^2)\mathrm{sign}(\lambda_-)\langle X_+(\tau)|\gamma_5|\lambda(\tau)\rangle\langle\lambda(\tau)|X_-(\tau)\rangle \\ &-(1-\mu^2)\mathrm{sign}(\lambda_-)\langle X_+(\tau)|\lambda(\tau)\rangle\langle\lambda(\tau)|\gamma_5|X_-(\tau)\rangle.\end{aligned}$$

and have

$$\Delta S \equiv \lim_{\delta\tau\to 0} \frac{1}{2}\frac{1}{\delta\tau}\sum_{x,\mu}\left[(\Pi_\mu^+)^2(x) - (\Pi_\mu^-)^2(x)\right] = 2d(\tau_c). \tag{2.15}$$

It is straightforward to show that this discontinuity in the kinetic energy will exactly cancel the discontinuity in the pseudo-fermion action. Therefore, energy would be conserved across the eigenvalue crossing in an exact integration. Of course, numerical integration schemes are not exact and will produce a large error at the discontinuity.

Our task in the next section is to develop an integration algorithm which remains accurate in the presence of Dirac delta function forces while satisfying detailed balance.

2.3 HMC algorithm with adapted MD update step

The algorithm we describe in this section adds a "correction step" to the standard MD integrator (the leapfrog in this presentation, see alg. 2.1). The correction step handles the aforementioned discontinuities in an area-conserving[8] and reversible way. Since the leapfrog algorithm conserves energy with errors of $O(\Delta\tau^2)$, it clearly is desirable that the new scheme will also satisfy eqn. (2.14) with the same or better accuracy, so that the MD step size does not have to be reduced to keep violations of energy conservation on the same level.

After establishing our notation, we will discuss a simplified variant of the algorithm in the context of classical mechanics to introduce the ideas behind the method. The algorithm is then described in the context of QCD as a *general* method by which suitable correction steps can be derived in a *systematic* manner. Finally, we will discuss a particular integrator.

2.3.1 Notation

We will denote the volume, that is the number of lattice sites of the 4-dimensional space-time lattice, by V. The number of colors is N_C, although we will be only interested in the QCD case where $N_C = 3$. The gauge field U contains a member of $\mathrm{SU}(N_C)$ on every of the $4V$ links; the (conjugate) momentum field Π is represented by a Hermitian and traceless $N_C \times N_C$ matrix, also one on each link. Furthermore, we will denote the (fictitious) MD time, at which the gauge or momentum field is calculated, by a subscript. Thus, U_τ refers

[8] Area conservation is in fact not a necessary condition for detailed balance [55]. Non-area-preserving improved MD update algorithms for the overlap operator can be found in in [49, 55].

to the gauge field at MD time τ. To keep the notation simple, we have the MD update start at time zero and end at time $\Delta\tau$. We (re-)define τ_c so that the MD time of the eigenvalue crossing is at $\tau_c + \Delta\tau/2$. In addition, the superscript "$-$" is used to indicate that the effects of the crossing are not yet included into the momentum update and the crossing eigenvalue has it's original sign, and "$+$" indicates that the momentum has been updated to account for the crossing and the sign of the eigenvalue has flipped. To shorten the notation we define

$$\Pi^+ \equiv \Pi^+_{\Delta\tau/2},\ F^+ \equiv F^+_{\Delta\tau/2},\ \ldots \qquad U_c \equiv U^-_{\Delta\tau/2+\tau_c} = U^+_{\Delta\tau/2+\tau_c},\ \Pi^+_c = \Pi^+_{\Delta\tau/2+\tau_c}\ \ldots$$

and

$$(A,B) \equiv \sum_{x,\mu} \mathrm{Tr}(A_\mu(x) B_\mu(x)).$$

The continuous part of the (Hermitian) force is $F_\tau = F^G_\tau + F^C_\tau$, with F^G and F^C defined in eqns. (2.12) and (2.13).

In order to later write the correction step in a general form, Π is expanded in terms of an orthonormal basis. This basis is defined by a set of orthonormal basis vectors which are divided into N_S subsets, $\{\{\eta^1_1, \eta^1_2, \ldots\}, \{\eta^2_1, \eta^2_2, \ldots\}, \ldots\}$. The parameter N_k gives the number of η vectors in each subset k. The η^k_i are $4V(N_C^2 - 1)$ Hermitian traceless matrices which satisfy $(\eta^k_i, \eta^m_j) = \delta_{ij}\delta^{km}$. N_k and N_S are defined such that the subscripts (i and j) run from 1 to N_k, where N_k is not necessarily constant for all the k, while the superscripts (k and m) run from 1 to N_S. For the moment, we shall leave the N_ks and N_S as arbitrary parameters, which satisfy the constraint

$$\sum_{k=1}^{N_S} N_k = 4V(N_C^2 - 1).$$

Thus, the basis is complete, so that

$$\Pi = \sum_{k=1}^{N_S} \sum_{i=1}^{N_k} \eta^k_i (\eta^k_i, \Pi).$$

The η matrices are functions of U_c, and are otherwise independent of the momentum. $\eta^1_1 \equiv \eta$ is defined as being normal to the gauge field surface where the eigenvalue is zero[9]. η^1_2 is proportional to $F - \eta(\eta, F)$, where $F = F^+_{\tau_c+\Delta\tau/2} - F^-_{\tau_c+\Delta\tau/2}$. The other η matrices are arbitrary.

[9] An explicit formula for η can be found in [19], appendix A, eqn. (A.29).

2.3.2 The classical mechanics case

Before discussing the MD with the full overlap operator in QCD, let us first look at the much simpler problem of a classical mechanics particle approaching a potential wall of height $-2d$.

The potential energy in this case is defined as $V(q) = -2d\theta(q)$, (*i.e.* $V = 0$ for $q < 0$, and $V = -2d$ for $q > 0$). Note that d may be positive or negative. Let us consider the 1-dimensional case first. The kinetic energy of the particle before it hits the wall is $\frac{1}{2}(\Pi^-)^2$. Afterwards, there are two possibilities: if the initial momentum is large enough, the particle will continue onwards albeit with changed momentum $\Pi^{+2} = \Pi^{-2} + 4d$. This case is called *transmission*[10]. If the momentum is too small, the particle will carry insufficient kinetic energy to cross the wall and will be reflected (elastically), giving a final momentum $\Pi^+ = -\Pi^-$. This case is called *reflection*. The total energy $\frac{1}{2}\Pi^2 + V$ is of course conserved in both cases.

Next consider the classical mechanics particle in three dimensions. The coordinate system shall be defined in terms of the orthonormal basis vectors η, η_1^1, and η_2^1 as just given above. It is assumed that the potential is given by

$$V(\mathbf{q}) = -2d\theta\big((\mathbf{q}, \eta)\big),$$

such that η is the normal vector to the potential wall.

The three components of the momentum are defined as (Π^-, η), (Π^-, η_1^2) and (Π^-, η_2^2). It is well known what happens to the particle in classical mechanics after it hits the potential wall; in the case of transmission,

$$(\Pi^+, \eta) = \sqrt{(\Pi^-, \eta)^2 + 4d}, \tag{2.16}$$

is obtained, and the transverse momenta are

$$(\Pi^+, \eta_i^1) = (\Pi^-, \eta_i^1). \tag{2.17}$$

For reflection, the final momenta will be

$$(\Pi^+, \eta) = -(\Pi^-, \eta),$$

[10] Also (and arguably more often) "refraction" is used here in the literature, following the terminology of Fodor *et al.* [53, 54].'

and

$$(\Pi^+, \eta_i^1) = (\Pi^-, \eta_i^1),$$

respectively. Again, both cases conserve energy.

2.3.3 Beyond classical mechanics

In fact, there is no deeper reason why the MD trajectory must follow the classical mechanics trajectory, as long as it is energy conserving, area conserving, reversible and ergodic. Instead of eqn. (2.16) and eqn. (2.17) one can equally well use the scheme

$$\begin{aligned}(\Pi^+, \eta) &= (\Pi^-, \eta) \\ (\Pi^+, \eta_i^1) &= (\Pi^-, \eta_i^1)\sqrt{1 + 4d/((\Pi^-, \eta_1^1)^2 + (\Pi^-, \eta_2^1)^2)}\end{aligned}$$

It is evident that this update, as well as many others which could be chosen, conserves energy and is also area conserving. Let us look at the explicit formulae for this example:

$$\left|\frac{\partial(\Pi^+, \eta_i^1)}{\partial(\Pi^-, \eta_j^1)}\right| = \begin{vmatrix} J_{11} & J_{12} \\ J_{21} & J_{22} \end{vmatrix} = 1,$$

with the J_{ij} defined as

$$\begin{aligned}J_{11} =& \sqrt{1 + \frac{4d}{(\Pi^-, \eta_1^1)^2 + (\Pi^-, \eta_2^1)^2}} - \\ & \frac{4d(\Pi^-, \eta_1^1)^2}{((\Pi^-, \eta_1^1)^2 + (\Pi^-, \eta_2^1)^2)^2} \left(\sqrt{1 + \frac{4d}{(\Pi^-, \eta_1^1)^2 + (\Pi^-, \eta_2^1)^2}}\right)^{-1},\end{aligned}$$

$$J_{12} = -\frac{4d(\Pi^-, \eta_1^1)(\Pi^-, \eta_2^1)}{((\Pi^-, \eta_1^1)^2 + (\Pi^-, \eta_2^1)^2)^2} \left(\sqrt{1 + \frac{4d}{(\Pi^-, \eta_1^1)^2 + (\Pi^-, \eta_2^1)^2}}\right)^{-1},$$

$$J_{21} = -\frac{4d(\Pi^-, \eta_1^1)(\Pi^-, \eta_2^1)}{((\Pi^-, \eta_1^1)^2 + (\Pi^-, \eta_2^1)^2)^2} \left(\sqrt{1 + \frac{4d}{(\Pi^-, \eta_1^1)^2 + (\Pi^-, \eta_2^1)^2}}\right)^{-1},$$

$$J_{22} = \sqrt{1 + \frac{4d}{(\Pi^-, \eta_1^1)^2 + (\Pi^-, \eta_2^1)^2}} - \frac{4d(\Pi^-, \eta_2^1)^2}{((\Pi^-, \eta_1^1)^2 + (\Pi^-, \eta_2^1)^2)^2} \left(\sqrt{1 + \frac{4d}{(\Pi^-, \eta_1^1)^2 + (\Pi^-, \eta_2^1)^2}} \right)^{-1}.$$

It can be shown that this latter update is reversible, since reversing the time changes $d \to -d$. Thus, instead of creating a discontinuity in the momentum *normal* to the potential wall, we are introducing the discontinuity in the directions *transverse* to the potential wall.

Furthermore, one can also consider a 5-dimensional case (in 5-dimensional space), with two additional basis vectors η_1^2 and η_2^2, which provides the option of changing momentum in any or all of the directions defined by η, $\{\eta_1^1, \eta_2^1\}$, and $\{\eta_1^2, \eta_2^2\}$. This general scheme will allow to achieve the $O(\Delta\tau^2)$-scalability of the approach.

2.3.4 The QCD situation

With these results in mind, we now proceed to discuss the QCD situation. There are two important differences between the MD in LQCD and the classical mechanics example of the previous section. First of all, the configuration space of the gauge fields on the lattice has many more dimensions. We are only considering working with SU(N_C) on a 4-dimensional lattice with V lattice sites. Thus, the gauge and momentum fields exist within a $4V(N_C^2 - 1)$-dimensional space, giving us a great deal of freedom in how to update the momentum fields. Secondly, within the MD a numerical integration is performed rather than an exact integration. Care must thus be taken as to the effects of time discretization on both the energy conservation and the area conservation.

Simple update algorithm

Now, we can construct the QCD correction update. The first step is to update the gauge and momentum fields to time $\tau + \Delta\tau/2$, as in the leapfrog procedure (alg. 2.1), giving Π^- and U^-:

$$\Pi^- = \Pi_0 + \frac{\Delta\tau}{2} F_0^-$$
$$U^- = \exp\{i\frac{\Delta\tau}{2}\Pi_-\}\, U_0.$$

Next, the integration proceeds up to the crossing point itself:

$$\begin{aligned} \Pi_c^- &= \Pi^- + \tau_c F^- \\ U_c &= \exp\{i\tau_c \Pi^-\}\, U^-. \end{aligned} \tag{2.18}$$

We now perform the correction step. From eqn. (2.15) we get:

$$\left(\Pi_c^+, \Pi_c^+\right) = \left(\Pi_c^-, \Pi_c^-\right) + 4d. \tag{2.19}$$

In terms of our basis, a general solution of (2.19)[11] is:

$$\begin{aligned} \Pi_c^+ &= \Pi_c^- + \sum_{k=1}^{N_S} \left(\sum_{i=1}^{N_k} \eta_i^k (\eta_i^k, \Pi_c^-) \right) \left(\sqrt{1 + \frac{d_k}{\sum_i (\eta_i^k, \Pi_c^-)^2}} - 1 \right), \\ \sum d_k &= 4d. \end{aligned} \tag{2.20}$$

Finally, we move back to computer time $\tau + \Delta\tau/2$, and complete the rest of the normal leapfrog integration

$$\begin{aligned} \Pi^+ &= \Pi_c^+ - \tau_c \left(F_+\right), \\ U^+ &= \exp\{-i\tau_c \Pi^+\}\, U_c, \\ U_1 &= \exp\{i\frac{\Delta\tau}{2}\Pi^+\}\, U^+, \\ \Pi_1 &= \Pi^+ + \frac{\Delta\tau}{2} F_1^+. \end{aligned} \tag{2.21}$$

This defines the simple update algorithm. Unfortunately we cannot make use of it because of two reasons: firstly, there is the possibility that one of the square roots in eqn. (2.20) might be imaginary causing Π to no longer be Hermitian, which has to be the case in order to keep the gauge fields U unitary during the MD; and secondly because the steps described in eqns. (2.18) and (2.21) violate detailed balance[12].

Let us address the latter problem first and discuss the problem with the square root (which we will solve by reflecting in analogy to the classical mechanics example) later.

[11] This is in fact not the most general solution: there are other possibilities involving error functions, which can be easily shown by extending the derivation of the transmission update outlined in [55].

[12] Although τ_c is a function of the momentum, this alone is not enough to violate detailed balance, but, as shown in [19], appendix A, an update of the momentum parallel to η will violate area conservation.

Maintaining detailed balance

In order to ensure that detailed balance is fulfilled, we can update the momentum in directions normal to η, *i.e.* we replace (2.18) and (2.21) by

$$\Pi^{\pm}_{\Delta\tau+\tau_c} = \Pi^{\pm} + \tau_c(F^{\pm} - \eta(\eta, F^{\pm}));$$

note however that this replacement comes at the cost of an $O(\tau_c)$ violation of energy conservation. A more flexible general momentum integration step which satisfies detailed balance[13] is given by

$$\begin{aligned}\Pi^{+} =& \Pi^{-} - \tau_c(F - \eta(\eta,F)) - \frac{\tau_c}{3}\mathrm{Tr}F + \eta(\eta,\Pi^{-})\left(\sqrt{1+\frac{d_1}{(\eta,\Pi^{-})^2}} - 1\right) + \\ & \sum_{k=2}^{N_S}\left[\eta_1^k(\eta_1^k,\Pi^{-} - \frac{\tau_c}{2}(F^{+}+F^{-})) + \eta_2^k(\eta_2^k,\Pi^{-} - \frac{\tau_c}{2}(F^{+}+F^{-}))\right]\times \\ & \left[\sqrt{1+\frac{d_k}{[\eta_1^k,\Pi^{-} - \frac{\tau_c}{2}(F^{+}+F^{-})]^2 + [\eta_2^k,\Pi^{-} - \frac{\tau_c}{2}(F^{+}+F^{-})]^2}} - 1\right]. \end{aligned} \tag{2.22}$$

To satisfy detailed balance, we need $N_k = 2\,\forall k$. Furthermore, the d_k should be odd functions of $\Delta\tau$ and beyond that only depend on the gauge field at the crossing and, for $k \neq 1$, on (η,Π^{-}).

Improved error behaviour

Using the general update proposed in eqn. (2.22) allows the improvement of the energy conservation to $O(\Delta\tau^2)$ effects[14]. Instead of adding $2d$ to the kinetic energy, we add $2d - \Delta E_\tau$, with $\Delta E_\tau = \tau_c[(F^{+},\eta)(\Pi^{+},\eta) - (F^{-},\eta)(\Pi^{-},\eta)]$ accounting for the $O(\Delta\tau_c)$ errors. This can be implemented by setting $\sum d_k = 4d - 2\Delta E_\tau$. We can also remove some (though not all) of the $O(\Delta\tau^2)$ errors in the same way, improving the energy conservation to almost $O(\Delta\tau^3)$ accuracy, as demonstrated numerically in section 2.3.6. The presence of $O(\Delta\tau^2)$ errors is not inconsistent with reversibility because τ_c is an even function of $\Delta\tau$.

Transmission and reflection

We now come back to the problem of imaginary square roots in eqn. (2.22). In analogy to the classical mechanics picture discussed above, and following [53, 54], we solve the

[13] The proof can be found in [19], appendix A.
[14] The proof can be found in [19], appendix A.3.

problem by reflecting off the $\lambda = 0$ surface. Thus, to summarize, if the momentum is large enough, we can use eqn. (2.22) and pass through the $\lambda = 0$ surface into the new topological sector with updated momentum. As in the classical mechanics example, we call this case *transmission*, and this is the scenario described so far in this section. If, however, the momentum is too small, we reflect off the $\lambda = 0$ surface. As before, this is denoted as *reflection*. Unlike transmission, a reflection update is accompanied neither by a change in topological index nor by a discontinuity in the fermionic action.

The explicit formulae for the transmission and reflection momentum updates are given in the next section. Since for both of these we have to integrate the equation of motions until the point (in MD time) of the eigenvalue crossing, we require a precise knowledge of τ_c. Therefore, let us first discuss a scheme by which we can calculate τ_c with sufficient accuracy.

2.3.5 Integration over the discontinuity

Many methods are available that could be used here. When picking one we should keep in mind that it is desirable to calculate τ_c exactly rather than to use an approximation, since this removes one possible source of $O(\Delta\tau^2)$ energy conservation violating terms and, even more important, we have to ensure that the selected method does not cause a breakdown of reversibility. A fast and efficient way to fulfill both requirements is to use a root-finding algorithm, such as the Newton-Raphson. Using this method, we arrive at the following iterative procedure:

$$\tau_c^n = \tau_c^{n-1} - \frac{\langle \lambda_l(\Delta\tau/2 + \tau_c^{n-1}) | Q(\Delta\tau/2 + \tau_c^{n-1}) | \lambda_l(\Delta\tau/2 + \tau_c^{n-1}) \rangle}{\langle \lambda_l(\Delta\tau/2 + \tau_c^{n-1}) | \dot{Q}(\Delta\tau/2 + \tau_c^{n-1}) | \lambda_l(\Delta\tau/2 + \tau_c^{n-1}) \rangle}.$$

This allows us to increase the accuracy of the eigenvalue calculation as we approach τ_c, so that we can use a low accuracy calculation of the eigenvalue during the initial Newton-Raphson iterations. We only need to calculate the eigenvector to a high accuracy for the final iteration to ensure that τ_c reaches the required precision. If we used a bounded method, such as Brent's method [56, 57] or bisection, we would have to calculate the eigenvector to full accuracy at each step to ensure that the eigenvalue does not escape the bounds. However, the Newton-Raphson method will break down if the crossing is close to a minimum of the eigenvalue. In this case, we will have to fall back to a different algorithm, such as Brent's method, to get sufficiently close to the solution for the Newton-Raphson method to converge.

With this method, we can calculate τ_c for the transmission/reflection update step, which we will discuss in the remainder of this section.

Transmission

The update scheme for transmission[15] is given by (see alg. 2.2):

$$\begin{aligned}\Pi^+ =&\Pi^- + \tau_c(F) - \eta\,\tau_c(\eta,F) - \frac{\tau_c}{3}\mathrm{Tr}(F)+\\ &\left(\eta_1^k(\eta_1^k,\Pi^- - \frac{\tau_c}{2}(F^- + F^+)) + \eta_2^k(\eta_2^2,\Pi^- - \frac{\tau_c}{2}(F^- + F^+))\right)\times\\ &\left(\sqrt{1+\frac{d_k}{(\eta_1^k,\Pi^- - \frac{\tau_c}{2}(F^- + F^+))^2 + (\eta_2^k,\Pi^- - \frac{\tau_c}{2}(F^- + F^+))^2}} - 1\right), \qquad (2.23)\\ d_k =&\frac{1}{N_S}(4d - 2\tau_c(F^-,\eta)(\Pi^-,\eta) + 2\tau_c(F^+,\eta)(\Pi^+,\eta) + \tau_c^2(F^- + F^+, F^+ - F^-)).\end{aligned}$$

As mentioned earlier, η_1^k, and η_2^k must be orthonormal and orthogonal to η and F. We can construct these vectors using the following procedure:

- We start by taking three unit vectors, α, β and γ corresponding to putting one of the eight Gell-Mann matrices on one particular link.
- We then construct $\eta_1^k = \alpha\cos\theta + \beta\sin\theta\cos\phi + \gamma\sin\theta\sin\phi$, choosing the angles θ and ϕ so that η_1^k is normal to η and F.
- η_2^k is then constructed in the same way from three different Gell-Mann matrices on the same link.

Therefore, N_S is the number of links on the lattice.

Up to $O(1/V)$ effects, this procedure does not lead to a higher transmission rate than any other scheme[16]. In section 2.3.6, we will see how this choice of transmission algorithm affects the numerical stability and the transmission rate.

1. $\Pi^-(\tau+\Delta\tau/2) = \Pi(\tau) + \Delta\tau/2\dot{\Pi}(\tau)$;
2. $U^-(\tau+\Delta\tau/2) = \exp\{i(\Delta\tau/2)\Pi^-(\tau+\Delta\tau/2)\}\,U(\tau)$;
3. $U_c = \exp\{i\tau_c\Pi^-\}\,U^-$;
4. The momentum update given in eqn. (2.23);
5. $U^+ = \exp\{-i\tau_c\Pi^+\}\,U_c$;
6. $U(\tau+\Delta\tau) = \exp\{i(\Delta\tau/2)\Pi^+(\tau+\Delta\tau/2)\}\,U^+(\tau+\Delta\tau/2)$;
7. $\Pi(\tau+\Delta\tau) = \Pi^+(\tau+\Delta\tau/2) + (\Delta\tau/2)\dot{\Pi}_+(\tau+\Delta\tau)$.

Algorithm 2.2: The modified leapfrog algorithm for transmission.

[15] The proof that this update satisfies detailed balance is given in [19], appendix A.

[16] Although it is possible to use non-area conserving algorithms with a higher transmission rate — see [55].

1. $\Pi^-(\tau+\Delta\tau/2) = \Pi(\tau) + (\Delta\tau/2)\dot{\Pi}(\tau)$;
2. $U^-(\tau+\Delta\tau/2) = \exp\{i(\Delta\tau/2)\Pi^-(\tau+\Delta\tau/2)\}\, U(\tau)$;
3. $U_c = \exp\{i\tau_c\Pi^-\}\, U^-$;
4. The momentum update given in eqn. (2.24);
5. $U^+ = \exp\{i\tau_c\Pi^+\}\, U_c$;
6. $U(\tau+\Delta\tau) = \exp\{i(\Delta\tau/2)\Pi^+(\tau+\Delta\tau/2)\}U^+(\tau+\Delta\tau/2)$;
7. $\Pi(\tau+\Delta\tau) = \Pi^+(\tau+\Delta\tau/2) + (\Delta\tau/2)\dot{\Pi}_+(\tau+\Delta\tau)$.

Algorithm 2.3: The modified leapfrog algorithm for reflection.

Reflection

A reflection takes place whenever one of the momentum updates in the transmission algorithm would lead to an imaginary momentum. The reflection update (see alg. 2.3) is based on a method first proposed in [51]. It is given by[17]

$$\Pi^+ = \Pi^- - 2\eta(\eta,\Pi^-) - 2\tau_c(F^-) + 2\eta\,\tau_c(\eta,F^-) + 2\frac{\tau_c}{3}\mathrm{Tr}(F^-). \tag{2.24}$$

Note the change of sign in the gauge field update in step (5) of alg. 2.3, as compared to alg. 2.2.

The sign of the smallest eigenvalue should change for a transmission step, and remain the same for reflection. However with a low probability, this does not occur. Such odd phenomena happen if the $\lambda = 0$ surface is not smooth near to the point of crossing, so that the eigenvalue might try to cross again in the same MD step. We can correct for this by adding a second correction step (*i.e.* we repeated steps (3) (4) and (5) in alg. 2.3) if the sign of the smallest eigenvalue did not behave as expected.

Two different eigenvalues crossing during the same micro-canonical step will also cause this algorithm to break down, because of possible mixing between the two eigenvectors[18]. This phenomenon is discussed and solved in [49] by explicitly calculating and treating this effect.

2.3.6 Numerical results

In this section, we will review numerical evidence showing that the transmission/reflection algorithm we discussed so far works as expected. Let us start by giving a description of the algorithmic setup first.

[17] The proof that this update satisfies detailed balance is given in [19], appendix A.
[18] See [19], appendix B.

β	κ	μ
5.4	0.18	0.5
	0.19	0.5
	0.2	0.5
	0.21	0.5
	0.22	0.5
	0.225	0.5
	0.23	0.5
	0.225	0.4
		0.3
		0.2
		0.1
		0.05

Table 2.1: 4^4 ensembles

β	κ	μ
5.6	0.2	0.3
		0.1
		0.05

Table 2.2: 6^4 ensembles

β	κ	μ
5.6	0.2	0.3
		0.1

Table 2.3: 8^4 ensembles

Simulation setup

All of the numerical results within this section were obtained from simulating two degenerate quark flavors ($N_f = 2$) using the transmission and reflection updates in alg. 2.2 and alg. 2.3. The overlap inversions make use of the improved inversion algorithms in refs. [58–62]. The Wilson plaquette action, given in eqn. (2.6), is used for the gauge action.

Several ensembles were generated, with different quark masses, lattice spacings and volumes. A list of these simulations can be found in the tables 2.1-2.3.

In order to set the scale, the static potential and $r_0 = 0.49$fm was used giving a lattice spacing of approximately $a^{-1} \sim 590$MeV on the 6^4 lattices. Due to the small number of configurations available, the scale has large errors, although the fit proved to be very stable when single data points were left out. In the context of renormalization, these large errors render matching to the continuum impossible. Thus, given the magnitude of the uncertainties, we will make the rough approximation that $Z_m = 1$, given that renormalization constants are typically close to this value. This implies that on these ensembles a quark mass of $\mu = 0.05$ corresponds to a physical mass of ~ 100 MeV, *i.e.* around the value of the strange quark mass, however with a very large error, both in the statistical and systematical sense.

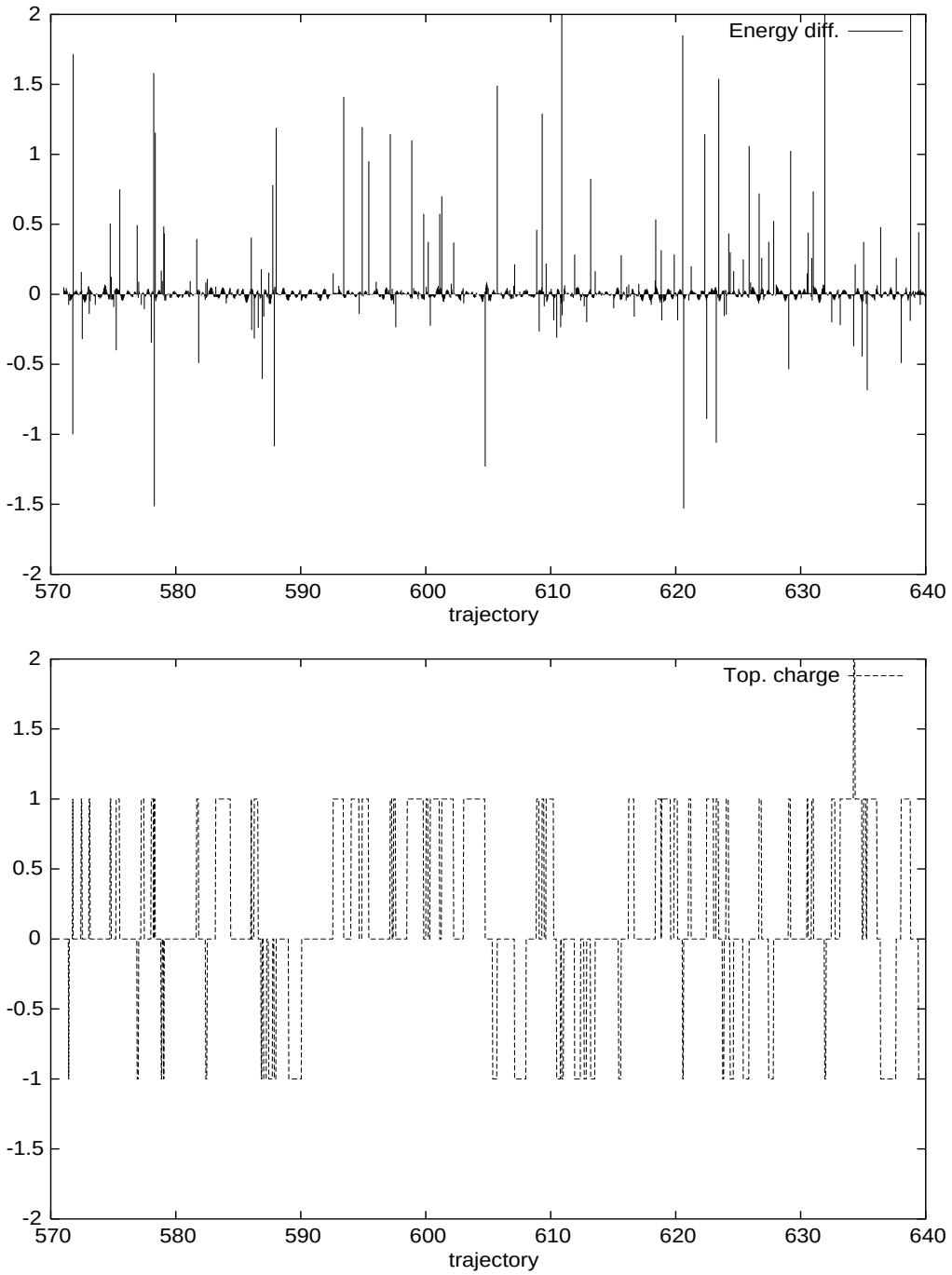

Figure 2.1: The energy difference between two micro-canonical steps, and the topological index plotted against the trajectory number, for an ensemble with $\beta = 5.4$, $\mu = 0.5$, and $\kappa = 0.225$, generated without the correction step.

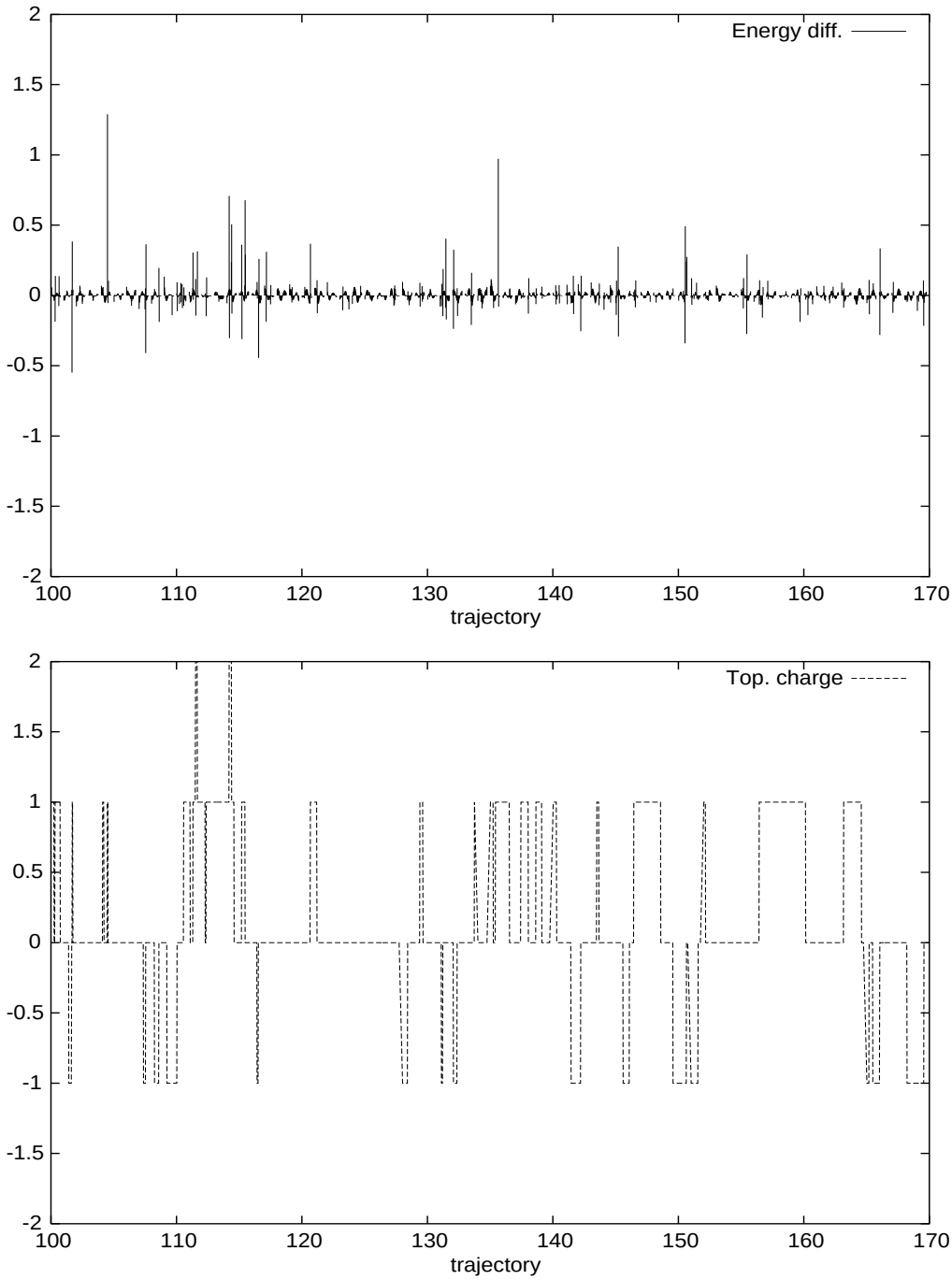

Figure 2.2: The energy difference between two micro-canonical steps and the topological index plotted against the trajectory number for 70 trajectories of an ensemble with $\beta = 5.4$, $\mu = 0.5$, and $\kappa = 0.225$, generated with the correction step.

4^4	$\mu = 0.5$	4^4	$\kappa = 0.225$	6^4	$\kappa = 0.2$	8^4	$\kappa = 0.2$
κ	n_{top}	μ	n_{top}	μ	n_{top}	μ	n_{top}
0.18	0.000(0)	0.05	0.045(12)	0.05	0.040(14)		
0.19	0.006(6)	0.1	0.103(20)	0.1	0.074(18)	0.1	0.153(42)
0.2	0.122(31)	0.2	0.393(39)				
0.21	0.579(30)	0.3	0.567(46)	0.3	0.547(74)	0.3	0.969(175)
0.22	0.901(104)	0.4	0.827(52)				
0.23	1.21(83)	0.5	1.12(73)				

Table 2.4: The number of topological index changes per trajectory (n_{top}) for various masses on our 4^4, $\kappa = 0.225$ ensembles (left), the 4^4, $\mu = 0.5$ ensembles (middle), and the 6^4, $\kappa = 0.2$ ensembles (right). Note that the 4^4 and 6^4 ensembles were generated at different values of κ (and β), so the bare quark mass at constant μ is 20% lower for the 6^4 ensembles.

The correction step and the number of topological index changes

The correction step algorithm was designed to conserve energy, even if there is a discontinuity in the overlap operator. Such a discontinuity is caused by a kernel eigenvalue crossing zero. If this eigenvalue changes sign, so does the topological index. To check whether energy conservation is maintained, we, therefore, monitor both, the (ferminonic) topological charge and the energy difference before and after an MD update.

Without the transmission/reflection step, we should see large spikes in the energy difference, when a change in topology is attempted. This is shown in fig. 2.1. The energy conservation of the MD is clearly violated and thus there is no acceptance when there is an attempt to change topology.

The opposite picture emerges when the correction step is switched on, see fig. 2.2. There are considerably less spikes in the energy difference, and the simulation stays in sectors with nontrivial topology, proving that the transmission step works well. Both simulations of fig. 2.1 and fig. 2.2 used the same parameters, thus proving that this aspect of the algorithm indeed works as expected.

As can be seen from tab. 2.4, the rate of tunneling between sectors with different topological index becomes smaller as the quark mass is decreased. However, it appears that the problem is less severe on larger volumes. But since the quark masses used for these runs are rather large, even on the 8^4 lattice the tunneling rate will become small already at a quark mass close to the strange quark mass.

The algorithm presented in the following section (section 2.4) solves this problem.

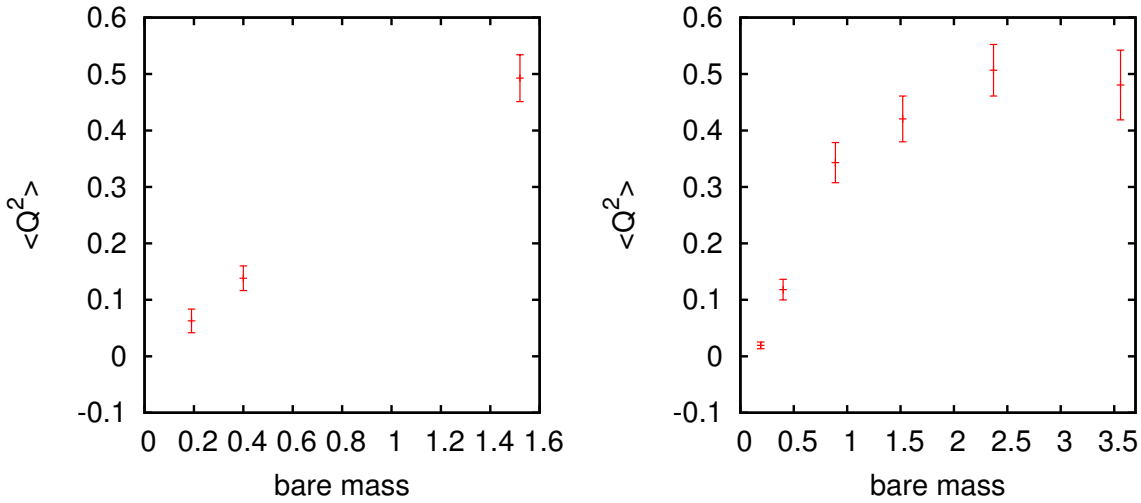

Figure 2.3: The ensemble average of Q_f^2 plotted against the bare quark mass on the 6^4 (left) and 4^4 (right) ensembles.

Topological susceptibility

The topological susceptibility, which is proportional to $< Q_f^2 >$, can be related to the quark mass using chiral perturbation theory [63–65]. It is expected that at low quark masses on large enough volumes the topological susceptibility should be proportional to the quark mass, *i.e.* the square of the pion mass:

$$\chi = \frac{< Q_f^2 >}{V} \sim \frac{f_\pi^2 m_\pi^2}{2N_F} + O(m_\pi^4).$$

At larger quark masses the topological susceptibility should tend asymptotically towards its quenched value. The transition between the two forms, in a large volume, is expected to be around 50-90 MeV [66]. The bare quark masses used within these test runs can be estimated to range from about 100 MeV to a few GeV and should be in the transitional region between the two known limits: a linear decrease in the quark mass would not necessarily be expected.

However, there is a clear decrease in the topological susceptibility, and the results are not inconsistent with the expected functional form.

Scaling of the correction step with $\Delta\tau$

Another important property to analyze is the scaling of the energy violation caused by the transmission or reflection step with the MD step size $\Delta\tau$. We know that these errors

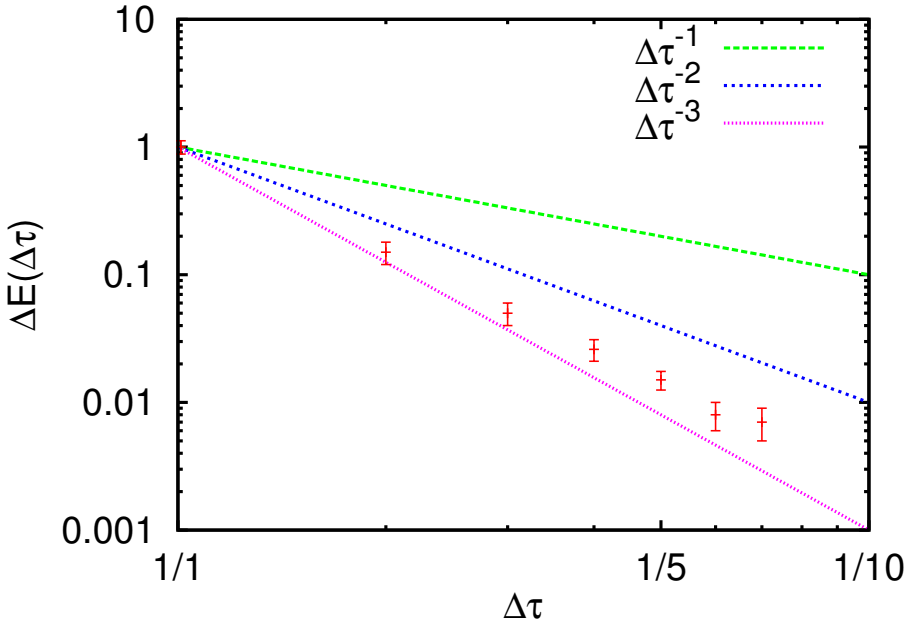

Figure 2.4: The energy violation by the correction step. The reference lines are from top down given by $\{\Delta\tau, \Delta\tau^2, \Delta\tau^3\}$

should scale with $\Delta\tau^2$ or better. To test the scaling properties numerically, the absolute value of the energy violation of the correction step was measured on 100 configurations of the $V = 6^4$, $\mu = 0.3$ ensemble. At the crossing the step size was varied according to $\Delta\tau/n_\tau$ with $n_\tau = 1, \ldots, 7$ and the measured value of the energy violation then averaged over the configurations. As can be clearly seen in fig. 2.4, the correction step indeed scales as expected with errors $O(\Delta\tau^2)$ or better.

2.3.7 Conclusion

In this section we have discussed an improved integrator to be used in an HMC with dynamical overlap fermions with two degenerate quark flavors. We have reviewed numerical results and have seen that this algorithm works as expected. The features of the algorithm are:

- The energy violations related to changes in the topological charge that cause the generic HMC to fail are absent or largely reduced by the correction step update.
- The scaling of the energy violations with the MD step size are comparable or better than $O(\Delta\tau^2)$.

- The scheme used to construct the correction step update can be extended to *e.g.* improve the energy conservation properties.
- The algorithm is reversible and satisfies area conservation.
- The transmission rate of the basic correction step HMC however depends strongly on the quark mass.

These methods are the basis for the more advanced algorithms of [49, 55, 60]. They are also the starting point of the methods aiming at increasing the transmission rate [20, 50], which we will discuss in the following section.

2.4 HMC algorithm with determinant factorization

We have seen in the previous section, that the probability for the simulation to tunnel through a topological barrier is a function of the quark mass μ. At least for the correction step algorithm this probability may become very low as the quark mass is decreased.

Assuming that the conjugate momentum Π of the MD integration can be described by a Gaussian distribution, the transmission rate, which we define as the number of transmission steps divided by the total number of transmission and reflection steps, is [20]

$$R = \min(1, e^{-\Delta S}),$$

with the action jump ΔS (see eqn. (2.15)). For a sufficiently large volume, the transmission rate is given by this formula for all possible energy and area conserving transmission algorithms. While it is possible to improve the transmission rate using non-area conserving algorithms [55], the dependence on the mass remains the same. To have a large transmission rate, and thus small auto-correlation, it is necessary to reduce ΔS.

More precisely, ΔS scales as $O(\mu^{-2})$ when the fermion determinant is estimated by a single pseudo-fermion [20]. Therefore, at low masses, topological charge changes are practically impossible. We will see below that using multiple pseudo-fermions reduces this problem, but does not eliminate it.

However, it was noted in [51, 67] that the change in the actual fermion determinant, as opposed to the pseudo-fermion estimate of it, scales much better with the quark mass, and one can argue that the dominant terms in the mean discontinuity are $O(1)$ [20]. Therefore, if we were to use the actual determinant, rather than the pseudo-fermion estimate, the bad scaling of the topological auto-correlation time with the mass would not occur. Of course, in practice, this is impossible.

There is another possibility, which is to factorize the determinant into two terms: a larger continuous determinant that can be treated with pseudo-fermions; and a smaller determinant that contains all the discontinuities and which can be treated exactly. In principle, this should combine the low ΔS of the exact determinant, with the better volume scaling of the pseudo-fermion estimate. Here, we will concentrate on one algorithm, which we will call algorithm C, following the notation in [20]. This algorithmic setup has meanwhile been tested on lattices with volumes ranging $8^3 \times 16$ to $16^3 \times 48$, see section 2.4.3.

Improving the transmission rate is the key to optimizing the efficiency of a dynamical overlap algorithm. Any transmission/reflection update requires a considerable amount of computer time: the exact MD time of the crossing has to be found, kernel eigenvalues and eigenvectors need to be recalculated and several inversions of the overlap operator need to be performed. These costs are only justified when the autocorrelation is reduced by a topological index change. In this sense, only the reflection step is costly. Since the density of small kernel modes increases with the volume, we can expect the transmission/reflection part of the algorithm to dominate on larger lattices. However, the auto-correlation time should decrease as the number of successful topological index changes increases. An efficient algorithm will therefore have as few reflections as possible, and, therefore, a maximized transmission rate.

The determinant factorization algorithm we will discuss in this section improves the tunneling of the overlap Hybrid Monte Carlo by a significant factor, and the cost of the factorization is far less than the gain from reduced auto-correlation. This gain will increase at smaller mass.

2.4.1 Motivation

A possible way of increasing the tunneling rate is to use multiple pseudo-fermions [67,68]. For example, simulating the fermion determinant using

$$\det H^2 = \exp\left\{ \langle\phi_1| \frac{1}{H(\mu_1)^2} |\phi_1\rangle + \langle\phi_2| \frac{H(\mu_1)^2}{H(\mu)^2} |\phi_2\rangle \right\}$$

gives [20]

$$\Delta S = \alpha \mu_1^{-2} + \beta \frac{\mu_1}{\mu} + \gamma \frac{(\mu_1^2 - \mu^2)^2}{\mu^2} + O(\mu^0), \tag{2.25}$$

where α and β are constants which need to be determined. In principle, by adding more pseudo-fermions, we can reduce the action discontinuity considerably. However, as the

mass decreases, it is necessary to add more pseudo-fermions. The optimum number and masses of the extra pseudo-fermion fields for force factorization will not necessarily be the same as the optimum for improving the tunneling rate. Also, even if multiple timescales are used, this will increase the time required for each trajectory. And because of the dependency of ΔS on μ and the μ_i, as indicated (for one additional pseudo-fermion) in eqn. (2.25), even for arbitrarily many pseudo-fermions this method cannot produce a ΔS that is independent of the quark mass.

An alternative approach is to factorize the discontinuity from the pseudo-fermion term, and treat the discontinuous part of the action exactly. One way of doing this is to use a projector P constructed from the smallest n kernel eigenvectors. We can write

$$\begin{aligned}\det[H] = &\det\left[1 - P\frac{1}{PHP}PH(1-P)\right]^{-1} \det\left[1-(1-P)HP\frac{1}{PHP}P\right]^{-1} \\ &\det\left[PHP + (1-P)H(1-P) - (1-P)HP\frac{1}{PHP}PH(1-P)\right]\end{aligned} \tag{2.26}$$

If the projectors are exact, so that $P^2 = P$, then the first two determinants on the r.h.s. of equation (2.26) are 1 and the third determinant can be further factorized into the product of

$$\det\left[PHP + (1-P)\right] \tag{2.27}$$

and

$$\det\left[(1-P)H(1-P) - (1-P)HP\frac{1}{PHP}PH(1-P) + P\right]. \tag{2.28}$$

This is the familiar Schur decomposition. The projectors P could in principle be constructed using $P = 1 - \sum_{i=0}^{n} |\psi_i\rangle\langle\psi_i|$. The first determinant, (2.27), is then continuous when a kernel eigenvalue crosses zero, and can be treated with pseudo-fermions. The second determinant, given in equation (2.28), is discontinuous, but the matrix is small enough for the determinant to be calculated exactly, and to be explicitly included in the action without pseudo-fermions. Of course, the determinant given in equation (2.27) is discontinuous when there is a level crossing between the nth and $(n+1)$th eigenvalues. To avoid this, without resorting to another transmission/reflection step, it is necessary to use projectors which are a function of the eigenvalue, which means that it is impossible to satisfy $P^2 = P$. While this decomposition is still possible, we cannot neglect the first two determinants in equation (2.26), and the third determinant cannot be factorized so easily. The algorithm (alg. C) we will discuss in the next section uses simpler means to achieve the same goal.

2.4.2 Determinant factorization

Algorithm A

Algorithm A was introduced in the context of dynamical overlap simulations in [67]. It reduces the noise of the pseudo-fermion approximation by introducing n additional pseudo-fermions, following the method of Hasenbusch [68]:

$$\begin{aligned}\det(H(\mu)) =& \det\frac{H(\mu)}{H(\mu_1)}\det\frac{H(\mu_1)}{H(\mu_2)}\ldots\det(H(\mu_n)),\\ S_{pf} =& \phi_1^\dagger H(\mu_1)H(\mu)^{-2}H(\mu_1)\phi_1 + \phi_2^\dagger H(\mu_2)H(\mu_1)^{-2}H(\mu_2)\phi_2 + \ldots +\\ & \phi_{n+1}^\dagger H(\mu_n)^{-2}\phi_{n+1}\end{aligned}$$

This decomposition was originally introduced to precondition the fermionic force, and as such a few additional pseudo-fermions are needed for an efficient algorithm at low mass. As discussed in the previous section, it can also be used to reduce the action discontinuity. Here alg. A will be used with one additional pseudo-fermion as a benchmark against which the results of the new method will be compared.

Algorithm C

As mentioned before, it is preferable to avoid the extra cost of both an additional correction step or of the two additional terms in eqn. (2.26) necessary if the Schur decomposition of the fermion determinant was used. Instead, we use an eigenvalue projector which depends on a continuous function α of the kernel eigenvalue.

$$\begin{aligned}\tilde{H}_C =& (1+\mu)\gamma_5 + (1-\mu)\mathrm{sign}(Q)\left(1-\sum_i \alpha(\lambda_i)|\lambda_i\rangle\langle\lambda_i|\right),\\ \det H =& \det[\tilde{H}_C]\det\left[1+(1-\mu)(\mathrm{sign}(Q)\sum_i \alpha(\lambda_i)|\lambda_i\rangle\langle\lambda_i|)\frac{1}{\tilde{H}_C}\right],\end{aligned} \tag{2.29}$$

where $\alpha(0)=1$ and $\alpha(\lambda\geq\Lambda)=0$ for a carefully tuned eigenvalue cutoff Λ. The first of the determinants in equation (2.29) is a continuous function at $\lambda=0$, so it will not contribute to the action jump. The second can be written as

$$\begin{aligned}D_C =& \det\left[1+(1-\mu)|\lambda_i\rangle\langle\lambda_i|\left(\mathrm{sign}(\lambda_i)\alpha(\lambda_i)\right)\frac{1}{\tilde{H}_C}\right]\\ =& \det\left[\delta_{ij}+(1-\mu)\langle\lambda_i|\left(\mathrm{sign}(\lambda_i)\alpha(\lambda_i)\right)\frac{1}{\tilde{H}_C}|\lambda_j\rangle\right].\end{aligned} \tag{2.30}$$

This is the determinant of an $n \times n$ matrix, which can be calculated easily using, for example, LU decomposition [57]. It has been proposed to account for this determinant by re-weighting, or by including the correct expression in the Hybrid Monte-Carlo Metropolis step, but this leads to a low acceptance rate and hence an algorithm that is only a small improvement over alg. A [69]. Therefore, we will be adding the logarithm of this determinant to the fermion action. This obviously costs more per trajectory, both because of the additional term in the fermionic force and because, since D_C is discontinuous at the eigenvalue crossing, requires tracking the eigenvalues of the kernel operator and the reflection/transmission routine to account for the discontinuity in the action. However, including the additional term in the action gains by maintaining a high Monte-Carlo acceptance rate. In the numerical tests $\alpha(\lambda) = \text{sign}(\lambda)Z(\lambda)$ was used, where Z is the same Zolotarev rational approximation used to approximate the sign function. With this choice, there is no need to project out the eigenvalues when calculating $\tilde{H}_C$. In principle, the choice of α is arbitrary, and can be tuned to maximize the HMC acceptance rate or, more importantly, the stability of the algorithm.

The fermion action is thus (with no additional Hasenbusch pseudo-fermion terms):

$$S_{pf} = \phi^\dagger \frac{1}{\tilde{H}_C}\phi - 2\log(D_C). \tag{2.31}$$

The determinant can be differentiated easily, by differentiating each component of the matrix, and multiplying it by the co-factor of that component. As an illustration, for a 3×3 matrix, we write

$$\frac{d}{d\tau}\log(\det[a]) = \frac{1}{\det[a]}\frac{da_{11}}{d\tau}\det\begin{bmatrix} 1 & 0 & 0 \\ 0 & a_{22} & a_{23} \\ 0 & a_{32} & a_{33} \end{bmatrix} + \frac{1}{\det[a]}\frac{da_{12}}{d\tau}\det\begin{bmatrix} 0 & 1 & 0 \\ a_{21} & 0 & a_{23} \\ a_{31} & 0 & a_{33} \end{bmatrix} + \ldots. \tag{2.32}$$

The eigenvectors and eigenvalues can be differentiated following the methods in the previous section with the improvements in [49].

2.4.3 Numerical results

In this section we look at numerical results for both alg. A and C on a $8^3 \times 16$ lattice at masses $\mu = 0.03$, $\mu = 0.04$ and $\mu = 0.05$, corresponding to pion masses of $450 - 550$ MeV (calculated from the pseudo-scalar correlator) at lattice spacings of about $a = 0.11$ fm (calculated using $r_0 = 0.49$ [70]). These masses are as low as they could be achieved on these

μ	μ_1	A	C	A	C	A	C
0.03	0.17	14.0(7)	0.28(8)	21.9	0.78	9.6%	77.5%
0.04	0.22	13.8(10)	0.59(11)	19.5	0.77	9.2%	75.2%
0.05	0.22	7.8(4)	0.24(7)	13.6	0.72	18.3%	70.1%

Table 2.5: Average values of ΔS (left) standard deviations of ΔS (middle) and transmission rates (right) for alg. A and C.

lattice volumes while remaining in the topologically active p-regime. A tadpole improved Lüscher-Weisz gauge action [71, 72] and two steps of stout smearing were used, with an otherwise standard Wilson kernel at smearing parameter $\rho = 0.1$. The MD integration was performed using the improved Omelyan integrator [31, 32]. Furthermore, one additional flavor of Hasenbusch fermions was included, for both algs. A and C. The Hasenbusch mass (μ_1) was the same for algs. A and C, but was varied trying to optimize ΔS for alg. A for each quark mass. However, the choice of μ_1 turned out to be sub-optimal at $\mu = 0.04$.

Between 120 and 500 trajectories were generated for each of the ensembles, and all ensembles had over 170 attempted topological index changes. The trajectory length was 0.5 with 20 integration steps, which achieved a Monte Carlo acceptance rate of over 90% in all cases.

The mean values of the action jump at the topological sector boundary, ΔS, standard deviation of ΔS, and the transmission rates are given in tab. 2.5, together with the Hasenbusch mass μ_1. The distribution of ΔS is shown in fig. 2.5.

It can be seen that alg. C has a far lower action jump than alg. A, and a much smaller spread of ΔS. This corresponds to a much larger transmission rate. However, the pion masses used are still large, and thus the gain should be far larger at more realistic masses. As expected, the mass dependence of the transmission rate for alg. C is not significant, while for alg. A it has a strong dependence on the quark mass.

The increased transmission rate of alg. A corresponds to a reduction in the topological autocorrelation time of about a factor of 8. The extra cost of the additional inversions meant that it took twice as long to generate the trajectory (measured on the $\mu = 0.04$ ensemble), meaning that the overall gain of this method was roughly a factor of 4. This was without using any Sexton-Weingarten [33] methods to place the small determinant on a reduced time-scale, and at a relatively large quark mass. In summary, one can expect an even larger gain for simulations at bigger lattice volumes and smaller pion masses.

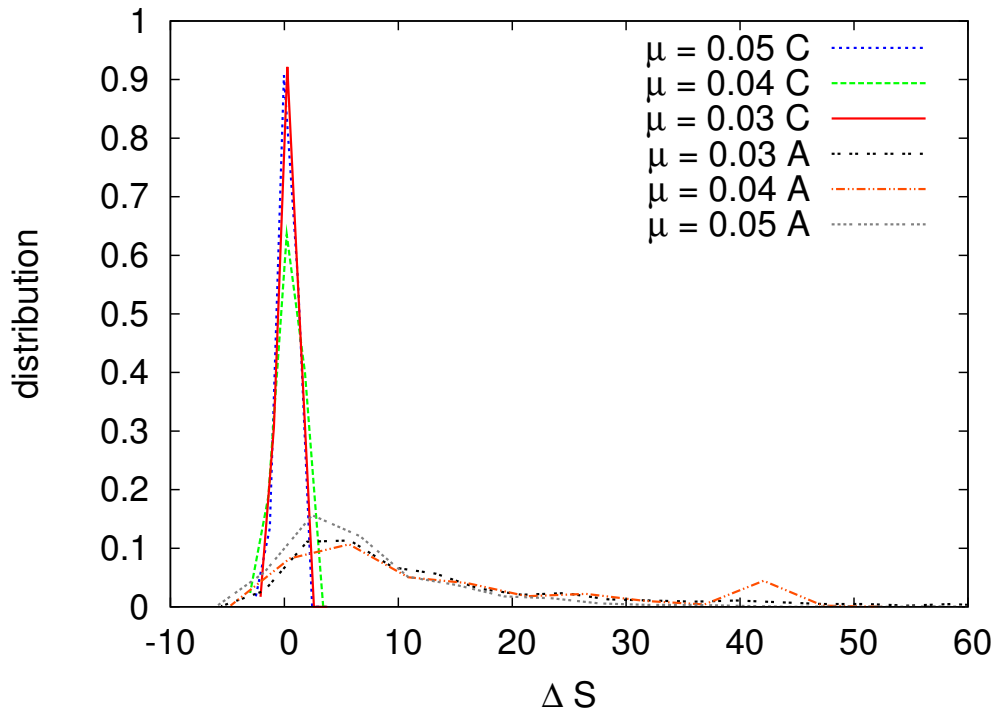

Figure 2.5: The distribution of ΔS for masses $\mu = 0.03$, $\mu = 0.04$, and $\mu = 0.05$ for algs. A and C.

2.4.4 Conclusion

The topological auto-correlation time limits dynamical lattice QCD simulations, particularly those involving overlap fermions. The algorithm we discussed in this section, solves or at least largely reduces this problem. This is done by factorizing the fermion determinant into a large continuous matrix approximated by pseudo-fermions and a smaller discontinuous part treated exactly. Topological tunneling can then be observed even at small quark masses. With this method, the discontinuity in the pseudo-fermion action is independent of the quark mass, and it can be expected to be largely independent of the lattice volume as well. The algorithm is found to work as predicted on $8^3 \times 16$ and $8^3 \times 32$ lattices (see also [73]). Preliminary results show that the method continues to work well on lattices as large as $16^3 \times 48$.

2.5 Summary and conclusion

In this chapter, we have discussed how to adapt the generic HMC algorithm to simulations with dynamical overlap quarks. The main advantage of overlap fermions, the exact lattice chiral symmetry with the connected index theorem, turns out to be the biggest obstacle for such an algorithm. Anytime the simulation attempts to cross over the boundary separating sectors with different topological index, a discontinuity in the fermion action appears. It can be successfully treated with the transmission/reflection algorithm of section 2.3.

Although with this algorithm crossing between sectors is possible, it is found to become less probable as the quark mass is decreased. This is caused by the pseudo-fermion estimate of the quark determinant, which overestimates the discontinuity in the action. Thus, most of the time when the simulation attempts to change the topological sector, it will not tunnel through the sector boundary, but rather reflect off it. As a consequence the autocorrelation time increases while the computational costs remain the same or, when switching to a larger volume, increase as well.

In section 2.4 we discussed an algorithm that can in principle solve this problem and we saw numerical evidence confirming that it works as predicted. While simulations with dynamical overlap fermions remain considerably and maybe even $O(100)$ more expensive than simulations with conventional fermions, with this new algorithm simulations on medium to large lattice are in the reach of future supercomputers of the 100 TFlop/s to 1 PFlop/s class.

A highly precise calculation of the masses of strongly interacting particles, based on fundamental theory, is testament to the age-old verity that physical reality embodies simple mathematical laws.

Frank Wilczek [21]

Chapter 3

The light hadron sector with improved Wilson Fermions

The overlap fermion algorithms of the previous chapter are significantly more costly in terms of computer time than simulations based on generic Wilson fermions. However, only a few years ago it was believed that the opposite could be true. As mentioned in the introduction, extrapolations showed that simulations using generic Wilson quarks would not be able to reach pion masses that, judging from what we know today, would be small enough for chiral extrapolations to be trusted ("critical slowing down") [74–77]. Simulations with dynamical "chiral" fermions, like the overlap formulation, at that time were considered to be a possible remedy for this problem. This assessment was based on the observation that, in opposition to Wilson fermions, with the additive quark mass renormalization being excluded by chiral symmetry, a precise lower bound on the spectrum of these chiral Dirac operators could be given. And indeed, simulations based on these formulations are safe from the problematic fluctuations of the small eigenmodes present in simulations with Wilson quarks.

However in the following years it was realized[1] that the different improved algorithms of the past decades [10, 32, 33, 68, 80, 81] could actually be combined, and that the resulting algorithm, in terms of the gain, was far more than the sum of its parts [22, 82–84]. These studies showed that this combined scheme constitutes a dramatic improvement of the above scenario. And additionally, as we will discuss in this chapter, if the action used for the simulation is chosen properly, the computational costs can be reduced even further.

[1] A completely different and comparably efficient approach was taken by M. Lüscher with the "domain decomposed" HMC, see *e.g.* [78, 79] and references therein.

In the quenched theory, it is a well known fact that the combination of Symanzik improved [85] Wilson ("clover") fermions and link averaging ("smearing") results in a Dirac action with significantly improved chiral properties [86–91]. In a dynamical simulation this not only translates into a reduced additive quark mass renormalization, but the smearing also tames the fluctuations of the eigenvalue spectrum. This in turn improves the convergence rate of the linear solvers and through that reduces the total costs of the simulation.

Reduced costs are, however, not the only advantage of such an action. Due to the smearing, the theoretically leading $O(\alpha_s a)$ contributions are, in practice, absent, and extrapolations to the continuum appear to be dominated by $O(a^2)$ cut-off effects, consistent with an $O(a)$ improved theory. Furthermore, contributions of unphysical tadpoles are greatly reduced; renormalization constants are generally closer to their tree level values, and c_{SW} is not far from 1 at typical lattice spacings.

All this suggest that this combination of systematic improvements of action and algorithm (see section 3.1) will allow simulations with a shorter extrapolation range in the pion mass, with a smoother continuum limit and consequently with an unprecedented level of accuracy. As we will see below, this is indeed the case.

To be precise, all results presented in this chapter are obtained using a tree-level Symanzik improved gauge action [92] and six-step, stout-smeared clover fermions with the clover coefficient set to its tree-level value. This choice allows for an efficient simulation while delivering excellent scaling properties, as will be shown in the detailed scaling study of section 3.3.

In section 3.4 the simulations are extended by a total of 20 different $N_f = 2+1$ ensembles with pion masses reaching down to 190 MeV in a calculation of the light hadron spectrum of QCD. This large number of ensembles makes it possible to control all sources of systematic errors – the simulation, therefore, provides a high-precision ab initio determination of the light hadron masses as predicted by QCD.

The remainder of this chapter is organized as follows. In section 3.1 the details of the action and simulation algorithm are given, which will then be tested in section 3.2. Section 3.3 contains the scaling study, and we will discuss the spectrum calculation in section 3.4. The chapter is then concluded with an outlook in section 3.5.

3.1 Action and algorithm

In this section we will discuss the properties of the tree-level Symanzik improved action and the improved simulation algorithm in more detail. We will begin with the action and

then move on to discuss the specifics of the algorithm. In the next section, this setup will be tested to make sure it is suitable for a large scale simulation at small pion masses.

3.1.1 Action

The explicit form of the gauge and fermion actions in terms of the thin ($U_{n,\mu}$) and smeared ($V_{n,\mu}$) gauge links is as follows:

$$\begin{aligned} S &= S_G^{\mathrm{Sym}} + S_F^{\mathrm{SW}}, \\ S_G^{\mathrm{Sym}} &= \beta \left[\frac{c_0}{3} \sum_{\mathrm{plaq}} \mathrm{Re}\,\mathrm{Tr}\,(1 - U_{\mathrm{plaq}}) + \frac{c_1}{3} \sum_{\mathrm{rect}} \mathrm{Re}\,\mathrm{Tr}\,(1 - U_{\mathrm{rect}}) \right], \\ S_F^{\mathrm{SW}} &= S_F^{\mathrm{W}}[V] - \frac{c_{\mathrm{SW}}}{4} \sum_n \sum_{\mu,\nu} \overline{\psi}_x \, \sigma_{\mu\nu} F_{\mu\nu,n}[V] \, \psi_x \,, \end{aligned} \tag{3.1}$$

with the standard Wilson action S_F^{W}. The parameters c_{SW}, c_0 and c_1 set to their tree level values:

$$c_{\mathrm{SW}} = 1, \quad c_1 = -1/12, \quad c_0 = 1 - 8c_1 = 5/3 \,.$$

Both the hopping part and the clover improvement term in the fermion action S_F^{SW} use six-step stout-smeared links [93] $V_{n,\mu} \equiv V_{n,\mu}^{(6)}$. These are constructed from the thin links $U_{n,\mu} \equiv V_{n,\mu}^{(0)}$ according to

$$\begin{aligned} V^{(n+1)} &= e^{\rho S^{(n)}} U^{(n)}, \\ S^{(n)} &= \frac{1}{2}(\Gamma^{(n)} V^{(n)\dagger} - V^{(n)} \Gamma^{(n)\dagger}) - \frac{1}{6} \mathrm{Re}\,\mathrm{Tr}(\Gamma^{(n)} V^{(n)\dagger} - V^{(n)} \Gamma^{(n)\dagger}), \\ \Gamma_{n,\mu}^{(n)} &= \sum_{\nu \neq \mu} V_{n,\nu}^{(n)} V_{n+\nu,\mu}^{(n)} V_{n+\mu,\nu}^{(n)\dagger}. \end{aligned} \tag{3.2}$$

The stout smearing parameter is chosen to be $\rho = 0.11$, which is a rather conservative choice [88,93] corresponding to an $\alpha_{\mathrm{APE}} = 0.48$ with respect to the average plaquette [94]. In S_G^{Sym} only the unfiltered links are used.

This action is ultra-local: as is apparent from eqn. (3.1), the Dirac operator exclusively connects nearest-neighboring sites. The damping of unphysical UV modes is achieved by a modified - but still ultra-local - coupling to the gluonic background. To be more precise: the term locality is used in two different ways in the literature (see *e.g.* [95–97]). First of all (type A locality), in the sum $\sum_{x,y} \bar{\psi}(x) D(x,y) \psi(y)$ the non-diagonal elements of the clover Dirac operator $D(x,y)$ are by definition strictly zero for all (x,y) pairs except for nearest neighbors. The second aspect of locality (type B) is how $D(x,y)$ depends on the

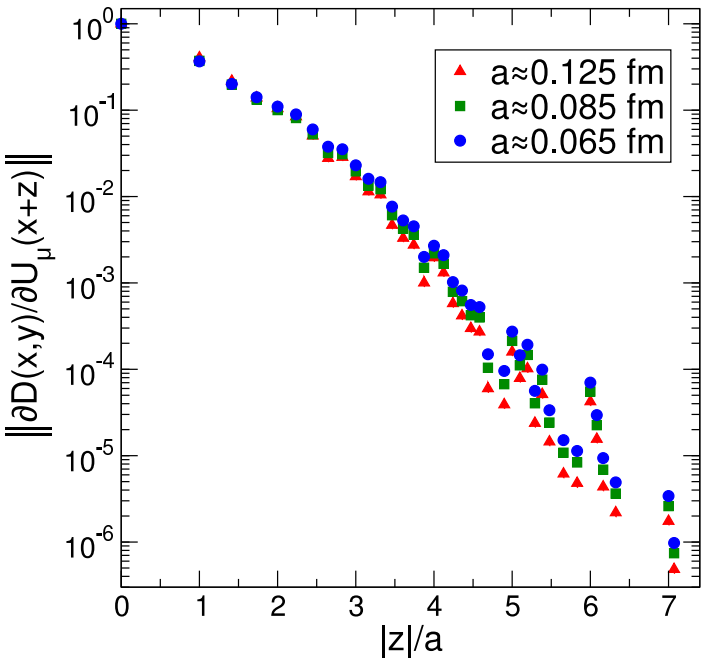

Figure 3.1: Locality properties of the Dirac operator used in the simulations. Shown here is the locality of type B (see text) for three different lattice spacings. In the analyses the Euclidian metric for $|z|$ was used. Shown is the Frobenius norm of the resulting antihermitian matrix summed over spin, color and Lorentz indices. An overall normalization is performed to ensure unity at $|z|$=0.

gauge field U_μ at some distance z: $\|\partial D(x,y)/\partial U_\mu(x+z)\|$. The action is by definition ultra-local, thus $\|\partial D(x,y)/\partial U_\mu(x+z)\|$ depends only on gauge field variables residing within a fixed range. Furthermore, within this ultra-locality range the decay is, in very good approximation, exponential with an effective mass of about $2.2a^{-1}$, see fig. 3.1. This is far larger than any of the masses considered in this chapter, even on the coarsest lattices used for the scaling study in section 3.3.

3.1.2 Simulation algorithm

Let us now come to the $N_f = 2+1$ simulation algorithm. The two degenerate quark flavors are implemented via the Hybrid Monte Carlo (HMC) algorithm [10], the third using the Rational Hybrid Monte Carlo (RHMC) algorithm [80, 81, 98–100]. To speed up the inversions, the fermion matrix is preconditioned using the even/odd scheme of [101]. As already mentioned in the introduction to this chapter, the generic HMC algorithm suffers from critical slowing down in the light-quark regime. To treat this problem, several improvements over the generic algorithm are used in combination (see also [22, 82–84]):

- *Multiple time-scale integration:* not all force contributions in the MD part of the HMC algorithm require the same amount of computational resources. Using multiple time-scale integration ("Sexton-Weingarten integration scheme") [33], it is possible to put each part of the MD on a different time scale according to its relative contribution to the total force, thus reducing the computational costs of the MD.

- *Mass preconditioning:* the pseudo-fermion force is used within the MD to include the effects of dynamical fermions. Through mass preconditioning, the UV part of the force can be split off and treated separately [68, 102, 103], which helps reducing the fluctuations in the force (see also section 2.4). The second important benefit of mass preconditioning appears when combined with the multiple timescale integration scheme [22,82–84]: the more expensive infrared part contributes less to the total force and can be integrated with larger time steps.

- *RHMC:* the third, unpaired quark flavor is implemented through the RHMC [80, 81, 98–100] algorithm. This algorithm makes use of the fact that the single fermion action can be written as $\xi^\dagger (M^\dagger M)^{-1/2} \xi$, where the inverse square root can in turn be approximated by a rational approximation and be efficiently calculated with a multi-shift solver. The RHMC is highly efficient in simulating a single quark flavor. It can also be combined with the multiple timescale integration scheme.

- *Omelyan integrator:* the MD integration within the generic HMC algorithms uses the leapfrog integration scheme. It proceeds by first integrating one half step in position space followed by a full step update of the conjugate momenta and finally another half step in position space (see also alg. 2.1). The Omelyan integrator [31, 32] adds a small momentum update (reduced by $\lambda \approx 0.193$) before and after the leapfrog step and shortens the original leapfrog momentum update by a factor $(1 - 2\lambda)$. This scheme improves the MD energy conservation by about one order of magnitude for a factor ~ 2 increase in computational cost. The use of a correspondingly larger step size then results in a net gain of about 50% [32].

As we will see throughout this chapter, this combined algorithm overcomes the problem of critical slowing down. It is used in the spectrum measurements we will discuss in section 3.4 and also for the $N_f = 3$ scaling study described in section 3.3.

3.1.3 Inversion algorithms

The most time consuming part, both in the valence and the sea sector, is the (approximate) fermion matrix inversion by means of a linear solver. These calculations generally require double precision accuracy. This is due to the fact that, in order to maintain reversibility at small quark masses, the MD part of the algorithm needs to be performed at least in double precision[2]. Double precision accuracy is also required in valence calculations at small quark masses, owing to the large condition numbers involved. However, this does not imply that each fermion matrix multiplication needs to be done in double precision. In the valence sector we need to solve

$$Dx = b \tag{3.3}$$

(with D in this case being the stout-link clover Dirac operator) to construct the correlators. To calculate the fermionic force in the MD part of the algorithm we need to solve

$$D^\dagger Dx = b. \tag{3.4}$$

In both cases it is possible to use a single precision version of D within mixed precision solvers to accelerate the inversion. There is basically no penalty in terms of the iteration count: for the parameters used in the simulations of this chapter, the increase in the number of matrix multiplications is well below 10%.

A simple and reasonably efficient way to construct a mixed precision solver is to use the standard "iterative refinement" technique, which amounts to repeatedly using a single precision solver. In this scheme, only the (outer) residuals and global sums are calculated in double precision; the inversion is performed with single precision accuracy. The single precision inversion typically uses the same algorithm that would be used for a full double precision inversion, such as BiCGstab to solve (3.3) or CG for (3.4). With $\mathbf{A} = D$ or $\mathbf{A} = D^\dagger D$ referring to the forward multiplication routine in double precision, $\mathbf{a}$ the single precision counterpart and ε the desired final double precision accuracy, the complete procedure reads:

1. Compute $r_i = b - \mathbf{A}x_i$
2. If $|r_i| \leq \varepsilon |b|$, exit
3. Solve $\mathbf{a}t_i = r_i$ in single precision to an accuracy ε', with $\tilde{t}_i$ denoting the solution.
4. Update $x_{i+1} = x_i + \tilde{t}_i$

[2] In order to make the algorithm exactly reversible up to full double precision accuracy, the link and momentum update is computed in quadruple precision.

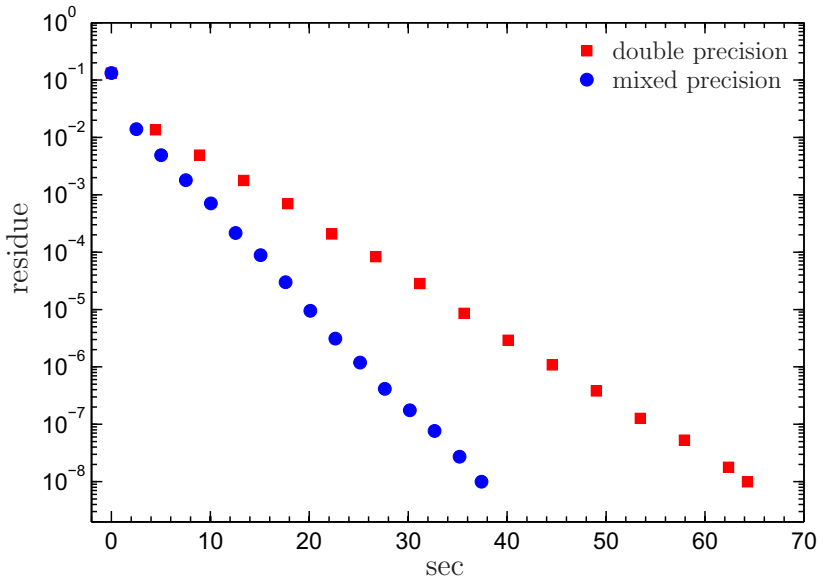

Figure 3.2: Performance of the CG algorithm in double precision (squares) compared to a mixed precision variant of CG (circles). The inversions were performed on a $32^3 \times 64$ lattice at $M_\pi \sim 250$ MeV from the $N_f = 2+1$ ensemble at $\beta = 3.57$ (see tab. 3.3).

5. Goto 1

With $s_i = r_i - \mathbf{A}\tilde{t}_i$ and $\delta \equiv |s_i|/|r_i| \approx \varepsilon' < 1$, we have

$$|r_{i+1}| = |b - \mathbf{A}x_{i+1}| = |b - \mathbf{A}x_i - \mathbf{A}\tilde{t}_i| = |b - \mathbf{A}x_i - r_i + s_i| = |s_i| = \delta|r_i| < |r_i| \,.$$

Thus, as long as the single precision inversion does not fail, the method will converge. Since many single precision matrix multiplications are needed to compute $\tilde{t}_i$, compared to just one double precision multiplication with $\mathbf{A}$ in the outer iteration, the whole solver is dominated by the single precision matrix multiplication performance, resulting in a significant speedup over a full double precision inversion (see Fig. 3.2).

3.1.4 Software implementation

Performance optimization for the IBM Blue Gene/L

The performance of generic MPI/C software on the Blue Gene/L necessitated a thorough optimization of the simulation code. This problem was caused by a combination of limitations on the side of the "ppc440" core and the complex SIMD instruction set of the attached FPU, which makes automatic code optimization often too difficult for the compilers [104].

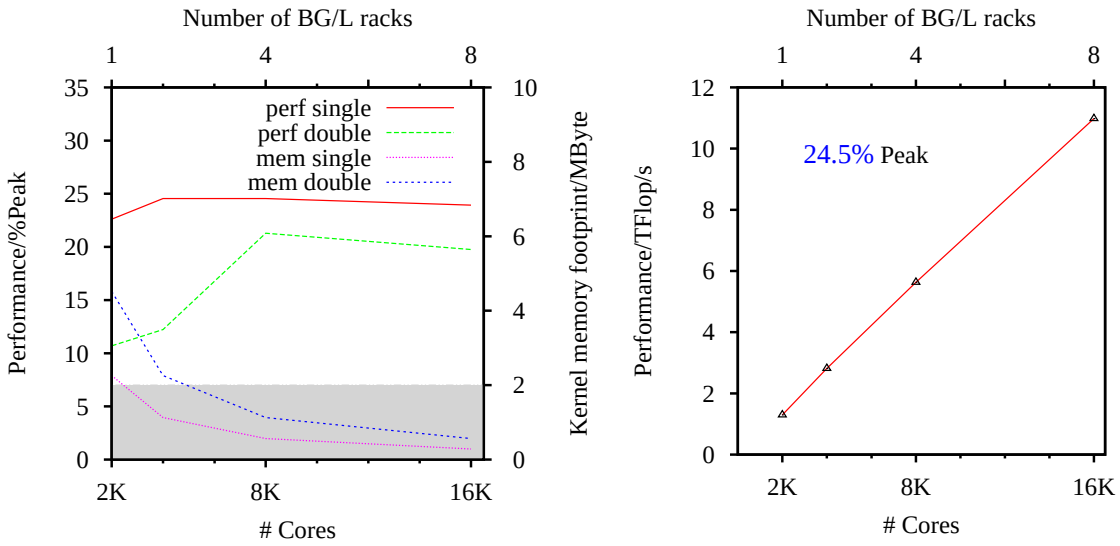

Figure 3.3: Performance of the Blue Gene/L implementation. Shown is a strong scaling analysis of a $48^3 \times 96$ lattice. The gray shaded area gives the L3 cache size.

To that end, because of its impact on the overall performance of the HMC, all scalar parts of the clover operator were written in hand tuned assembly code. Additionally, other routines that proved to be performance critical were optimized using the built-in functions of the IBM XL C compiler. These provide an "assembler generator" type functionality, where the user has to pick the exact floating point assembly instruction that is to be used and has to provide information about the data flow, but the scheduling of instructions will be done by the compiler. The efforts that went into this optimization actually payed off twice: since the same FPU is also used on the Blue Gene/P, the assembly code, apart from some minor reordering to account for the difference in caching policies, could be reused on the Blue Gene/P.

Communication. The Blue Gene/L, again like the Blue Gene/P, features a 3-dimensional torus network, which is perfectly suited for a parallel LQCD code. To make sure latencies are minimal, the torus network was used directly, by having the CPU copy data into the appropriate torus FIFOs. To simultaneously optimize all communication operations of the code, a low level software layer was designed. This layer contained optimized routines for all necessary communication operations, including global sums or barriers. The HMC was then adapted and completely based on this layer – no MPI or other high level libraries were used. It showed good scaling properties up to the full Blue Gene/L installation at Forschungszentrum Jülich (see fig. 3.3), and reached a sustained performance of up to

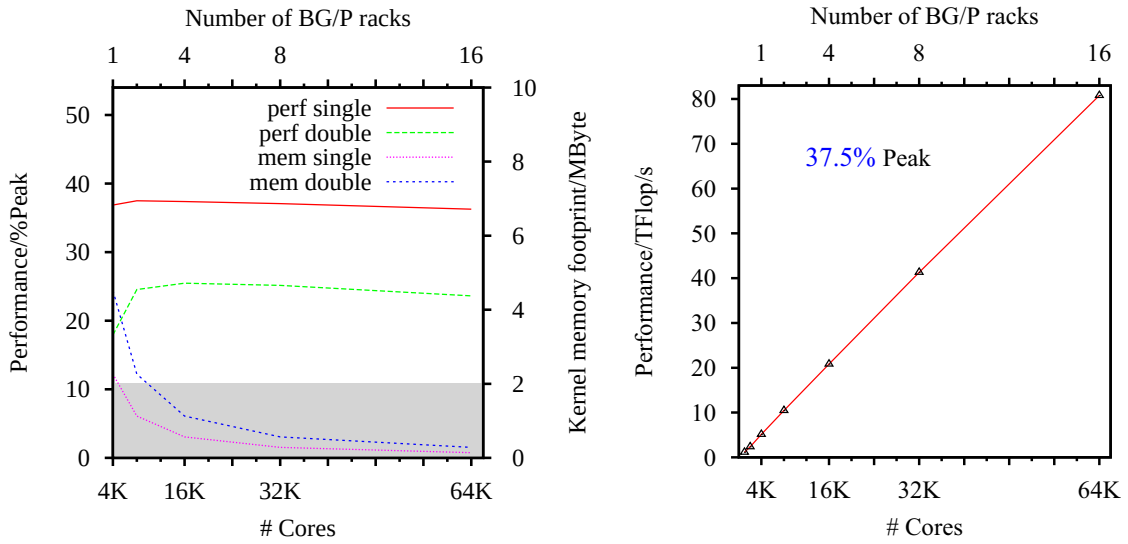

Figure 3.4: Performance of the Blue Gene/P implementation, developed and optimized for demonstrating strong scaling up to the full 65536 CPUs of the Blue Gene/P at JSC, with an impressive sustained performance of 80 TFlop/s. Shown is a strong scaling analysis of a 64^4 lattice. The gray shaded area gives the L3 cache size.

26% of machine peak (on a $32^3 \times 64$ lattice running on 8 Racks) .

Performance optimization for the IBM Blue Gene/P

In order to also make optimal use of the Blue Gene/P, the communication layer was adapted to fully use its new capabilities. Most of the code that had already been tuned for the Blue Gene/L could, with minor modifications, simply be used again. However, since the efficiency of compiler generated code proved to be slightly worse than on the Blue Gene/L, a significant number of additional routines had to be optimized (see below). The good scaling properties of the Blue Gene/P implementation are apparent from the scaling plots of fig. 3.4, which shows a strong scaling analysis from one Rack of the Blue Gene/P in Jülich up to the whole 16-rack machine. The scaling is almost perfect and peaks at a sustained performance of 37.5% of machine peak.

Communication. The new communication library uses the low level SPI software interface. This thin layer contains wrapper functions for compute node kernel calls and allows direct hardware access for user space applications. With the SPI it is possible to make best use of the hardware capabilities avoiding latencies from high level libraries such as DCMF or MPI.

Especially important for efficient communication routines is the ability to directly control the Blue Gene/P's DMA. By explicitly injecting message descriptors into a dedicated injection FIFO and by resetting the FIFO head it is possible to implement persistent communications, which cuts the time required to start the communication process down to a minimum. This functionality is not accessible through DCMF or MPI. Additionally, this way all communication inside the kernels perfectly overlap with the computations. The performance of the serial Clover operator for instance is virtually unchanged when the communication is switched on.

The communication layer is completely based on the SPI software interface. It contains all required communication routines, such as global sums or broadcasts, persistent or generic communication routines as well as global and node barriers to synchronize all cores or the cores of a single node. The simulation code itself is again completely based on this new layer.

Serial code optimization. In order to be able to optimize large fractions of the code, a set of macros was used that implements - via the built-in functions - the basic mathematical operations that are required, such as $SU(3)$ matrix matrix or matrix vector multiplications or spinor manipulation routines. Using these macros, all remaining compute intense parts of the simulation code could be efficiently optimized. Combined with extensive manual reordering of loops to deal with the limited instruction flow manipulation capabilities of the Blue Gene/P's "ppc450" core, almost always a speed up of at least a factor of 3 over the plain C code could be achieved.

3.2 Algorithm verification

3.2.1 Spectral gap

In quenched QCD, the (unsmeared) clover fermion operator may have one or several eigenvalues close to the origin or with a negative real part, even for not very light quark masses. Configurations for which this is the case are referred to as "exceptional".

If one integrated the HMC trajectories exactly, any such configuration would be absent in full QCD, since an eigenvalue of the hermitian Wilson operator $H_{\mathrm{W}} = \gamma_5 D_{\mathrm{W}}$ approaching zero would induce an infinite back-driving force in the HMC. In practice, when the trajectories are generated with a finite step-size integrator, the near zero modes along a trajectory are only approximately suppressed. This may cause a breakdown of the MD evolution. It

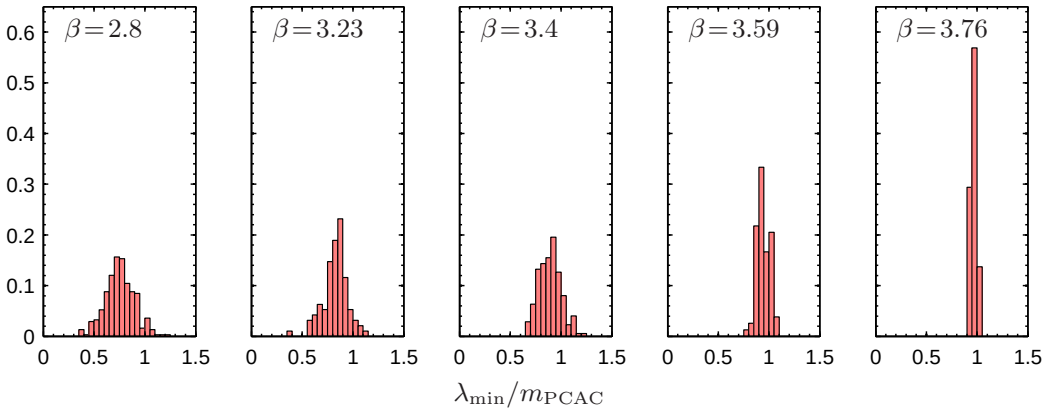

Figure 3.5: The magnitude of the smallest eigenvalue of the preconditioned hermitian Dirac operator in units of the PCAC mass. At each β the lightest run ($M_\pi/M_\rho \simeq 0.6$) of the scaling study (section 3.3) is shown.

is therefore natural to monitor the smallest eigenvalue (in magnitude) of H_{W} and check if it is sufficiently far from the origin throughout the entire run. In a given ensemble this spectral gap shows a more-or-less Gaussian distribution, and as long as its median is several σ away from zero, the simulation is deemed safe [105].

Since even-odd preconditioning is used, the relevant quantity to monitor is the smallest eigenvalue of the hermitian counterpart of the reduced operator $D_{\mathrm{r}} = \frac{1}{2}(D_{\mathrm{oo}} - D_{\mathrm{oe}} D_{\mathrm{ee}}^{-1} D_{\mathrm{eo}})$, which is γ_5-hermitian. Here a factor $1/2$ is included to have the IR eigenvalues almost aligned with the low-lying eigenvalues of the full operator. For the lightest mass ($M_\pi/M_\rho = 0.60$) used in the scaling study of section 3.3, the distributions are shown in fig. 3.5, with β ranging from 2.8 (left) to 3.76 (right). As we can see, even for the strongest coupling there is still a clear separation of the eigenmodes from the origin.

For phenomenological applications it is of course most relevant to know how this spectral gap evolves when lowering the masses of two of the three flavors. Instead of monitoring the lowest eigenvalue of $\gamma_5 D_{\mathrm{r}}$, we can also use the closely related quantity $1/n_{\mathrm{CG}}$, where n_{CG} is the iteration count for the lightest pseudo-fermion in the action for the $N_f = 2+1$ runs (see section 3.4). In Fig. 3.6, such a histogram of $1/n_{\mathrm{CG}}$ for the lightest production run is shown. A clear gap can be seen, which provides strong evidence for the stability of the algorithm.[3]

[3] Also the acceptance rate and the Hamiltonian violation ΔH were monitored throughout the runs and there was no sign of any algorithmic problems.

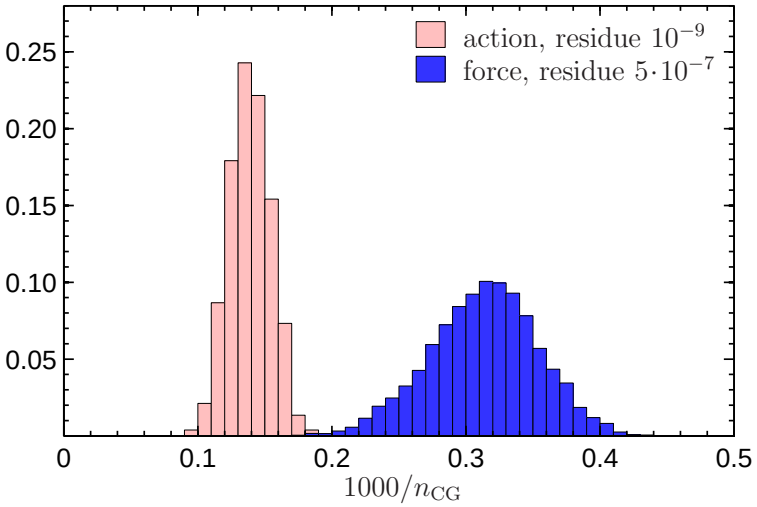

Figure 3.6: Histogram of the inverse iteration number of the linear solver. Results are from $48^3 \times 64$ lattice at $M_\pi \sim 190$ MeV, taken from the $N_f = 2+1$ ensemble at $\beta = 3.57$ (see tab. 3.3).

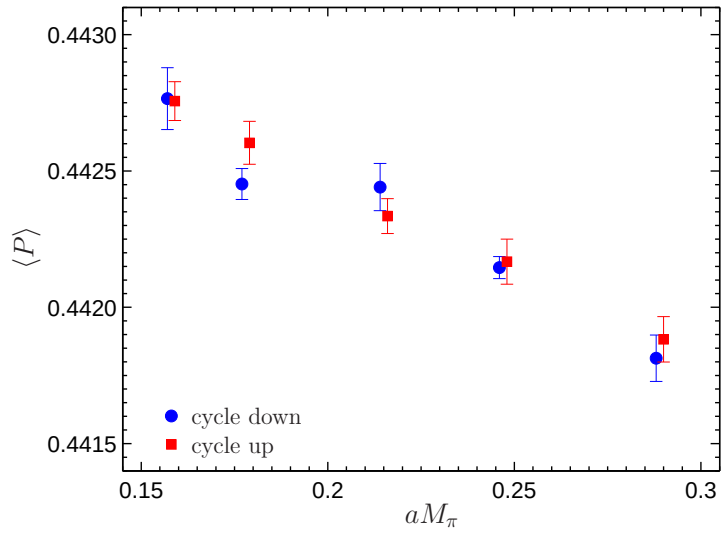

Figure 3.7: Absence of hysteresis in the average expectation value of the plaquette. Data are from an $N_f = 2+1$ run on a $16^3 \times 32$ lattice at $\beta = 3.3$ with a fixed strange quark mass corresponding to the PCAC mass of $am_s \simeq 0.0677$. The light quark mass was varied so that the corresponding PCAC quark mass changed between $am_{ud} \simeq 0.0066$ and 0.0243 in ascending (square) and descending (circles) order. The range of light quark masses corresponds to $M_\pi \sim 240 - 440$ MeV. Data points are slightly offset along the x-axis for better readability.

3.2.2 Search for potentially metastable behavior

In dynamical Wilson fermion simulations with small quark masses, it was reported that the system appears to undergo a first-order transition to an unphysical phase [106, 107]. This was argued to mean that there is a lower bound on the quark mass, below which physically sensible simulations cannot be performed. Moreover, it was observed, that

1. the phenomenon occurs only on coarse lattices,
2. gauge action improvement decreases the lower bound on the quark mass [108],
3. $O(a)$-improved Wilson fermions together with improved gauge actions made the problem disappear for all lattice spacings investigated in [106],
4. one level of stout smearing weakens the phenomenon [109].

When discussing such phenomena, it is important to remember that a first-order phase transition can only occur in infinite volume. In finite volume, the metastability can be understood as an artifact of the updating algorithm: with an efficient algorithm, the system should eventually find the true minimum of the effective potential. Thus, for finite-volume simulations, the relevant question is: can the algorithm thermalize the system in a manageable number of updating steps?

To investigate this issue, two $16^3 \times 32$ configurations were taken, one with random links and the other, thermalized in a $N_f = 2+1$ simulation at $\beta = 3.3$, with $am_{u,d}^{\mathrm{PCAC}} = 0.0066$, corresponding to a pion mass of approximately 240 MeV, and $am_s^{\mathrm{PCAC}} \simeq 0.0677$, corresponding roughly to the physical strange quark mass. A "downward" updating sequence was then constructed from the random configuration: consecutive simulations at $am_{u,d}^{\mathrm{PCAC}} \simeq 0.0243, 0.0173, 0.0131, 0.0086, 0.0066$, corresponding to a range of pseudo-scalar masses $M_\pi \sim 440 - 240$ MeV, were performed, with each simulation starting from the last configuration of the previous (larger mass) run. Similarly, an "upward" sequence of five simulations was obtained, beginning with the configuration thermalized at $am_{u,d}^{\mathrm{PCAC}} \simeq 0.0066$, and ending with a run at $am_{u,d}^{\mathrm{PCAC}} \simeq 0.0243$. For each point in the two sequences, approximately 400 trajectories were generated, of which the first 100 were discarded when calculating the average expectation value of the plaquette. The resulting plaquette values, obtained during the two updating sequences, are shown in Fig. 3.7. No sign of hysteresis is observed: the algorithm evolves the system to the correct equilibrium state in a reasonable number of steps, independently of the starting configuration.

This absence of evidence for metastability, together with the good performance of the algorithm in all of the production runs, indicates that this choice of algorithm and of action is appropriate for the range of parameters considered here.

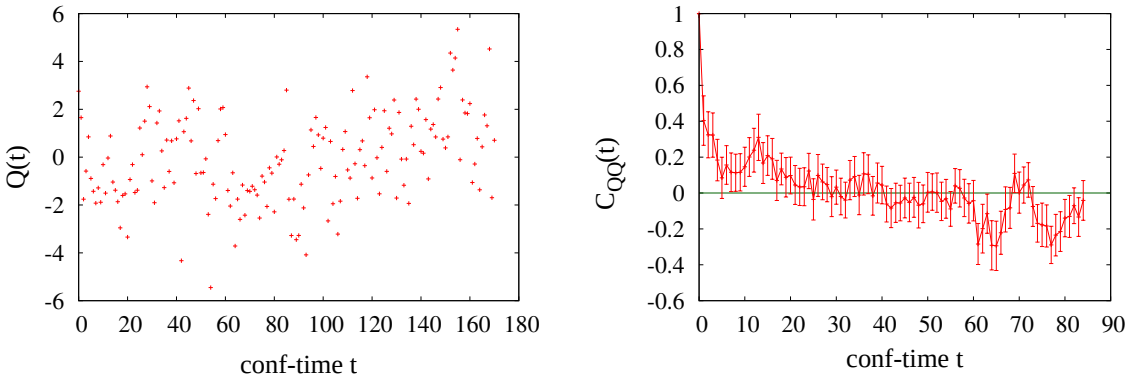

Figure 3.8: History of the unrenormalized gluonic topological charge (left) and the corresponding autocorrelation function plot (right), measured on the finest lattice with the smallest quark mass: $\beta = 3.76, aM_\pi = 0.2019(20)$. The integrated autocorrelation time of Q_{top} is approximately 2 configurations on this ensemble. A separation of one configuration corresponds to 10 HMC/RHMC trajectories.

3.2.3 Topology

In the previous chapter, we have discussed algorithms for dynamical overlap fermions, designed to enable the sampling of all topological sectors. This is necessary to ensure that the simulation is able to sample the whole phase space. Should it get stuck in one topological sector, it would be unclear if ergodicity is fulfilled. For Wilson type fermions this problem is less pronounced, since, at finite lattice spacing, there is no discontinuity in the action at the boundaries between the different sectors.

In the continuum however, it is not possible at all to change from one topological sector to another by a continuous sequence of gauge fields [110]. Thus, as the lattice spacing is reduced, the autocorrelation time of the topological charge will increase. It therefore must be demonstrated, that the combined choice of action and algorithm allows for an adequate sampling of the different sectors in the range of lattice spacings considered.

To determine the topological charge of the configurations, the naïve gluonic definition of the charge was used,

$$Q_{\text{top}} = \frac{1}{16\pi^2} \sum_x \text{Tr}\left[F_{\mu\nu}(x)\tilde{F}^{\mu\nu}(x)\right], \tag{3.5}$$

where $F_{\mu\nu}$ is the gluonic field strength tensor, constructed from the smeared links of eqn. (3.2), and the sum extends over all lattice sites. Since the charge defined in eqn. (3.5) does not necessarily have an integer value, it must in principle be renormalized for quantitative studies of topology. However, such a renormalization is not necessary here, since

we are only interested in verifying the topological ergodicity of the simulations.

The simulation-time evolution and autocorrelation of this unrenormalized topological charge are shown in fig. 3.8 for the finest lattice spacing and at the smallest quark mass ($aM_\pi = 0.2019(20)$) available there. This therefore provides a worst case scenario for the parameter range considered.

No dramatic slowing down of tunneling events can be observed. The integrated autocorrelation time is found to be around 2 configurations, with the autocorrelation decaying very rapidly and being compatible with zero within errors after around 5 configurations. We can conclude from these two plots that there is no long-range correlation.

3.3 Scaling study

To analyze the scaling properties of the Symanzik improved gauge and stout link Clover fermion action, simulations with lattices of approximately constant physical volume at five different lattice spacings are used. The study includes $N_f = 3$ quark flavors instead of a simple $N_f = 2$ setting in order to also test the full RHMC algorithm. The temporal extent is set to $T = 2L$ with lattice sizes varying from $L/a = 8$ to $L/a = 24$ and bare gauge couplings between $\beta = 2.8$ and $\beta = 3.76$. Fermionic observables are measured every twenty trajectories for $L/a = 8, 10, 12$ and every ten for $L/a = 16, 24$. For the error analysis, the "moving-block-bootstrap" [111] technique was used, with a bin size of two times the integrated autocorrelation time of the quantity which is measured. This bin size is typically around 2 for the coarsest lattices and around 8 for the finest lattices. The number of bootstrap samples is chosen to be 2000, because the calculated bootstrap errors saturate at $\simeq 1500$ samples.

At each lattice spacing, configurations with a number of different quark masses are generated (from seven at $L/a = 8$ to three at $L/a = 24$) such that M_π/M_ρ is between 0.60 and 0.68. It is preferable to use these rather large masses for a scaling study in order to enhance possible discretization effects of order Ma. After fixing to Coulomb gauge, propagators with multiple Gaussian sources are measured on different time slices. The source size is set to $L/4$ and is thus roughly constant in physical units. Using a Gaussian sink of the same size, the effective masses usually reach a plateau very quickly and a suitable fitting window could be found in every case. To illustrate this point, a typical effective mass plot is shown in fig. 3.9.

Then, the masses are extracted from a correlated single channel cosh or sinh fit to the correlators. In order to estimate the systematic error due to excited states, the analysis is

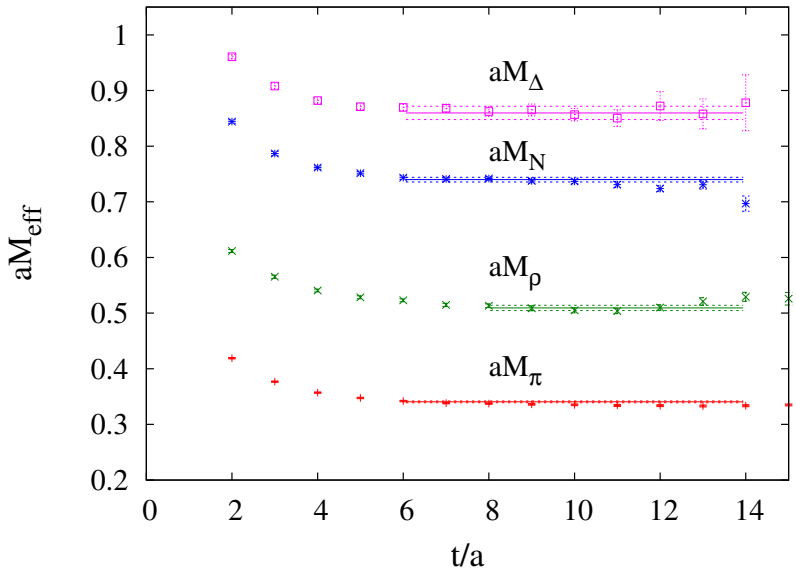

Figure 3.9: Effective masses of the pion, rho, nucleon and delta on the ensemble with $L/a = 16$, $\beta = 3.59$, $am_{\mathrm{PCAC}} = 0.04608(12)$. The horizontal lines are the masses with error bars obtained from correlated cosh or sinh fits in the time intervals indicated by the length of the lines.

repeated with a reduced fit range (by up to 2 timeslices) and the difference then propagated into the systematic error in the continuum limit.

For each coupling β the masses $a^2M_\pi^2$, aM_ρ, aM_{N} and aM_Δ are interpolated linearly to a common current quark mass as determined by M_π/M_ρ. For illustration the interpolation at $\beta = 3.59$ is shown in fig. 3.10. The error on the current quark mass is of order 10^{-4} and therefore barely visible on this scale. Note that all data points are fully unquenched.

The scaling test on the baryon spectrum is performed for three different values of M_π/M_ρ, all of which can be reached by interpolating the simulation data. In tab. 3.1 the values of am_{PCAC}, aM_π, aM_ρ, aM_{N} and aM_Δ after interpolation to $M_\pi/M_\rho = 0.60, 0.64, 0.68$ are summarized. Also listed is LM_π, which is roughly constant for fixed M_π/M_ρ. Moreover, even for the lightest data set we are deep in the $M_\pi L > 4$ regime. The finite size analysis performed for the spectrum calculation (see section 3.4.2) shows that for the lattices of tab. 3.1 any finite size effects are significantly smaller than 1%. Additionally, the lattices have a fixed physical size which ensures that such effects would be the same for all data at a given M_π/M_ρ ratio.

The masses have errors smaller than 2% and, due to correlations, this is also true for mass ratios. For the three lines of constant physics, M_{N} and M_Δ in units of M_π are plotted in

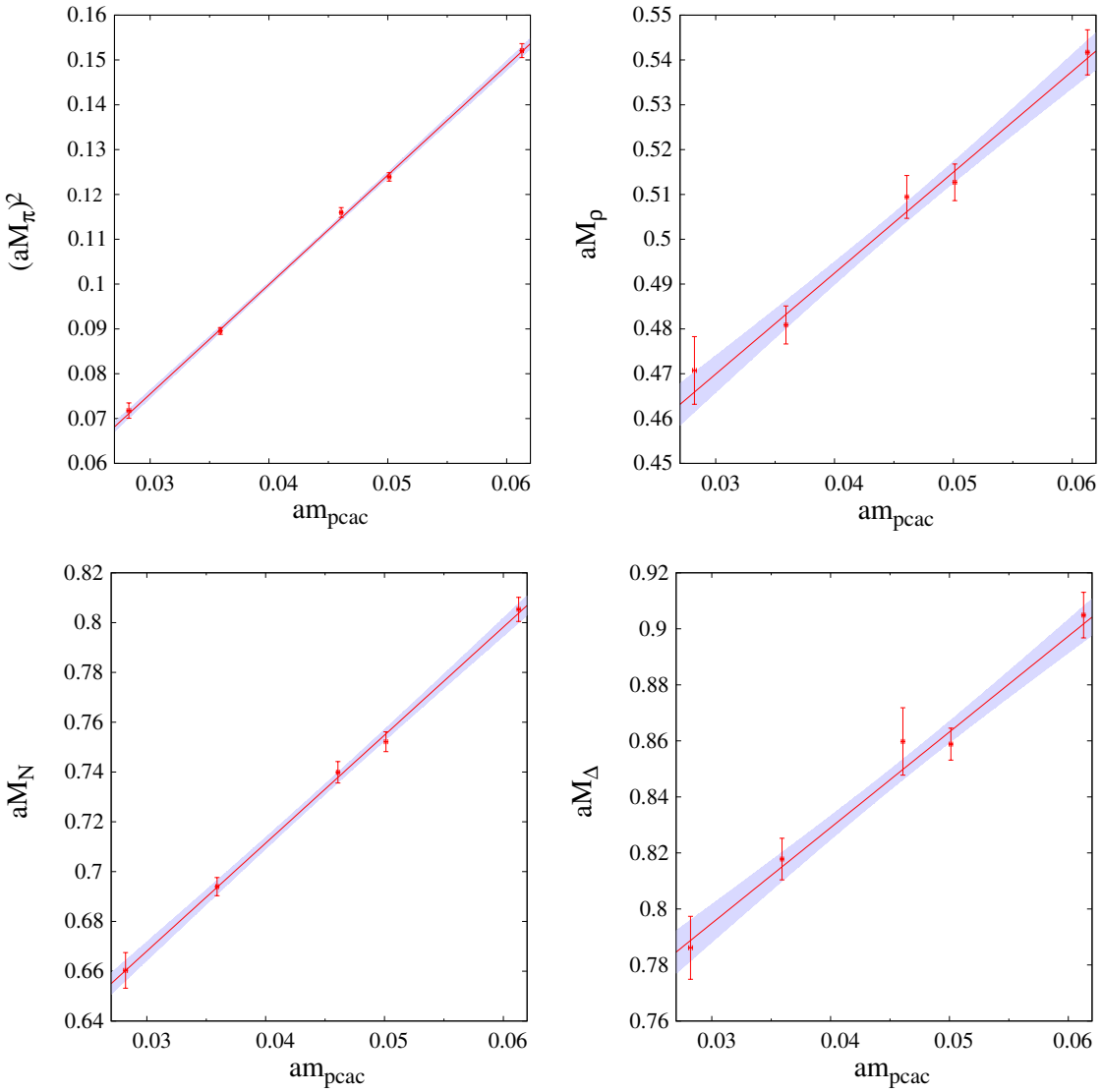

Figure 3.10: Linear fits of the spectrum in terms of the PCAC quark mass. Data shown are from $\beta = 3.59$, $L/a = 16$ simulations. The line indicates the central value of the interpolation and the shaded region is the corresponding 1σ error band (based on the assumption that the linear ansatz is correct).

$\frac{M_\pi}{M_\rho}$	$\frac{L}{a}$	β	am_{PCAC}	LM_π	aM_π	aM_ρ	aM_{N}	aM_Δ
	8	2.80	0.0676(11)	4.55	0.5688(26)	0.9480(44)	1.3605(73)	1.5944(75)
	10	3.23	0.0468(28)	4.44	0.4437(57)	0.7395(95)	1.064(12)	1.248(10)
0.60	12	3.40	0.0437(15)	4.60	0.3830(34)	0.6384(57)	0.9236(74)	1.0823(87)
	16	3.59	0.0328(6)	4.56	0.2852(26)	0.4754(43)	0.6785(44)	0.8031(38)
	24	3.76	0.0217(7)	4.85	0.2019(20)	0.3365(33)	0.4825(34)	0.5708(20)
	8	2.80	0.0839(8)	5.03	0.6292(21)	0.9832(33)	1.4341(43)	1.6581(59)
	10	3.23	0.0607(23)	4.95	0.4950(47)	0.7735(73)	1.127(10)	1.3074(82)
0.64	12	3.40	0.0545(13)	5.12	0.4268(23)	0.6669(35)	0.9711(62)	1.1282(71)
	16	3.59	0.0405(6)	5.03	0.3146(23)	0.4916(36)	0.7099(35)	0.8278(28)
	24	3.76	0.0270(6)	5.41	0.2256(18)	0.3524(28)	0.5081(29)	0.5933(29)
	8	2.80	0.1050(11)	5.60	0.6993(22)	1.0284(32)	1.5286(52)	1.7401(65)
	10	3.23	0.0796(21)	5.57	0.5574(52)	0.8198(76)	1.212(11)	1.389(10)
0.68	12	3.40	0.0693(12)	5.76	0.4798(30)	0.7055(44)	1.0354(47)	1.1903(52)
	16	3.59	0.0506(7)	5.57	0.3483(22)	0.5122(32)	0.7495(30)	0.8590(41)
	24	3.76	0.0343(9)	6.11	0.2546(25)	0.3744(37)	0.5434(38)	0.6242(39)

Table 3.1: Results of the interpolation of aM_π, aM_ρ, aM_N and aM_Δ, obtained from simulations performed at different bare quark masses and gauge couplings, to the reference points $M_\pi/M_\rho = 0.60, 0.64, 0.68$.

fig. 3.11 as functions of the squared lattice spacing (see below), measured in units of the vector meson mass. The baryon masses are normalized by M_π to clearly separate the lines of constant physics in the plot. The fits incorporate the error bars along both the vertical and horizontal axes.

For both the spin-$1/2$ and spin-$3/2$ baryons, the continuum limit is approached smoothly with scaling violations of at most 1.2% at $\beta = 2.8$. The extrapolations shown exclude this data point but consistent results are obtained by using all available data.

While we can expect that the choice of the clover coefficient is close to a non-perturbtively determined value, effects that are linear in the lattice spacing cannot be excluded in principle. The cutoff effects of this action are so small that it is not possible to make a definitive statement, despite the fact that the data is very precise and covers more than a factor of seven in a^2. Assuming the lattice artifacts to be linear in a produces an only marginally worse fit.

An alternative way of proceeding is doing a combined chiral and continuum extrapolation with all data points at once. Applying this procedure one obtains basically consistent continuum limits. Again, the absolute differences goes into the systematic error.

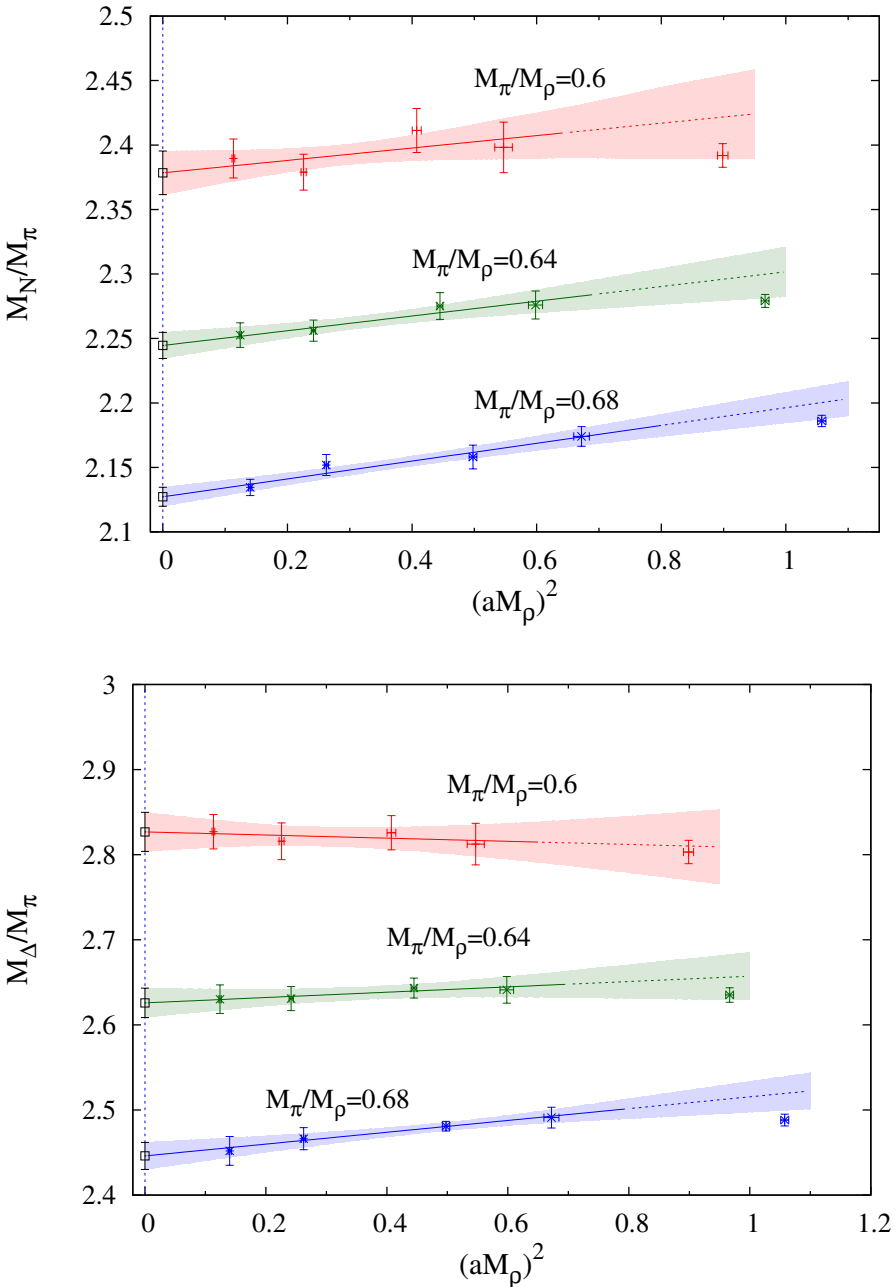

Figure 3.11: $M_{\rm N}$ and M_Δ, the mass of the spin-1/2 and spin-3/2 baryon, in terms of M_π, versus the lattice spacing squared (in terms of M_ρ^{-1}). Each one of the three continuum extrapolations is based on the data at $\beta = 3.76 - 3.23$, but the curve is extended to $\beta = 2.8$ (the points on the right) to allow for comparison. The continuum limits are $M_N/M_\pi = 2.378(17)(43), 2.245(10)(51), 2.127(7)(34)$ and $M_\Delta/M_\pi = 2.827(23)(40), 2.626(17)(49), 2.446(16)(30)$ respectively. For all data-points only statistical errors are shown.

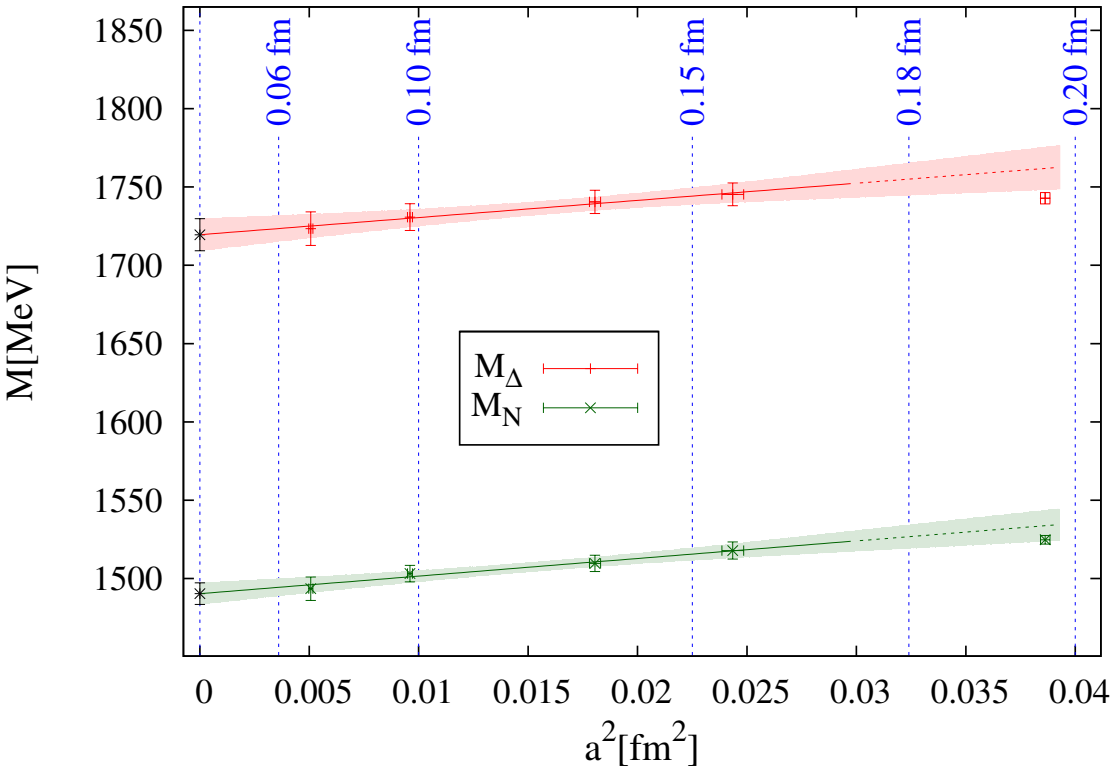

Figure 3.12: Scaling of the Δ and nucleon mass at $M_\pi/M_\rho = 0.67$ in physical units using the scale setting procedure described around (3.6). In the continuum one obtains $M_{\rm N} = 1490(7)(27)$ MeV and $M_\Delta = 1720(10)(35)$ MeV. As in fig. 3.11, only statistical errors are shown.

For illustrative purposes, one can set the scale by linearly interpolating M_ρ and M_π^2 to the point where

$$M_\pi/M_\rho = \sqrt{2(M_K^{\rm phys})^2 - (M_\pi^{\rm phys})^2}/M_\phi^{\rm phys} \sim 0.67 \tag{3.6}$$

and identify M_ρ with the mass of the physical ϕ. According to this convention lattice spacings from 0.19 fm down to 0.07 fm (see fig. 3.12) are covered. In this range only small scaling violations can be found in the spectrum and these disappear smoothly toward the continuum. The behavior is consistent with that of an O(a)-improved theory.

3.4 Light hadron masses

In the previous two sections we have seen that the the Symanzik improved gauge and stout link Clover fermion action possesses excellent scaling properties and that the combination of action and simulation algorithm is both highly efficient and algorithmically safe. In this section this setup will be applied to a dynamical $N_f = 2+1$ calculation of the light hadron spectrum with fully controlled systematic errors. We will see that the results agree with the experimental data with combined errors in the low $O(1)$ per-cent range. They therefore provide further strong evidence that QCD is the correct theory of the strong interaction.

3.4.1 Strategy

For a LQCD calculation of light hadron masses with fully controlled systematic errors, a number of requirements needs to be fulfilled:

1. The inclusion of the up (u), down (d) and strange (s) quarks in the fermion determinant with an exact algorithm and with an action whose universality class must be QCD. For the light hadron spectrum, the effects of the heavier charm, bottom and top quarks are included in the coupling constant and light quark masses. With the action and the algorithms described in the previous section this requirement is clearly satisfied.
2. A complete determination of the masses of the light ground-state, flavor non-singlet mesons and octet and decuplet baryons. Three of these are used to fix the masses of the isospin averaged light (m_{ud}) and strange (m_s) quark masses and the overall scale in physical units.
3. Large volumes to guarantee small *finite-size effects* and at least one data point at a significantly larger volume to confirm the smallness of these effects. In large volumes, finite-size corrections to the spectrum are exponentially small [112, 113]. As a conservative rule of thumb $M_\pi L \gtrsim 4$, with M_π the pion mass and L the lattice size, guarantees that finite-volume errors in the spectrum are around or below the percent level (see section 3.4.2 below). Resonances require special care. Their finite volume behavior is more involved. The literature provides a conceptually satisfactory framework for these effects [114, 115] which should be included in the analysis.
4. Controlled *interpolations and extrapolations* of the results *to physical quark masses* (m_{ud} and m_s, or eventually directly simulating at these mass values). Although interpolations to physical m_s, corresponding to $M_K \simeq 495$ MeV, are straightforward, the

extrapolations to the physical value of m_{ud}, corresponding to $M_\pi \simeq 135$ MeV, are difficult. They need computationally intensive calculations with M_π reaching down to 200 MeV or less.

5. Controlled extrapolations to the *continuum limit*, requiring that the calculations be performed at no less than three values of the lattice spacing, in order to guarantee that the scaling region is reached.

The spectrum calculation discussed here includes a large range of light hadron masses, 14 in total, certainly enough to fulfill the requirements of point 2. In principle, any of these masses could be used to set the overall physical scale. However, the selected particle mass should be a quantity which can be calculated precisely and whose experimental value is well known. Additionally, it should have a weak dependence on m_{ud} to not strongly alter the chiral behavior of other observables. Finally, the particle should not decay under the strong interaction.

On the one hand, the larger the strange content of the particle, the more precise the mass determination and the weaker the dependence on m_{ud}. These facts support the use of the Ω baryon, the particle with the highest strange content. On the other hand, the determination of baryon decuplet masses is usually less precise than those of the octet. This observation would suggest that the Ξ baryon is appropriate. Because both the Ω and Ξ are reasonable choices, two analyses are carried out, one with M_Ω (Ω set) and one with M_Ξ (Ξ set). For all three gauge couplings, β=3.3, 3.57 and 3.7, both quantities give consistent results, namely: $a \approx 0.125$, 0.085 and 0.065 fm, respectively.

More work is needed to meet the remaining three requirements and we will discuss how this is done in the following sections.

3.4.2 Finite-size effects

In general, the energy of the different hadronic states depends on the (physical) spatial volume of the lattice. In the simulations we are discussing here, the size of the lattice for each ensemble was chosen so that the spatial extension L would always fulfill the condition $M_\pi L \gtrsim 4$. For stable particles like the pion or nucleon, as will become clear in a moment, this is indeed enough to ensure that finite-size corrections are small, typically below the 1% threshold. For resonant states like the delta or the rho additional work is needed. We will discuss this issue below.

There are the two sources of volume dependence which we will refer to as type I (all particle states) and type II (resonant states). The literature provides a conceptually satisfactory

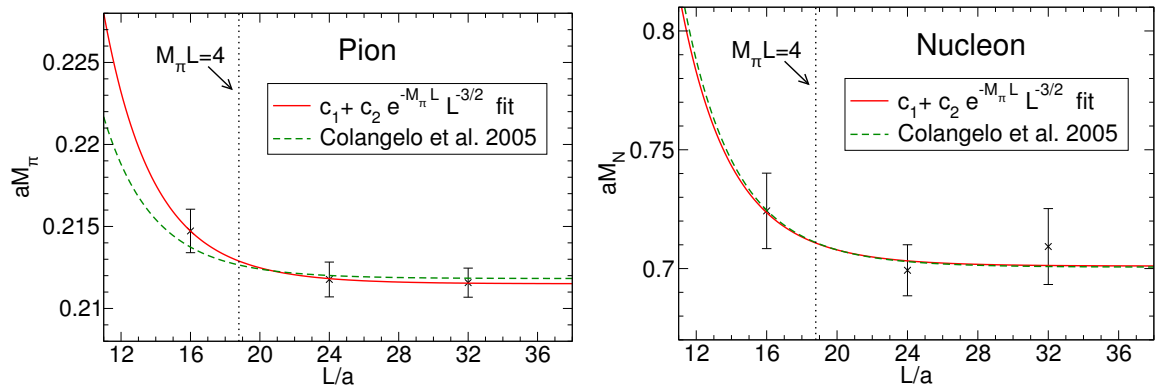

Figure 3.13: Volume dependence of the π (left panel) and N (right panel) masses in one of the simulation points at $a \approx 0.125$ fm and $M_\pi \approx 320$ MeV. The fit of the form $c_1 + c_2 \exp(-M_\pi L)/(M_\pi L)^{3/2}$ is shown by the solid lines, with $c_1 = aM_X(L = \infty)$ and $c_2 = ac_X(M_\pi)$ given in the text ($X = \pi, N$ for pion/nucleon). Fits with c_2 of refs. [116, 117] are shown by the dashed lines.

framework for a treatment of these effects [112–115].

Type I finite-size corrections

All particle masses are shifted by finite volume effects due to pion exchanges between the different copies of the periodic system. The induced corrections in the spectrum fall off exponentially with $M_\pi L$ for large enough volumes [112]. For one set of parameters ($M_\pi \approx 320$ MeV at $a \approx 0.125$ fm), additional runs have been carried out for several spatial volumes ranging from $M_\pi L \approx 3.5$ to 7. The size dependences of the different hadron masses M_X are successfully described by $M_X(L) = M_X + c_X(M_\pi) \cdot \exp(-M_\pi L)/(M_\pi L)^{3/2}$. Figure 3.13 shows the volume dependence at M_π = 320 MeV for the two statistically most significant channels: pion and nucleon. The fitted c_X coefficients are in good agreement with those suggested by [116, 117] which predicts a behaviour of $c_X(M_\pi) \propto M_\pi^2$. According to these results the rule of thumb ($M_\pi L \gtrsim 4$ gives the infinite volume masses within statistical accuracy) is confirmed for all channels. Still, these finite volume corrections are included in the analysis.

Type II finite-size corrections

In regions of parameter space, where a resonant state would decay in infinite volume, its finite volume mass is shifted due to an avoided level crossing phenomenon. In this case the lowest energy state with the quantum numbers of the resonance in infinite volume is a

two particle scattering state. Its effects therefore have to be included in the analysis[4]. For the rho meson[5] in a finite box of size L, the spectrum in the center of mass frame consists of two pion states with total energy $2\sqrt{M_\pi^2+\mathbf{k}^2}$, where $\mathbf{k}=\mathbf{n}2\pi/L$, $\mathbf{n}\in Z^3$, the pion mass M_π with the type I corrections of the previous paragraph, and the rho resonance state with mass M_ρ, again with corrections of type I. The basic result of [114] is that the true energy spectrum is still given by above expression but with k being a solution of a complicated non-linear equation. Solving this equation leads to energy levels for different volumes and masses.

For a resonant state "X" the spectrum is therefore determined by the spatial lattice size L, the infinite volume masses of the resonance M_X and the decay products, say M_1 and M_2, and one parameter, g_X, which describes the effective coupling of the resonance to the decay products and is thus directly related to the width of the resonance. In an *ab initio* calculation of the spectrum however, one cannot rely on experimental inputs in the calculations of the hadron masses. Therefore both M_X and g_X are determined from the set of measurements for various L, M_1 and M_2. With the quark masses and volumes used within this calculation, it turns out that the masses of the resonant states can be accurately extracted by this procedure (with two exceptions, see below). The sensitivity to the resonances' widths is however limited but the results are in agreement with the experimental values, albeit with large errors.

In two cases out of 14·12=168 mass determinations (14 sets of lattice parameters/volumes, see tab. 3.3, and 12 hadrons), the finite volume "scattering" state has a lower energy than the corresponding resonance. These exceptions are the ρ and Δ for the lightest pion mass point at $a\approx 0.085$ fm. For a reliable extraction of the resonance mass precise information on the resonance's width would be required. Thus, these two mass points have to be left out of the analysis (only these two, and only for one ensemble).

3.4.3 Interpolations and extrapolations to physical quark masses

The simulations are performed at physical strange quark mass, or at two values of m_s and otherwise fixed parameters and then interpolated to physical m_s. Because simulations at small m_{ud} quark mass is computationally very costly, the ensembles are generated using larger than physical[6] quark masses and the results therefore have to be extrapolated to the

[4] For a detailed description of the phenomenon see [4]

[5] This analysis can be extended to other resonant states [4, 115].

[6] As *e.g.* defined by the pion mass.

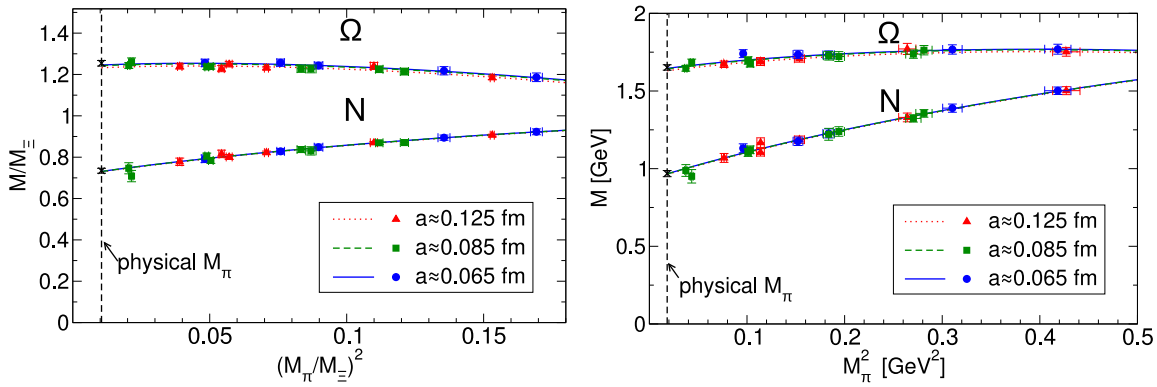

Figure 3.14: Pion mass dependence of the N and Ω for all three values of the lattice spacing, using mass ratios normalized by M_Ξ (left panel), evaluated at the corresponding simulation points, or masses in physical units (right panel). In this case the scale is set by M_Ξ at the physical point. The χ^2/d.o.f values of (left panel) are 9.46/14 and 7.10/14; whereas those of (right panel) are 10.6/14 and 9.33/14, for the Ω and the nucleon, respectively. All data points represent mean $\pm$ SEM.

physical point.

In order to give a reliable estimate of the systematic effects associated with these extrapolations, two different extrapolation schemes are used and three different cuts on the maximum pion mass are applied. The resulting differences are accounted for in the systematic uncertainties. This analysis is carried out both for the Ξ and for the Ω sets separately.

Let us call the two methods to normalize the hadron masses "the ratio method", and "mass independent scale setting".

The ratio method. This method is motivated by the fact that in QCD one can calculate only dimensionless combinations of observables, *e.g.* mass ratios. Furthermore, in such ratios cancellations of statistitical uncertainties and systematic effects may occur. The method uses the ratios r_X=M_X/M_Ξ and parametrizes the mass dependence of these ratios in terms of r_π=M_π/M_Ξ and r_K=M_K/M_Ξ. The continuum extrapolated two-dimensional surface r_X= $r_X(r_\pi,r_K)$ is an unambiguous prediction of QCD for a particle of type X (a couple of points of this surface have been determined in the scaling study of the previous section). One-dimensional slices ($2r_K^2 - r_\pi^2$ was set to 0.27, its physical value) of the two-dimensional surfaces for N and Ω (Ξ set) are shown in fig. 3.14. The displayed data points are obtained by interpolating the lattice results to the physical m_s (defined by setting $2M_K^2$-M_π^2 to its physical value). The curves are the corresponding fits. The crosses are the continuum extrapolated values in the physical pion mass limit. The lattice-spacing dependence of the

results is barely significant statistically despite the factor of 3.7 separating the squares of the largest ($a\approx$0.125 fm) and smallest ($a\approx$0.065 fm) lattice spacings.

The extrapolation of a particle mass "M_X" to the physical pion mass is based on an expansion of M_X (or r_X) in terms of the pion and kaon mass contributions around some mass point. This point can either be r_π=0 (M_π=0), which corresponds to chiral perturbation theory, or alternatively one can use the center of the r_π^2 (or M_π) region of the simulation points. Both strategies will be used in the following (and referred to as "chiral fit" and "Taylor fit", respectively).

As it turns out, a linear term in r_K^2 (or M_K^2) is sufficient for the required small interpolations. Except for the mesons, this is, however, not true for the expansions in the pion mass. Here, in addition to a linear expression in M_π^2, chiral perturbation theory suggests [118] an M_π^3 next-to-leading order behavior for masses other than those of the pseudo-Goldstone bosons. A generic expansion of the ratio r_X around a reference point reads: $r_X = r_X(ref) + \alpha_X[r_\pi^2 - r_\pi^2(ref)] + \beta_X[r_K^2 - r_K^2(ref)] + hoc$ resulting in higher order contributions (*hoc*). In the chiral fit a *hoc* of the form r_π^3 (following chiral perturbation theory) is used, leaving all coefficients free and taking the reference point at $r_\pi^2(ref)$=0 and $r_K^2(ref)$ at the center of the fit range.

The second strategy is a Taylor expansion in r_π^2 and r_K^2 around a reference point which does not correspond to any sort of singularity ("Taylor fit"). The reference point $(r_\pi^2(ref), r_K^2(ref))$ in this case is chosen to be the center of the fit range. This choice guarantees that all points are well within the radius of convergence, since the nearest singularities are at $M_\pi = 0$ and/or $M_K = 0$. The higher order contribution *hoc* of the form r_π^4 turns out to be sufficient.

The extrapolation is then done using both the chiral and the Taylor fit method and the difference between the two is included in the systematic error.

In case of the vector mesons, the higher order contributions turn out to have coefficients which are compatible with zero even when the full pion mass range is used (still these terms are included). This is however not true for the baryons. To get a handle on possible higher order contributions three different pion fit ranges are considered. These correspond to the full 14 simulation points, all points up to $r_\pi = 0.38$ and finally those points below $r_\pi = 0.31$. The differences between results obtained using these three pion mass ranges are included in the systematic error analysis.

Mass independent scale setting. This is the more conventional method. It consists of setting the lattice spacing by extrapolating M_Ξ to the physical point, given by the physical

ratios of M_π/M_Ξ and M_K/M_Ξ. Using the resulting lattice spacings obtained for each bare gauge coupling, M_X vs. M_π and M_K are extrapolated applying both strategies ("chiral" and "Taylor") discussed above. This is repeated for the three different pion mass ranges defined in the previous paragraph[7].

3.4.4 Continuum limit

As can be clearly seen from fig. 3.14, scaling violations are small (typically below the 1% level). As a consequence, although with this action, in principle $O(\alpha_s\, a)$ scaling violations could be present, the data is just as well described by assuming that these are absent and the dominant contributions are of $O(a^2)$, as it would be the case for a $O(a)$ improved formulation. These effects are taken into account in a combined fit by allowing $r_X(ref)$ (or $M_X(ref)$) of the previous paragraph to acquire a linear dependence in a or in a^2. The difference between them again enters into the systematic error.

3.4.5 Data analysis

Systematic uncertainties are studied by the different methods discussed above and by using 18 possible time intervals in the fits of two point functions used to extract the hadron masses.

Since the light hadron spectrum is known experimentally it is of extreme importance to carry out a blind data analysis. One should avoid any arbitrariness related *e.g.* to the choice of some fitting intervals or pre-specified coefficients of the chiral fit. To that end, the analysis follows an extended frequentist's method [119]: several possible sets of fitting procedures are combined (without imposing any additional information for the fits) and weighted according to their fit quality. Thus, there are 2 normalization methods, 2 strategies to extrapolate to the physical pion mass, 3 pion mass ranges, 2 different continuum extrapolations and 18 time intervals for the fits of two point functions, which result in 2·2·3·2·18=432 different results for the mass of each hadron. Note, that isospin breaking effects were included as corrections to the experimental data [120]. Higher order corrections to these masses [121], as well as electromagnetic effects [121], which are neglected here, are expected to be well below the 1% level.

[7] Using the lattice spacing obtained this way, the cuts correspond to: all data points, a cut at M_π=560 MeV and at M_π=450 MeV, respectively.

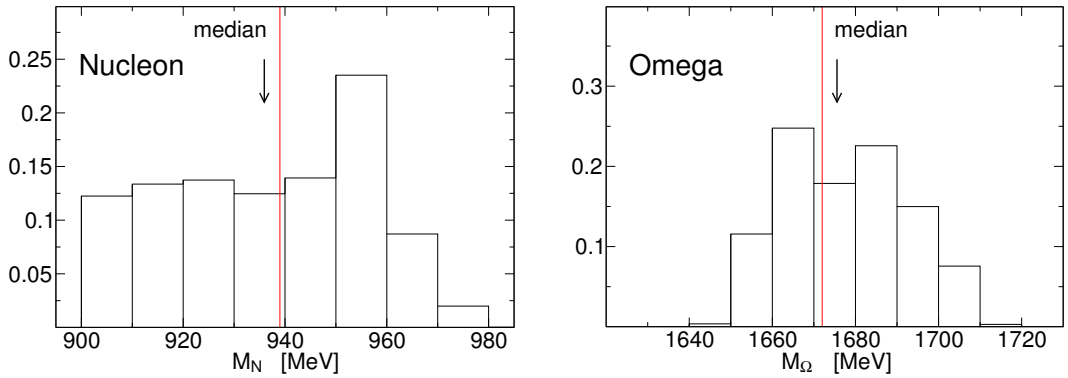

Figure 3.15: Distribution of the N and the Ω mass. The distribution was obtained from 432 different fitting procedures as explained in the text. The median is shown by the arrow. The experimental value of the nucleon mass is indicated by the vertical line.

In order to determine the statistical uncertainties a bootstrap analysis with 2000 samples for each of the 432 fitting procedures is performed. For each bootstrap sample a distribution of the 432 results weighted by their fit qualities is constructed. This weighted distribution for the full sample is shown on fig. 3.15. The best fit for the mass is given by the median of the distribution obtained from the full sample; the systematic error is estimated by the central 68% of the distribution. Finally, the medians of the distributions from the bootstrap samples give the statistical error (SEM). A breakdown of the total systematic errors into individual components is given in tab. 3.2. Systematic and statistical errors were added in quadrature, yielding the final errorbars.

3.4.6 Simulation Points

The simulation points are listed in tab. 3.3. The autocorrelation times of the smeared plaquette, of the conjugate gradient iteration steps and of *e.g.* pion and nucleon correlators is less than 10 trajectories for all ensembles. Thus, every 10th trajectory enters the analysis and is treated as uncorrelated data point[8].

Gaussian sources and sinks are used, because these suffer less from contributions of excited states (see fig. 3.16). Depending on the size of the temporal extension of the lattice more than one source is used for the propagator calculations. Since propagators from a single configuration are clearly correlated, they are placed in one bootstrap bin in the final analysis.

[8] This was checked in the final analysis *e.g.* by blocking data points.

	finite volume	chiral fits/scale setting	continuum extraplation	excited states
ρ	0.20	0.55	0.20	0.45
K^*	0.20	0.30	0.40	0.65
N	0.05	0.90	0.15	0.25
Λ	0.10	0.60	0.55	0.40
Σ	0.05	0.85	0.15	0.25
Ξ	0.10	0.40	0.60	0.60
Δ	0.05	0.65	0.35	0.95
Σ^*	0.10	0.65	0.20	0.75
Ξ^*	0.30	0.75	0.35	0.75
Ω	0.05	0.55	0.45	0.60

Table 3.2: Error budget in fractions of the total systematic error. Results represent averages over the Ξ and Ω sets. The columns correspond to the uncertainties related to finite volume corrections, extrapolation to the physical pion mass (chiral/Taylor for each three possible pion mass intervals with ratio method or mass independent scale setting), continuum extrapolation ($O(a)$ or $O(a^2)$ behaviour) and the effect of excited state contaminations (different fit ranges in the mass extractions). The squared sum of the individual fractions do not exactly add up to 1. The small ($\lesssim$20%) differences are due to correlations and the non-Gaussian nature of the distributions.

β	am_{ud}	am_s	$L^3 \times T$	# traj.
3.3	-0.0960	-0.057	$16^3 \times 32$	10000
	-0.1100	-0.057	$16^3 \times 32$	1450
	-0.1200	-0.057	$16^3 \times 64$	4500
	-0.1233	-0.057	$16^3 \times 64$ / $24^3 \times 64$ / $32^3 \times 64$	5000 / 2000 / 1300
	-0.1265	-0.057	$24^3 \times 64$	2100
3.57	-0.0318	0.0 / -0.01	$24^3 \times 64$	1650 / 1650
	-0.0380	0.0 / -0.01	$24^3 \times 64$	1350 / 1550
	-0.0440	0.0 / -0.007	$32^3 \times 64$	1000 / 1000
	-0.0483	0.0 / -0.007	$48^3 \times 64$	500 / 1000
3.7	-0.0070	0.0	$32^3 \times 96$	1100
	-0.0130	0.0	$32^3 \times 96$	1450
	-0.0200	0.0	$32^3 \times 96$	2050
	-0.0220	0.0	$32^3 \times 96$	1350
	-0.0250	0.0	$40^3 \times 96$	1450

Table 3.3: Parameters, lattice sizes and statistics. The table summarizes the 14 simulation points at three different lattice spacings ordered by the light quark masses.

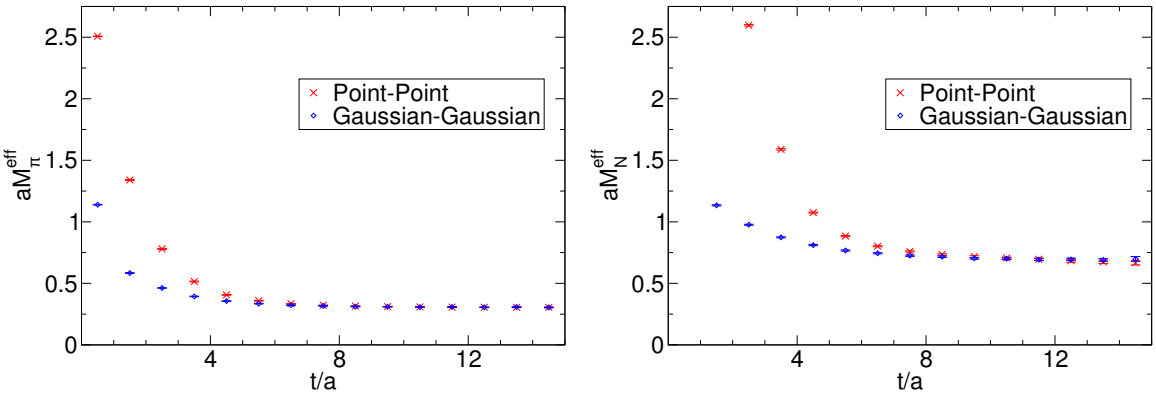

Figure 3.16: Effective masses for different source types in the pion (left panel) and nucleon (right panel) channels. Local sources have vanishing extents, whereas Gaussian sources, used on Coulomb gauge fixed configurations, have widths of ≈0.32 fm. As can be seen, the extended sources/sinks result in much smaller excited state contaminations.

X	Exp. [119]	M_X (Ξ set)	M_X (Ω set)
ρ	0.775	0.775(29)(13)	0.778(30)(33)
K^*	0.894	0.906(14)(4)	0.907(15)(8)
N	0.939	0.936(25)(22)	0.953(29)(19)
Λ	1.116	1.114(15)(5)	1.103(23)(10)
Σ	1.191	1.169(18)(15)	1.157(25)(15)
Ξ	1.318	1.318	1.317(16)(13)
Δ	1.232	1.248(97)(61)	1.234(82)(81)
Σ^*	1.385	1.427(46)(35)	1.404(38)(27)
Ξ^*	1.533	1.565(26)(15)	1.561(15)(15)
Ω	1.672	1.676(20)(15)	1.672

Table 3.4: Spectrum results in GeV. The statistical and systematic uncertainties on the last digits are given in the first and second set of parentheses, respectively.

3.4.7 Result

The results of the simulation are given in fig. 3.17 and tab. 3.4. In fig. 3.17 the Ξ set is depicted, the error bars give the systematic and statistical errors, summed in quadrature. Both the Ξ and the Ω set are shown in tab. 3.4 and systematic and statistical errors are given separately. Experimental masses given are isospin-averaged. For each of the isospin multiplets considered, this average is within at most 3.5 MeV of the masses of all of its members. Note that as expected, the octet masses are more accurate than the decuplet

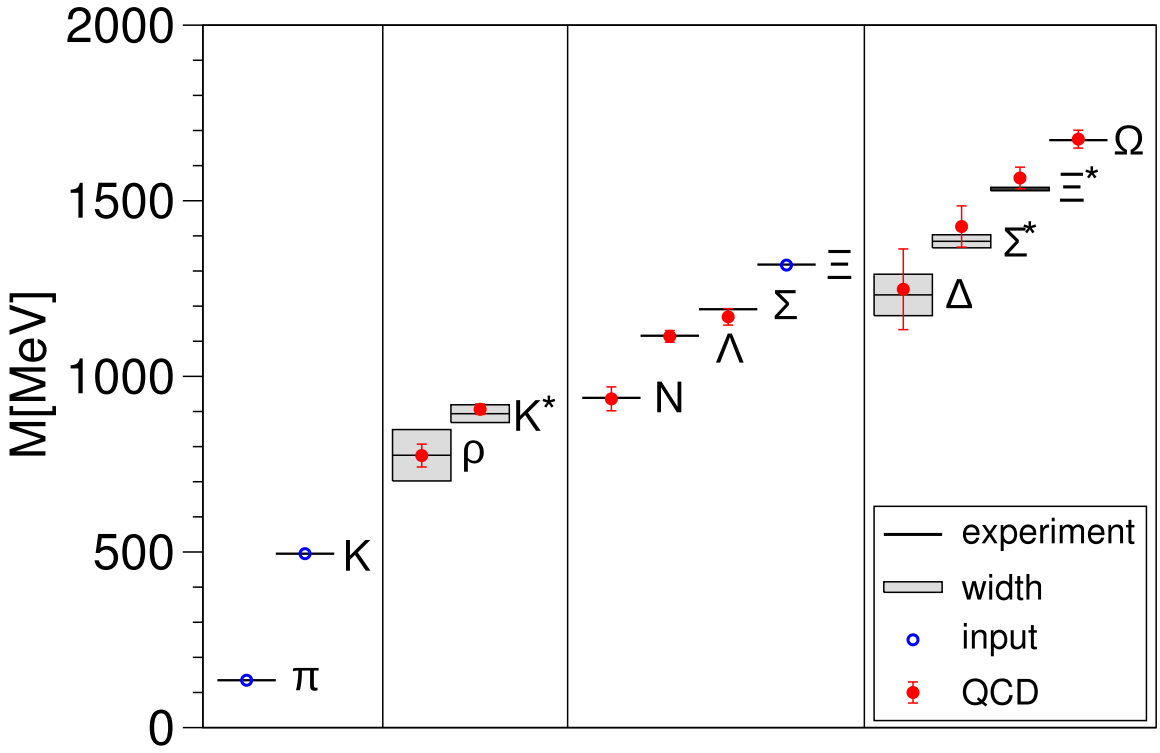

Figure 3.17: The light hadron mass spectrum of QCD. Horizontal lines and bands are the experimental values with their decay widths. The results are shown by solid circles. Vertical error bars represent our combined statistical and systematic error estimates. π, K and Ξ have no error bars, because they are used to set the light quark mass, the strange quark mass and the overall scale, respectively.

masses, and the larger the strange content the more precise is the result. Consequently, the Δ mass determination is the least precise.

As can be clearly seen, the calculated masses agree with the experimentally measured hadron spectrum. This calculation therefore strongly suggests that QCD correctly accounts for the magnitude of the hadron masses, and therefore, at low energies as well, is indeed the theory of the strong interaction.

3.5 Summary and outlook

In this section we have discussed a setup for simulations of Lattice QCD based on a tree-level Symanzik improved gauge action and stout-smeared, tree-level improved clover fermions combined with improved simulation algorithms. We have seen in a detailed scaling study that this action possesses excellent scaling properties and, furthermore, that with this combination of action and algorithms small pion masses can be reached – free of any metastabilities or other algorithmic problems.

The setup was then applied to a calculation of the light hadron spectrum of QCD. In this simulation all sources of systematic errors could be controlled. To make this possible, a large set of ensembles was generated covering different up/down and strange quark masses with pion masses down to 190 MeV, three different lattice spacings, lattice volumes that satisfy the $M_\pi L \gtrsim 4$ criterion and additional small and large volume points. By including different interpolation and extrapolation methods and by correctly treating the remaining (small) finite-size effects, the magnitude of all systematic errors could be estimated. The final result is the spectrum of fig. 3.17 and tab. 3.4. All calculated hadron masses are found to be in perfect agreement with their experimental values within $O(1)$ per-cent errors or better. This is the main result of the chapter.

Beyond providing a calculation of the light hadron spectrum from first principles, this result also shows that with this simulation setup reliable and precise estimates of other quantities of interest will be possible in the future.

Chapter 4

Conclusion and Outlook

As mentioned in the introduction, only a few years ago it was unclear which algorithms and actions would be suitable for high precision LQCD simulations. Wilson type fermions suffer from *critical slowing down* and staggered fermions, as discussed at great lengths in the literature, potentially have unresolved problems due to unquantifiable systematic errors. Different approaches were taken to address these issues, two of which I have described in this thesis.

In chapter 2, I presented a variant of the HMC algorithm for simulating dynamical overlap fermions. The classical HMC fails due to the discontinuity in the overlap operator at the boundaries between sectors with different topological index. The new method treats this problem by altering the integrator of the MD integration whenever a discontinuity is detected. This method was tested and found to behave as expected. However, the transmission rate, *i.e.* the rate of changes between the different topological sectors, was found to decrease exponentially with the quark mass. The reason for this problem was located and and a solution was proposed. This new method was tested and found to work as expected. It allows simulations with frequent topological charge changes even at small quark masses and on lattices with volumes of up to $16^3 \times 48$. Thus, with this new algorithm, simulations on medium to large lattice are in the reach of future supercomputers of the $O(100)$ TFlop/s to 1 PFlop/s class.

The focus of chapter 3 was on simulations with improved Wilson fermions. Here, by improving both the simulation algorithm and the lattice action, pion masses as small as 190 MeV could be reached. The algorithmic setup was tested thoroughly and no signs of metastabilities or exceptional configurations were seen. In a detailed scaling study the excellent scaling properties of the improved lattice action could be demonstrated. This

combination of algorithm and action was then used to calculate the masses of the low-lying mesons and baryons with high precision and fully controlled systematic errors. With the calculated masses being in perfect agreement with the experiment, this provides both further strong evidence for the correctness of QCD in the non-perturbative regime, as well as a proof of concept, showing that with this simulation setup, high precision predictions of QCD observables will be possible in the future. This result is considered to be a *milestone* [21] "in a 30-year effort of theoretical and computational physics" [122] and was selected as one of the top-10 scientific developments of 2008 [123].

Acknowledgments

First of all I would like to thank my advisor Thomas Lippert for his support. His help and encouragement was key to accomplishing this thesis. I am also especially grateful to Zoltán Fodor for his part in this work.

I would like to thank Nigel Cundy for his on-going collaboration and enlightening and enjoyable discussions, not only about physics. He has great part in the results of chapter 2.

It was a great pleasure to work together with Kálmán Szabó during the various stages of the dynamical clover projects. I am also very grateful for the collaboration and discussions with him, Christian Hoelbling, Laurent Lellouch, Stephan Dürr, Sandor Katz, Thorsten Kurth and the other members of the Budapest-Marseille-Wuppertal collaboration. To be honest and also fair to everybody, I should say that the results of chapter 3 do not belong the me alone. More precisely, my contributions include:

- Implementing and optimizing simulation algorithms and software,
- running large scale simulations ([4]),
- and analyzing data ([4]).

I would also like to thank Pavlos Vranas for his kind support and collaboration and the Blue Gene group for their hospitality during my different visits to the IBM Thomas J. Watson Research Center in Yorktown Heights, New York. I am also very grateful to Laurent Lellouch for doing the same during my stay at the Centre de Physique Théorique (CNRS) at Marseille.

Furthermore I would like to thank Ivo ("Dipl.-Ingsane") Kabadshow, my office mate, Matthias Bolten (alias "The maths geek next door"), Binh Trieu, Tom ("Der Holländer")

Schröder and my other fellow PhD-students of the “Doktorandenflur” at the Jülich Research Centre for their on-going distractions from the things that are supposedly so very important.

While the air we breathe is usually free of charge, lunch generally is not. I am very greatful for the financial support provided by the Forschungszentrum Jülich through the Doktorandenausschuss and by the Deutsche Forschungsgemeinschaft through grant Li 701/5-2.

The computations were performed on clusters at the Bergische Universität Wuppertal, at the Centre de Physique Théorique (CNRS) at Marseille, on the Blue Gene/P at IDRIS (CNRS) Orsay, and on clusters, the Blue Gene/L, and the Blue Gene/P at Forschungszentrum Jülich. I am very grateful for the generous allocation of computer time by the John von Neumann Institute for Computing and the “Kommission zur Vergabe von Supercomputer-Ressourcen” of the Forschungszentrum Jülich, which made this work possible.

Last but not least I would like to thank the staff of the Juelich Supercomputing Centre, especially Rüdiger Esser, Gaby Porschen, Bettina Scheid, Marc-André Hermanns, Wolfgang Frings for their time and assistance, Jutta Docter and Michael Stephan for their patience and their help with the Blue Gene machines and many more who I did not forget but are just too numerous to be mentioned here.

Figures

Tables

Bibliography

[1] Michael Edward Peskin and Daniel V. Schroeder, *An Introduction to quantum field theory*, Reading, USA: Addison-Wesley (1995) 842 p.

[2] Kenneth G. Wilson, *Confinement of quarks*, Phys. Rev., **D10**, 2445–2459, 1974.

[3] Kenneth G. Wilson, *Quarks and Strings on a Lattice*, New Phenomena In Subnuclear Physics. Part A. Proceedings of the First Half of the 1975 International School of Subnuclear Physics, Erice, Sicily, July 11 - August 1, 1975, ed. A. Zichichi, Plenum Press, New York, 1977, p. 69, CLNS-321.

[4] S. Durr et al., *Ab Initio Determination of Light Hadron Masses*, Science, **322**, 1224–1227, 2008.

[5] R. Narayanan and H. Neuberger, *Chiral fermions on the lattice*, Phys. Rev. Lett., **71**, 3251–3254, 1993.

[6] H. Neuberger, *Exactly massless quarks on the lattice*, Phys. Lett., **B417**, 141–144, 1998.

[7] M. Lüscher, *Abelian chiral gauge theories on the lattice with exact gauge invariance*, Nucl. Phys., **B549**, 295–334, 1999.

[8] P. H. Ginsparg and K. G. Wilson, *A remnant of chiral symetry on the lattice*, Phys. Rev., **D25**, 2649, 1982.

[9] J. van den Eshof, A. Frommer, T. Lippert, K. Schilling, and H. A. van der Vorst, *Numerical methods for the QCD overlap operator. I: Sign- function and error bounds*, Comput. Phys. Commun., **146**, 203–224, 2002.

[10] S. Duane, A. D. Kennedy, B. J. Pendleton, and D. Roweth, *Hybrid Monte Carlo*, Phys. Lett., **B195**, 216–222, 1987.

[11] M. Creutz, *Quarks, gluons and lattices*, Cambridge monographs on mathematical physics. Cambridge University Press, 1983.

[12] I. Montvay and G. Munster, *Quantum fields on a lattice*, Cambridge monographs on mathematical physics. Cambridge University Press, 1994.

[13] J. Smit, *Introduction to quantum fields on a lattice: A robust mate*, vol. 15 of *Cambridge Lecture Notes in Physics*, Cambridge University Press, 2002.

[14] H. J. Rothe, *Lattice gauge theories: An Introduction*, vol. 74 of *World Scientific Lecture Notes in Physics*, World Scientific, 2005.

[15] Thomas DeGrand and Carleton E. DeTar, *Lattice methods for quantum chromodynamics*, World Scientific, 2006.

[16] Michael E. Fisher, *The theory of equilibrium critical phenomena*, Rep. Prog. Phys., **30**, 615–730, 1967.

[17] Michael E. Fisher, *Corrigendum: The theory of equilibrium critical phenomena*, Rep. Prog. Phys., **31**, 431, 1968.

[18] H. Eugene Stanley, *Introduction to Phase Transitions and Critical Phenomena*, International Series of Monographs on Physics. Oxford University Press, Oxford, 1987.

[19] N. Cundy et al., *Numerical methods for the QCD overlap operator. IV: Hybrid Monte Carlo*, Comput. Phys. Commun., **180**, 26–54, 2009.

[20] Nigel Cundy, Stefan Krieg, Thomas Lippert, and Andreas Schäfer, *Topological tunneling with Dynamical overlap fermions*, Comp. Phys. Commun., **180**, 201–208, 2009.

[21] Frank Wilczek, *Particle physics: Mass by numbers*, Nature, **456**, 449–450, 2008.

[22] S. Durr et al., *Scaling study of dynamical smeared-link clover fermions*, Phys. Rev., **D79**, 014501, 2009.

[23] Ferenc Niedermayer, *Exact chiral symmetry, topological charge and related topics*, Nucl. Phys. Proc. Suppl., **73**, 105–119, 1999.

[24] K. F. Liu, A. Alexandru, and I. Horvath, *Gauge Field Strength Tensor from the Overlap Dirac Operator*, Phys. Lett., **B659**, 773–782, 2008.

[25] Ivan Horvath, *Ginsparg-Wilson relation and ultralocality*, Phys. Rev. Lett., **81**, 4063–4066, 1998.

[26] Ivan Horvath, *Ginsparg-Wilson-Luescher symmetry and ultralocality*, Phys. Rev., **D60**, 034510, 1999.

[27] Ivan Horvath, Chetan T. Balwe, and Robert Mendris, *Strong non-ultralocality of Ginsparg-Wilson fermionic actions*, Nucl. Phys., **B599**, 283–304, 2001.

[28] Ivan Horvath, *A framework for systematic study of QCD vacuum structure. II: Coherent lattice QCD*, 2006.

[29] P. Hasenfratz, *Prospects for perfect actions*, Nucl. Phys. Proc. Suppl., **63**, 53–58, 1998.

[30] D. B. Kaplan, *A Method for simulating chiral fermions on the lattice*, Phys. Lett., **B288**, 342–347, 1992.

[31] I. P. Omelyan, I. M. Mrygloda, and R. Folk, *Symplectic analytically integrable decomposition algorithms: classification, derivation, and application to molecular dynamics, quantum and celestial mechanics simulations*, Computer Physics Communications, **151**, 272, 2003.

[32] Tetsuya Takaishi and Philippe de Forcrand, *Testing and tuning new symplectic integrators for hybrid Monte Carlo algorithm in lattice QCD*, Phys. Rev., **E73**, 036706, 2006.

[33] J. C. Sexton and D. H. Weingarten, *Hamiltonian evolution for the hybrid Monte Carlo algorithm*, Nucl. Phys., **B 380**, 665, 1992.

[34] A. D. Kennedy and M. A. Clark, *Speeding up HMC with better integrators*, PoS, **LAT2007**, 038, 2007.

[35] I. P. Omelyan, I. M. Mryglod, and R. Folk, *Optimized Verlet-like algorithms for molecular dynamics simulations*, Phys. Rev. E, **65**, no. 5, 056706, May 2002.

[36] Michael Creutz and Andreas Gocksch, *Higher oder Hybrid Monte Carlo algorithms*, Phys. Rev. Lett., **63**, 9, 1989.

[37] Massimo Campostrini and Paolo Rossi, *A comparison of numerical algorithms for dynamical fermions*, Nucl. Phys., **B329**, 753, 1990.

[38] Siu A. Chin and Donald W. Kidwell, *Higher-order force gradient symplectic algorithms*, Phys. Rev. E, **62**, no. 6, 8746–8752, Dec 2000.

[39] G. Arnold, K. Schilling, and T. Lippert, *Multicanonical hybrid Monte Carlo: Boosting simulations of compact QED*, Phys. Rev., **D59**, 054509, 1999.

[40] Rajan Gupta, *Simulating QCD with dynamical Wilson and staggered fermions*, Nucl. Phys. Proc. Suppl., **9**, 473–483, 1989.

[41] Sourendu Gupta, A. Irback, F. Karsch, and B. Petersson, *The acceptance probability in the Hybrid Monte Carlo method*, Phys. Lett., **B242**, 437–443, 1990.

[42] H. Gausterer and M. Salmhofer, *Remarks on global Monte Carlo algorithms*, Phys. Rev., **D40**, 2723–2726, 1989.

[43] M. Creutz, *Global Monte Carlo algorithms for may fermion systems*, Phys. Rev., **D38**, 1228–1238, 1988.

[44] H. Neuberger, *A practical implementation of the overlap-Dirac operator*, Phys. Rev. Lett., **81**, 4060–4062, 1998.

[45] Andreas Frommer, Bertold Nockel, Stephan Gusken, Thomas Lippert, and Klaus Schilling, *Many masses on one stroke: Economic computation of quark propagators*, Int. J. Mod. Phys., **C6**, 627–638, 1995.

[46] B. Jegerlehner, *Multiple mass solvers*, Nucl. Phys. Proc. Suppl., **63**, 958–960, 1998.

[47] D. Ingerman, V. Druskin, and L. Knizerhman, Comm. Pure Appl. Math., **53**, 1039, 2000.

[48] P. P. Petrushev and V. A. Popov, *Rational approximation of real functions*, Cambridge University Press, 1987.

[49] Nigel Cundy, *Small Wilson Dirac operator eigenvector mixing in dynamical overlap hybrid Monte-Carlo*, Comp. Phys. Commun., **180**, 180–191, 2009.

[50] Nigel Cundy, Stefan Krieg, Thomas Lippert, and Andreas Schafer, *Dynamical overlap fermions with increased topological tunnelling*, PoS, **LAT2007**, 030, 2007.

[51] G. I. Egri, Z. Fodor, S. D. Katz, and K. K. Szabo, *Topology with dynamical overlap fermions*, JHEP, 01, 049, 2006.

[52] Hidenori Fukaya, Shoji Hashimoto, Takuya Hirohashi, Kenji Ogawa, and Tetsuya Onogi, *Topology conserving gauge action and the overlap-Dirac operator*, Phys. Rev., **D73**, 014503, 2006.

[53] Z. Fodor, S. D. Katz, and K. K. Szabo, *Dynamical overlap fermions, results with hybrid Monte-Carlo algorithm*, JHEP, **08**, 003, 2004.

[54] Z. Fodor, S. D. Katz, and K. K. Szabo, *Dynamical overlap fermions, results with HMC algorithm*, Nucl. Phys. Proc. Supp., **140C**, 2004.

[55] Nigel Cundy, *Current status of dynamical overlap project*, Nucl. Phys. Proc. Suppl., **153**, 54–61, 2006.

[56] R. P. Brent, *Algorithms for minimization without Derivitives*, Englewood Cliffs, NJ, 1973.

[57] W. Press, S. Teukolsky, W. Vetterling, and B. Flannery, *Numerical Recipies in Fortran, 2nd Ed.*, Cambridge University Press, 1992.

[58] G. Arnold et al., *Numerical methods for the QCD overlap operator. II: Optimal Krylov subspace methods*, 2003, Published in "Edinburgh 2003, QCD and numerical analysis" 153-167.

[59] Nigel Cundy et al., *Numerical methods for the QCD overlap operator. III: Nested iterations*, Comput. Phys. Commun., **165**, 221–242, 2005.

[60] Nigel Cundy, Stefan Krieg, and Thomas Lippert, *Improving the dynamical overlap algorithm*, PoS, **LAT2005**, 107, 2006.

[61] S. Krieg et al., *Improving inversions of the overlap operator*, Nucl. Phys. Proc. Supp., **140C**, 2005.

[62] Stefan Krieg, "Simulation der Quantenchromodynamik mit dynamischen Overlap-Fermionen", Master's thesis, Bergische Universität Wuppertal, Wuppertal, Germany, 2004, WU D 04-11.

[63] R. J. Crewther, *Chirality Selection Rules and the U(1) Problem*, Phys. Lett., **B70**, 349, 1977.

[64] P. Di Vecchia and G. Veneziano, *Chiral Dynamics in the Large n Limit*, Nucl. Phys., **B171**, 253, 1980.

[65] H. Leutwyler and Andrei V. Smilga, *Spectrum of Dirac operator and role of winding number in QCD*, Phys. Rev., **D46**, 5607–5632, 1992.

[66] S. Dürr, *Topological susceptibility in full QCD: Lattice results versus the prediction from the QCD partition function with granularity*, Nucl. Phys., **B611**, 281–310, 2001.

[67] Thomas A. DeGrand and Stefan Schaefer, *Physics issues in simulations with dynamical overlap fermions*, Phys. Rev., **D71**, 034507, 2005.

[68] Martin Hasenbusch, *Speeding up the Hybrid-Monte-Carlo algorithm for dynamical fermions*, Phys. Lett., **B519**, 177–182, 2001.

[69] Stefan Schaefer, *Algorithms for dynamical overlap fermions*, PoS, **LAT2006**, 020, 2006.

[70] R. Sommer, *A New way to set the energy scale in lattice gauge theories and its applications to the static force and alpha-s in SU(2) Yang-Mills theory*, Nucl. Phys., **B411**, 839–854, 1994.

[71] M. Luscher and P. Weisz, *On-Shell Improved Lattice Gauge Theories*, Commun. Math. Phys., **97**, 59, 1985.

[72] Mark G. Alford, W. Dimm, G. P. Lepage, G. Hockney, and P. B. Mackenzie, *Lattice QCD on small computers*, Phys. Lett., **B361**, 87–94, 1995.

[73] S. Krieg, N. Attig, N. Cundy, T. Lippert, *A comparison of methods to calculate the chiral condensate with overlap fermions*, Comput. Phys. Commun., **179**, 181–183, 2008.

[74] T. Lippert and K. Schilling, *Computational costs of future QCD simulations in the deep chiral regime*, Prepared for NATO Advanced Research Workshop on Lattice Fermions and Structure of the Vacuum, Dubna, Russia, 5-9 Oct 1999.

[75] C. Bernard et al., *Panel discussion on the cost of dynamical quark simulations*, Nucl. Phys. Proc. Suppl., **106**, 199–205, 2002.

[76] Karl Jansen, *Actions for dynamical fermion simulations: Are we ready to go?*, Nucl. Phys. Proc. Suppl., **129**, 3–16, 2004.

[77] A. Ukawa, *Computational cost of full QCD simulations experienced by CP-PACS and JLQCD Collaborations*, Nucl. Phys. Proc. Suppl., **106**, 195–196, 2002.

[78] Ken-Ichi Ishikawa, *Recent algorithm and machine developments for lattice QCD*, 2008.

[79] Martin Luscher, *Deflation acceleration of lattice QCD simulations*, JHEP, **12**, 011, 2007.

[80] M. A. Clark, B. Joo, and A. D. Kennedy, *Comparing the R algorithm and RHMC for staggered fermions*, Nucl. Phys. Proc. Suppl., **119**, 1015–1017, 2003.

[81] M. A. Clark and A. D. Kennedy, *Accelerating Dynamical Fermion Computations using the Rational Hybrid Monte Carlo (RHMC) Algorithm with Multiple Pseudofermion Fields*, Phys. Rev. Lett., **98**, 051601, 2007.

[82] A. Ali Khan et al., *Accelerating the hybrid Monte Carlo algorithm*, Phys. Lett., **B564**, 235–240, 2003.

[83] C. Urbach, K. Jansen, A. Shindler, and U. Wenger, *HMC algorithm with multiple time scale integration and mass preconditioning*, Comput. Phys. Commun., **174**, 87–98, 2006.

[84] Stefan Krieg, ", talk at Lattice 2006.

[85] B. Sheikholeslami and R. Wohlert, *Improved Continuum Limit Lattice Action for QCD with Wilson Fermions*, Nucl. Phys., **B259**, 572, 1985.

[86] Claude W. Bernard and Thomas A. DeGrand, *Perturbation theory for fat-link fermion actions*, Nucl. Phys. Proc. Suppl., **83**, 845–847, 2000.

[87] Claude W. Bernard et al., *f(B) for various actions: Approaching the continuum limit with dynamical fermions*, Nucl. Phys. Proc. Suppl., **94**, 346–349, 2001.

[88] Stefano Capitani, Stephan Durr, and Christian Hoelbling, *Rationale for UV-filtered clover fermions*, JHEP, **11**, 028, 2006.

[89] Thomas A. DeGrand, Anna Hasenfratz, and Tamas G. Kovacs, *Optimizing the chiral properties of lattice fermion actions*, 1998.

[90] Mark Stephenson, Carleton E. DeTar, Thomas A. DeGrand, and Anna Hasenfratz, *Scaling and eigenmode tests of the improved fat clover action*, Phys. Rev., **D63**, 034501, 2001.

[91] James M. Zanotti et al., *Hadron Masses From Novel Fat-Link Fermion Actions*, Phys. Rev., **D65**, 074507, 2002.

[92] M. Luscher and P. Weisz, *Computation of the Action for On-Shell Improved Lattice Gauge Theories at Weak Coupling*, Phys. Lett., **B158**, 250, 1985.

[93] Colin Morningstar and Mike J. Peardon, *Analytic smearing of SU(3) link variables in lattice QCD*, Phys. Rev., **D69**, 054501, 2004.

[94] Anna Hasenfratz, Roland Hoffmann, and Stefan Schaefer, *Hypercubic Smeared Links for Dynamical Fermions*, JHEP, **05**, 029, 2007.

[95] Stephan Durr, *Theoretical issues with staggered fermion simulations*, PoS, **LAT2005**, 021, 2006.

[96] P. Hernandez, K. Jansen, and M. Lüscher, *Locality properties of Neuberger's lattice Dirac operator*, Nucl. Phys., **B552**, 363–378, 1999.

[97] Tamas G. Kovacs, *Locality and topology with fat link overlap actions*, Phys. Rev., **D67**, 094501, 2003.

[98] M. A. Clark, A. D. Kennedy, and Z. Sroczynski, *Exact 2+1 flavour RHMC simulations*, Nucl. Phys. Proc. Suppl., **140**, 835–837, 2005.

[99] M. A. Clark, Ph. de Forcrand, and A. D. Kennedy, *Algorithm shootout: R versus RHMC*, PoS, **LAT2005**, 115, 2006.

[100] M. A. Clark, *The rational hybrid Monte Carlo algorithm*, PoS, **LAT2006**, 004, 2006.

[101] Thomas A. DeGrand and Pietro Rossi, *Conditioning techniques for dynamical fermions*, Comput. Phys. Commun., **60**, 211–214, 1990.

[102] M. Hasenbusch and K. Jansen, *Speeding up lattice QCD simulations with clover-improved Wilson fermions*, Nucl. Phys., **B659**, 299–320, 2003.

[103] Martin Hasenbusch, *Full QCD algorithms towards the chiral limit*, Nucl. Phys. Proc. Suppl., **129**, 27–33, 2004.

[104] Stefan Krieg, "Optimizing Lattice QCD Simulations on Blue Gene/L", in: Parallel Computing: Architectures, Algorithms and Applications, C. Bischof, M. Bücker, P. Gibbon, G. Joubert, T. Lippert, B. Mohr, F. Peters, (Ed.), pp. 543 – 550. Amsterdam, IOS Press, 2008.

[105] L. Del Debbio, L. Giusti, M. Luscher, R. Petronzio, and N. Tantalo, *Stability of lattice QCD simulations and the thermodynamic limit*, JHEP, **02**, 011, 2006.

[106] S. Aoki et al., *Bulk first-order phase transition in three-flavor lattice QCD with O(a)-improved Wilson fermion action at zero temperature*, Phys. Rev., **D72**, 054510, 2005.

[107] F. Farchioni et al., *Twisted mass quarks and the phase structure of lattice QCD*, Eur. Phys. J., **C39**, 421–433, 2005.

[108] F. Farchioni et al., *The phase structure of lattice QCD with Wilson quarks and renormalization group improved gluons*, Eur. Phys. J., **C42**, 73–87, 2005.

[109] Karl Jansen et al., *Stout Smearing for Twisted Mass Fermions*, PoS, **LAT2007**, 036, 2007.

[110] Steven Weinberg, *The quantum theory of fields. Vol. 2: Modern applications*, Cambridge, UK: Univ. Pr. (1996) 489 p.

[111] S Mignani and R Rosa, *The moving block bootstrap to assess the accuracy of statistical estimates in Ising model simulations*, Comput. Phys. Commun., **92**, 203–213, 1995.

[112] M. Luscher, *Volume Dependence of the Energy Spectrum in Massive Quantum Field Theories. 1. Stable Particle States*, Commun. Math. Phys., **104**, 177, 1986.

[113] M. Luscher, *Volume Dependence of the Energy Spectrum in Massive Quantum Field Theories. 2. Scattering States*, Commun. Math. Phys., **105**, 153–188, 1986.

[114] M. Luscher, *Two particle states on a torus and their relation to the scattering matrix*, Nucl. Phys., **B354**, 531–578, 1991.

[115] M. Luscher, *Signatures of unstable particles in finite volume*, Nucl. Phys., **B364**, 237–254, 1991.

[116] Gilberto Colangelo, Stephan Durr, and Christoph Haefeli, *Finite volume effects for meson masses and decay constants*, Nucl. Phys., **B721**, 136–174, 2005.

[117] Gilberto Colangelo, Andreas Fuhrer, and Christoph Haefeli, *The pion and proton mass in finite volume*, Nucl. Phys. Proc. Suppl., **153**, 41–48, 2006.

[118] Paul Langacker and Heinz Pagels, *Applications of Chiral Perturbation Theory: Mass Formulas and the Decay eta → 3 pi*, Phys. Rev., **D10**, 2904, 1974.

[119] W. M. Yao et al., *Review of particle physics*, J. Phys., **G33**, 1–1232, 2006.

[120] Roger F. Dashen, *Chiral SU(3) x SU(3) as a symmetry of the strong interactions*, Phys. Rev., **183**, 1245–1260, 1969.

[121] C. Aubin et al., *Light pseudoscalar decay constants, quark masses, and low energy constants from three-flavor lattice QCD*, Phys. Rev., **D70**, 114501, 2004.

[122] Andreas S. Kronfeld, *The Weight of the World Is Quantum Chromodynamics*, Science, **322**, 1198, 2008.

[123] *Proton's Mass 'Predicted'*, Science, **322**, 1772, 2008.

Already published:

Modern Methods and Algorithms of Quantum Chemistry - Proceedings
Johannes Grotendorst (Editor)
Winter School, 21 - 25 February 2000, Forschungszentrum Jülich
NIC Series Volume 1
ISBN 3-00-005618-1, February 2000, 562 pages
out of print

Modern Methods and Algorithms of Quantum Chemistry - Poster Presentations
Johannes Grotendorst (Editor)
Winter School, 21 - 25 February 2000, Forschungszentrum Jülich
NIC Series Volume 2
ISBN 3-00-005746-3, February 2000, 77 pages
out of print

Modern Methods and Algorithms of Quantum Chemistry - Proceedings, Second Edition
Johannes Grotendorst (Editor)
Winter School, 21 - 25 February 2000, Forschungszentrum Jülich
NIC Series Volume 3
ISBN 3-00-005834-6, December 2000, 638 pages
out of print

Nichtlineare Analyse raum-zeitlicher Aspekte der hirnelektrischen Aktivität von Epilepsiepatienten
Jochen Arnold
NIC Series Volume 4
ISBN 3-00-006221-1, September 2000, 120 pages

Elektron-Elektron-Wechselwirkung in Halbleitern: Von hochkorrelierten kohärenten Anfangszuständen zu inkohärentem Transport
Reinhold Lövenich
NIC Series Volume 5
ISBN 3-00-006329-3, August 2000, 146 pages

Erkennung von Nichtlinearitäten und wechselseitigen Abhängigkeiten in Zeitreihen
Andreas Schmitz
NIC Series Volume 6
ISBN 3-00-007871-1, May 2001, 142 pages

Multiparadigm Programming with Object-Oriented Languages - Proceedings
Kei Davis, Yannis Smaragdakis, Jörg Striegnitz (Editors)
Workshop MPOOL, 18 May 2001, Budapest
NIC Series Volume 7
ISBN 3-00-007968-8, June 2001, 160 pages

Europhysics Conference on Computational Physics - Book of Abstracts
Friedel Hossfeld, Kurt Binder (Editors)
Conference, 5 - 8 September 2001, Aachen
NIC Series Volume 8
ISBN 3-00-008236-0, September 2001, 500 pages

NIC Symposium 2001 - Proceedings
Horst Rollnik, Dietrich Wolf (Editors)
Symposium, 5 - 6 December 2001, Forschungszentrum Jülich
NIC Series Volume 9
ISBN 3-00-009055-X, May 2002, 514 pages

Quantum Simulations of Complex Many-Body Systems: From Theory to Algorithms - Lecture Notes
Johannes Grotendorst, Dominik Marx, Alejandro Muramatsu (Editors)
Winter School, 25 February - 1 March 2002, Rolduc Conference Centre, Kerkrade, The Netherlands
NIC Series Volume 10
ISBN 3-00-009057-6, February 2002, 548 pages

Quantum Simulations of Complex Many-Body Systems: From Theory to Algorithms- Poster Presentations
Johannes Grotendorst, Dominik Marx, Alejandro Muramatsu (Editors)
Winter School, 25 February - 1 March 2002, Rolduc Conference Centre, Kerkrade, The Netherlands
NIC Series Volume 11
ISBN 3-00-009058-4, February 2002, 194 pages

Strongly Disordered Quantum Spin Systems in Low Dimensions: Numerical Study of Spin Chains, Spin Ladders and Two-Dimensional Systems
Yu-cheng Lin
NIC Series Volume 12
ISBN 3-00-009056-8, May 2002, 146 pages

Multiparadigm Programming with Object-Oriented Languages - Proceedings
Jörg Striegnitz, Kei Davis, Yannis Smaragdakis (Editors)
Workshop MPOOL 2002, 11 June 2002, Malaga
NIC Series Volume 13
ISBN 3-00-009099-1, June 2002, 132 pages

Quantum Simulations of Complex Many-Body Systems: From Theory to Algorithms - Audio-Visual Lecture Notes
Johannes Grotendorst, Dominik Marx, Alejandro Muramatsu (Editors)
Winter School, 25 February - 1 March 2002, Rolduc Conference Centre, Kerkrade, The Netherlands
NIC Series Volume 14
ISBN 3-00-010000-8, November 2002, DVD

Numerical Methods for Limit and Shakedown Analysis
Manfred Staat, Michael Heitzer (Eds.)
NIC Series Volume 15
ISBN 3-00-010001-6, February 2003, 306 pages

Design and Evaluation of a Bandwidth Broker that Provides Network Quality of Service for Grid Applications
Volker Sander
NIC Series Volume 16
ISBN 3-00-010002-4, February 2003, 208 pages

Automatic Performance Analysis on Parallel Computers with SMP Nodes
Felix Wolf
NIC Series Volume 17
ISBN 3-00-010003-2, February 2003, 168 pages

Haptisches Rendern zum Einpassen von hochaufgelösten Molekülstrukturdaten in niedrigaufgelöste Elektronenmikroskopie-Dichteverteilungen
Stefan Birmanns
NIC Series Volume 18
ISBN 3-00-010004-0, September 2003, 178 pages

Auswirkungen der Virtualisierung auf den IT-Betrieb
Wolfgang Gürich (Editor)
GI Conference, 4 - 5 November 2003, Forschungszentrum Jülich
NIC Series Volume 19
ISBN 3-00-009100-9, October 2003, 126 pages

NIC Symposium 2004
Dietrich Wolf, Gernot Münster, Manfred Kremer (Editors)
Symposium, 17 - 18 February 2004, Forschungszentrum Jülich
NIC Series Volume 20
ISBN 3-00-012372-5, February 2004, 482 pages

Measuring Synchronization in Model Systems and Electroencephalographic Time Series from Epilepsy Patients
Thomas Kreutz
NIC Series Volume 21
ISBN 3-00-012373-3, February 2004, 138 pages

Computational Soft Matter: From Synthetic Polymers to Proteins - Poster Abstracts
Norbert Attig, Kurt Binder, Helmut Grubmüller, Kurt Kremer (Editors)
Winter School, 29 February - 6 March 2004, Gustav-Stresemann-Institut Bonn
NIC Series Volume 22
ISBN 3-00-012374-1, February 2004, 120 pages

Computational Soft Matter: From Synthetic Polymers to Proteins - Lecture Notes
Norbert Attig, Kurt Binder, Helmut Grubmüller, Kurt Kremer (Editors)
Winter School, 29 February - 6 March 2004, Gustav-Stresemann-Institut Bonn
NIC Series Volume 23
ISBN 3-00-012641-4, February 2004, 440 pages

Synchronization and Interdependence Measures and their Applications to the Electroencephalogram of Epilepsy Patients and Clustering of Data
Alexander Kraskov
NIC Series Volume 24
ISBN 3-00-013619-3, May 2004, 106 pages

High Performance Computing in Chemistry
Johannes Grotendorst (Editor)
Report of the Joint Research Project:
High Performance Computing in Chemistry - HPC-Chem
NIC Series Volume 25
ISBN 3-00-013618-5, December 2004, 160 pages

Zerlegung von Signalen in unabhängige Komponenten: Ein informationstheoretischer Zugang
Harald Stögbauer
NIC Series Volume 26
ISBN 3-00-013620-7, April 2005, 110 pages

Multiparadigm Programming 2003
Joint Proceedings of the
3rd International Workshop on Multiparadigm Programming with Object-Oriented Languages (MPOOL'03)
and the
1st International Workshop on Declarative Programming in the Context of Object-Oriented Languages (PD-COOL'03)
Jörg Striegnitz, Kei Davis (Editors)
NIC Series Volume 27
ISBN 3-00-016005-1, July 2005, 300 pages

Integration von Programmiersprachen durch strukturelle Typanalyse und partielle Auswertung
Jörg Striegnitz
NIC Series Volume 28
ISBN 3-00-016006-X, May 2005, 306 pages

OpenMolGRID - Open Computing Grid for Molecular Science and Engineering
Final Report
Mathilde Romberg (Editor)
NIC Series Volume 29
ISBN 3-00-016007-8, July 2005, 86 pages

GALA Grünenthal Applied Life Science Analysis
Achim Kless and Johannes Grotendorst (Editors)
NIC Series Volume 30
ISBN 3-00-017349-8, November 2006, 204 pages

Computational Nanoscience: Do It Yourself!
Lecture Notes
Johannes Grotendorst, Stefan Blügel, Dominik Marx (Editors)
Winter School, 14. - 22 February 2006, Forschungszentrum Jülich
NIC Series Volume 31
ISBN 3-00-017350-1, February 2006, 528 pages

NIC Symposium 2006 - Proceedings
G. Münster, D. Wolf, M. Kremer (Editors)
Symposium, 1 - 2 March 2006, Forschungszentrum Jülich
NIC Series Volume 32
ISBN 3-00-017351-X, February 2006, 384 pages

Parallel Computing: Current & Future Issues of High-End Computing
Proceedings of the International Conference ParCo 2005
G.R. Joubert, W.E. Nagel, F.J. Peters,
O. Plata, P. Tirado, E. Zapata (Editors)
NIC Series Volume 33
ISBN 3-00-017352-8, October 2006, 930 pages

From Computational Biophysics to Systems Biology 2006 Proceedings
U.H.E. Hansmann, J. Meinke, S. Mohanty, O. Zimmermann (Editors)
NIC Series Volume 34
ISBN-10 3-9810843-0-6, ISBN-13 978-3-9810843-0-6,
September 2006, 224 pages

Dreistufig parallele Software zur Parameteroptimierung von Support-Vektor-Maschinen mit kostensensitiven Gütemaßen
Tatjana Eitrich
NIC Series Volume 35
ISBN 978-3-9810843-1-3, March 2007, 262 pages

From Computational Biophysics to Systems Biology (CBSB07)
Proceedings
U.H.E. Hansmann, J. Meinke, S. Mohanty, O. Zimmermann (Editors)
NIC Series Volume 36
ISBN 978-3-9810843-2-0, August 2007, 330 pages

Parallel Computing: Architectures, Algorithms and Applications -
Book of Abstracts
Book of Abstracts, ParCo 2007 Conference, 4. - 7. September 2007
G.R. Joubert, C. Bischof, F. Peters, T. Lippert, M. Bücker, P. Gibbon, B. Mohr (Eds.)
NIC Series Volume 37
ISBN 978-3-9810843-3-7, August 2007, 216 pages

Parallel Computing: Architectures, Algorithms and Applications -
Proceedings
Proceedings, ParCo 2007 Conference, 4. - 7. September 2007
C. Bischof, M. Bücker, P. Gibbon, G.R. Joubert, T. Lippert, B. Mohr, F. Peters (Eds.)
NIC Series Volume 38
ISBN 978-3-9810843-4-4, December 2007, 830 pages

NIC Symposium 2008 - Proceedings
G. Münster, D. Wolf, M. Kremer (Editors)
Symposium, 20 - 21 February 2008, Forschungszentrum Jülich
NIC Series Volume 39
ISBN 978-3-9810843-5-1, February 2008, 380 pages

From Computational Biophysics to Systems Biology (CBSB08)
Proceedings
Ulrich H.E. Hansmann, Jan H. Meinke, Sandipan Mohanty, Walter Nadler,
Olav Zimmermann (Eds.) (Editors)
NIC Series Volume 40
ISBN 978-3-9810843-6-8, July 2008, 452 pages

Multigrid methods for structured grids and their application
in particle simulation
Matthias Bolten
NIC Series Volume 41
ISBN 978-3-9810843-7-5, December 2008, 153 pages

Multiscale Simulation Methods in Molecular Sciences
Lecture Notes
Johannes Grotendorst, Norbert Attig, Stefan Blügel, Dominik Marx (Eds.)
Winter School, 2. - 6. March 2009, Forschungszentrum Jülich
NIC Series Volume 42
ISBN 978-3-9810843-8-2, March 2009, 576 pages

All volumes are available online at

http:// www.fz-juelich.de/nic-series/.